THE KINETICS OF SURFACE-MEDIATED PHASE SEPARATION
IN THE QUASI-BINARY MIXTURE OF GUAIACOL-GLYCEROL-WATER

By

QINGBIAO SHI

A DISSERTATION PRESENTED TO THE GRADUATE SCHOOL
OF THE UNIVERSITY OF FLORIDA IN PARTIAL FULFILLMENT
OF THE REQUIREMENTS FOR THE DEGREE OF
DOCTOR OF PHILOSOPHY

UNIVERSITY OF FLORIDA

1994

Dedicated to my grandmother

FENG-HWA FU

ACKNOWLEDGMENTS

patience and warmheartedness were indispensable for me to get over the initial "culture shock" and the language barrier.

Heartfelt thanks go to Rob and Cynthia, for their friendship over the years, even after they had moved away. Their enthusiasm and encouragement are deeply appreciated, especially when I felt down and out.

Finally, to a special friend, C. J., I want to say thanks.

TABLE OF CONTENTS

Abstract of Dissertation Presented to the Graduate School
of the University of Florida in Partial Fulfillment of the
Requirements for the Degree of Doctor of Philosophy

THE KINETICS OF SURFACE-MEDIATED PHASE SEPARATION
IN THE QUASI-BINARY MIXTURE OF GUAIACOL-GLYCEROL-WATER

By

Qingbiao Shi

April, 1994

Chairman: Dr. Andrew W. Cumming
Major Department: Physics

The kinetics of phase separation in a quasi-binary mixture of guaiacol-glycerol-water has been investigated using a time-resolved light scattering method following a sudden quench into the thermodynamically unstable state of the mixture. The mixture was confined between two optically transparent windows with thickness less than 1 mm. In addition to the common growth mode in the bulk, where the average domain size, L, grows as $t^{1/3}$ (where t is time), a novel growth mode was observed that the domain size L grows as t^b, where b increases from 1.1 to about 1.5, depending on the quench depth. As the same novel mode had been observed earlier in a polymer mixture, it is thus established that it is generic to all classes of binary fluids.

Experimental results from both the light scattering and video-microscopy suggested that the novel growth mode was closely associated with wetting phenomena of the two separating fluid phases near the glass surfaces. It was also dependent on the properties of the glass surface, which could be altered with a self-assembled monolayer of silane molecules. This experimental

evidence confirmed that the novel mode of phase separation was surface mediated.

CHAPTER 1

INTRODUCTION

The phenomena of phase-separation have been observed in a wide range of systems with two or more components. It has been an increasingly important process in material manufacturing and processing. Therefore comprehensive understanding is needed in both physical and chemical aspects of the phenomena. Over the last 30 years, experimental investigations have been conducted in alloys [Gaulin et al., 1987] and solid solutions [Hono and Hirano, 1987], simple binary solutions [Goldburg, 1983] and glass forming mixtures [Tomozava et al., 1970], and more recently, in liquid-polymer solutions [Sasaki and Hashimoto, 1984] and polymer-polymer blends [Hashimoto, 1988; Bates and Wiltzius, 1989], etc. On the theoretical side, efforts have been concentrated on elucidating the growth mechanisms that govern the kinetics of phase separation, especially those growth kinetics that are universal, depending only the general properties of the phase transition, e.g., the symmetries of the system and the order parameter, but not on specifics of the system.

Significant progress has been achieved so far in our understanding of the kinetics of phase separation, both in experiment and theory, especially in the last two decades. In classical theories, phase separation proceeds either through spinodal decomposition or through nucleation and growth [see, e.g., Gunton et al., 1983]. The former leads to the decay of an thermodynamically unstable state, through long wavelength fluctuations of infinitesimal amplitude. The latter is

1

due to the instability against localized (droplet-like) fluctuations with finite amplitude, and that leads to the decay of a metastable state. This distinction is clear in the mean field theory, as the unstable and the metastable states are separated by a so-called spinodal line in the phase diagram. Although later development has shown that the spinodal line is not well defined and the transition is not clear cut, it is still very helpful to distinguish these two from a thermodynamic point of view.

This chapter is a brief summary of the theoretical models, and a general comparison of their results with the experiments. As a number of excellent and extensive reviews have been written in the field [e.g. Gunton et al., 1983], here I will only discuss the key elements, and all the discussions will be concentrated on binary fluids from now on. First the phase diagram is presented along with the equilibrium properties, its general features can be readily understood in terms of some elementary thermodynamic arguments. And then I will discuss the thermodynamic unstability and metastability in terms of mean-field theory. Next Cahn's linear theory of spinodal decomposition is described, from which we can clearly see the difference of the early stage of decay from the unstable or metastable state. Some nonlinear modification is also mentioned, and it will be helpful later on to understand how the domain size is measured in a scattering experiment. Section 1.4 is a description on three key growth modes at later stages that have been clearly identified so far: droplet coalescence, evaporation and condensation [Lifshitz and Slyozov, 1961] and the hydrodynamic mode due to E. Siggia [Siggia, 1979]. Also in the same section, the dynamic scaling theory is discussed [Lebowitz et al., 1982]. And then a general comparison between experiment and theory is presented in section 1.5. Finally, we review the recent experimental observations and a general discussion on the wetting phenomena, which provided the motivations for the present work.

**1-PHASE REGION
(Miscible)**
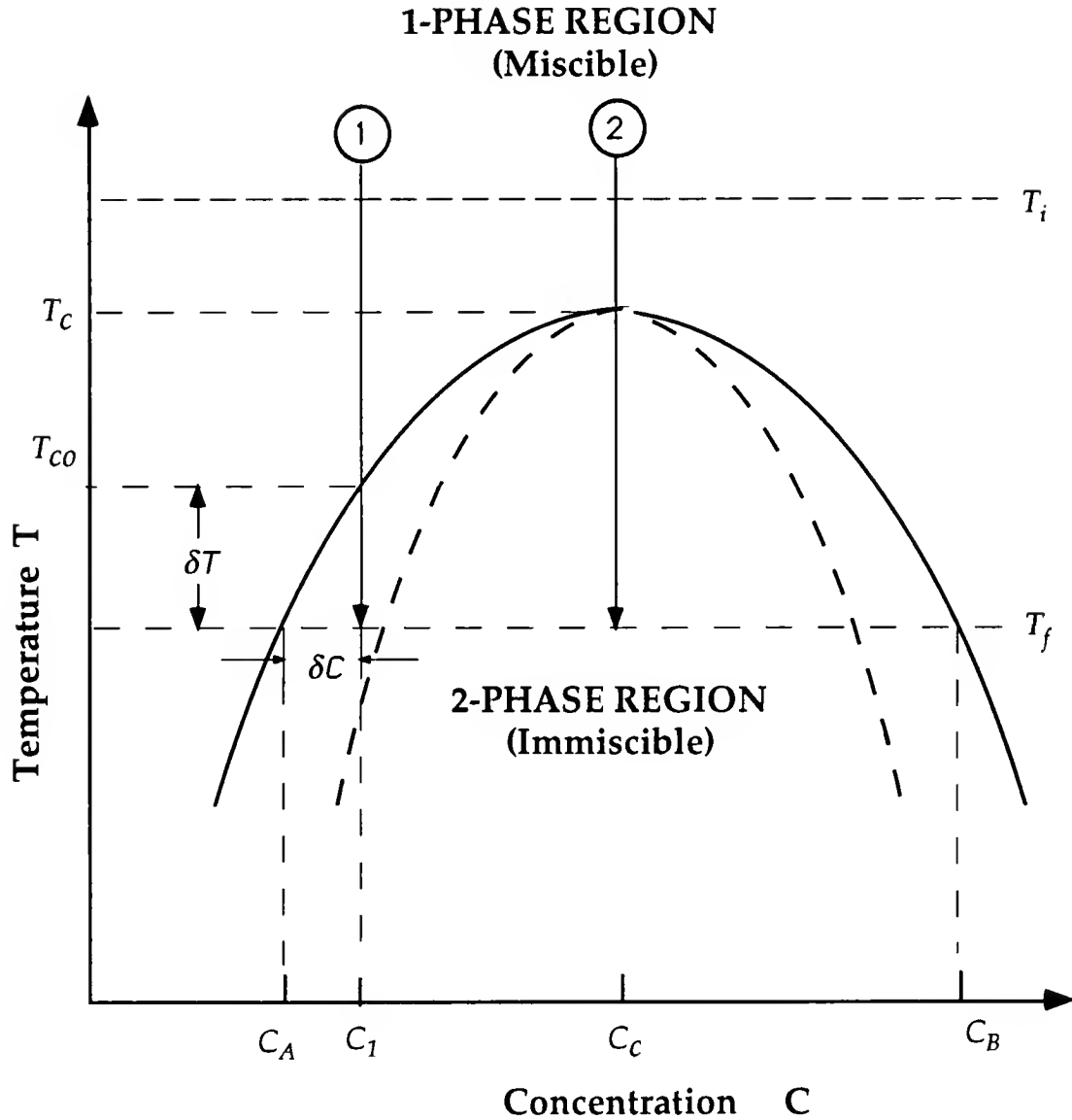
FIG. 1.1 The coexistence (solid) line and the spinodal line (dashed) in classical theory (mean field theory) for binary fluid. Two types of quenches are differentiated: (1) into the metastable state which is bounded by the coexistence and spinodal lines; (2) into unstable state bounded by the spinodal curve. In the first case the system is quenched into the metastable state by the depth δT, which corresponds to an initial supersaturation $\delta C = C_1 - C_A$. The phase separation eventually results in two phases, a major phase with concentration C_A, and a minor phase of C_B. The volume ratio of the two phases is given by the ratio $\delta C/(\Delta C - \delta C)$, where $\Delta C = C_B - C_A$.

1. 1 Phase Diagram

A generic phase diagram of binary fluids is shown in Fig. 1.1. The coexistence curve, also known as the binodal, divides it into two regions: the miscible region (one phase region or disordered phase) and the immiscible region (two-phase region or ordered phase). For binary fluids, the phase transition between the miscible phase and the immiscible phase is of second order, with the critical point at temperature T_c and critical concentration C_c. It is well known that the equilibrium properties of the fluids around the critical point belong to the universality class of the 3-d Ising model, where the properties around the critical point can be determined through:

$$\text{the correlation length} \qquad \xi = \xi_0 |t|^{-\nu}, \tag{1.1a}$$

where the critical exponent $\nu = 0.63$, and $t = (T - T_c)/T_c$, the reduced temperature, and

$$\text{the isothermal compressibility} \qquad K_T \sim |t|^{-\gamma}. \tag{1.1b}$$

with the corresponding exponent $\gamma = 1.3$. All the other critical exponents can be determined once two of them are known.

The qualitative features of the phase diagram can be readily understood in terms of the free energy F, the internal energy U and the entropy S:

$$F = U - TS$$

where T is the temperature in Kelvin. The equilibrium state has minimal free energy for given external conditions. For most fluids, the interactions between

the molecules are the van der Waals force, which is an attractive force due to the fluctuating induced dipole moments of the molecules. In most cases, the attractive force between the same species of molecules is much stronger than that of different species. Then the internal energy U will be minimized when the same species of molecules stay together, thereby favoring the phase separation. On the other hand, the entropy term has the temperature as a prefactor, so it is more important at high temperature. The entropy term will dominate over the internal energy above a certain temperature, the system will try to maximize its entropy and thus lower the free energy, then the fluids are miscible. At the other end, when the temperature is low, then the entropy term has minimal effects on total free energy F, and the internal energy term is more important, which is typically minimized when the like molecules stay together, so the fluids will try to keep away from each other. This explains the immiscibility at low temperature.

Most binary fluid systems have a similar phase diagram as Fig. 1.1, which is known as the upper critical solution temperature (UCST) type. There are other classes of mixtures whose phase diagrams are quite different; Fig. 1.2 lists several other common types. The opposite type to UCST is called the lower critical solution temperature (LCST) and behaves as shown in Fig. 1.2b, which has the immiscible phase at high temperature. This kind of behavior is due to some specific interactions between the different species of molecules in the mixture, e.g., hydrogen bonding. Some binary fluids can even show both UCST and LCST behavior, as described in Fig. 1.2c and 1.2d. Here I just want to mention particularly the closed-loop type of phase diagram as Fig. 1.2c, which shows a miscibility gap between the two critical temperature T_{cu} and T_{cl}, because the system involved in this study — Guaiacol-Glycerol-Water (GGW) shows this type of phase behavior.
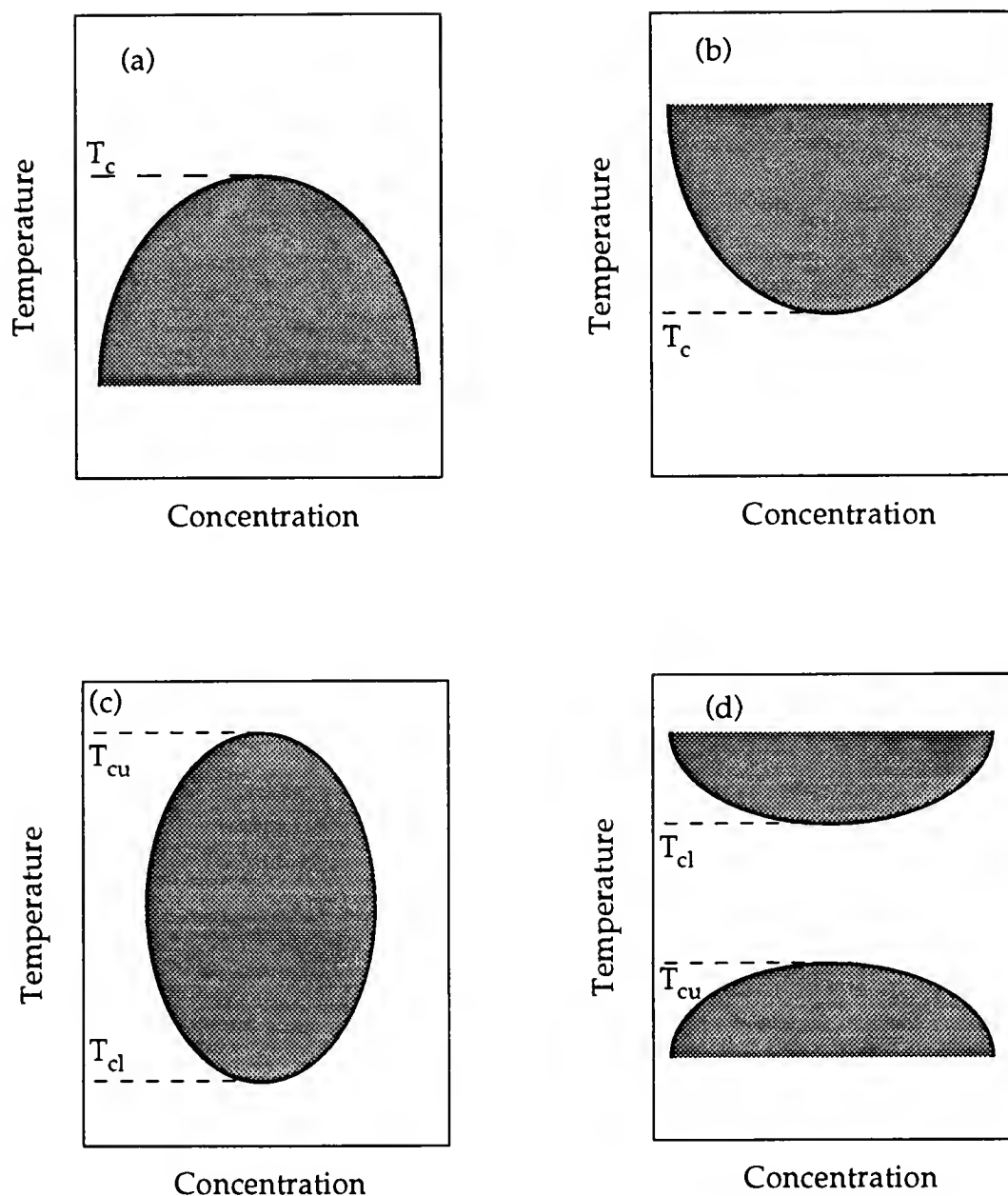
FIG. 1.2. Four types of phase diagrams of binary fluids are shown here schematically. The shaded area and beyond are the two-phase regions bounded by the coexistence curve. (a) is the most common, espcially if the fluids are nonpolar; All the other types usually involve some types of specific interaction, *e.g.*, hydrogen bonding between the molecules. The phase boundary is determined by the delicate balance of energy and entropy due to these interactions among the fluid molecules.

The closed-loop phase diagram, also known as a reentrant phase diagram, is due to the hydrogen bonding among the unlike species of molecules. One of the peculiarities of the hydrogen bond is that it is highly oriented; the bond will break if it sways beyond 10 degrees away from its optimal orientation axis. Due to this feature, hydrogen bonding effectively freezes the orientational degrees of freedom of the molecules, and hence decreases the compositional entropy of the mixture. At low temperature, the entropic contribution to the free energy will be minimal, so the hydrogen bonding between the unlikes strongly favors mixing. The close loop phase diagram can be understood as follows: at high temperature the fluids are miscible and the entropy is high. In this phase, the molecules mix together and are oriented randomly with respect to each other, and the entropy is maximized. As the temperature is lowered, internal energy due to van der Waals attraction becomes more important. At some point, it will dominate over the entropy contribution to the free energy and the fluids become immiscible, because the like molecules stay together which lowers internal energy. Now if we lower the temperature even further, the hydrogen bonding comes into play. And the mixture becomes miscible again by forming hydrogen bonds between the unlike molecules if the temperature is low enough, so the fluids reenter the miscible phase.

The close loop type of phase diagram can be elegantly fitted with the Walker-Vause (WV) model [Walker and Vause, 1980; Walker and Vause, 1983], which is an Ising-like lattice model, but each spin site can assume q different states. The Hamiltonian H of the model is

$$H = \sum_{<i,j>} [K_1(1 - \delta_{s_j s_i})\delta_{\sigma_i \sigma_j} + K_2(1 - \delta_{s_j s_i})(1 - \delta_{\sigma_i \sigma_j})] \qquad (1.2)$$

where the summation $<i,j>$ is over the nearest neighbor lattice sites. There are two sets of variables: s_i and σ_i, the spin variable s_i can be +1 (spin up) or -1 (spin down), which can also be designated as molecule species A or B respectively. The other site variable, σ_i, can take values 1, 2, 3,......q, which designates different orientational states of the molecules. If the two neighboring A and B molecules are in the same orientation state, i.e. $\sigma_A = \sigma_B$, then the energy is K_1, if not, the energy will be K_2. If we let $K_1 < K_2$, the Hamiltonian will simulate approximately the case of hydrogen bonding between the neighboring sites when they are in the same σ-state, and the number q is a measure of directionality of the hydrogen bond.

The phase diagrams of many binary fluid systems that exhibit the close loop have been fitted successfully by the WV model [Walker and Vause, 1983; Johnston, 1983], including the GGW mixture used in this study. From the molecular structures of guaiacol (2-Methoxyphenol) and glycerol (1,2,3-Propanetriol) and Water (Fig. 1.3), we can see the presence of multiple hydroxyl groups $-OH$, and the hydrogen bonding is a dominating factor in the mixing of the components. Strictly speaking, the system is a quasi-binary system, with a small amount of H_2O used in the mixture (less than 6% of the glycerol mass). Without the presence of this small amount of water, the guaiacol and glycerol will be miscible in any respective amounts. Only when a small amount of water is added to the mixture, a miscibility gap opens up in the phase diagram. The size of the immiscibility loop depends on the amount of water added. As it is well known, glycerol is highly hygroscopic; it will readily absorb the moisture from the surrounding air if the container is left open. On the other hand, the solubility of guaiacol in water is rather low; 70 ~ 80 cm^3 of water can only dissolve 1 g of guaiacol at room temperature. Therefore, most of the water

present will dissolve in glycerol, and glycerol-water effectively forms one component in the quasi-binary mixture, with guaiacol as the other .
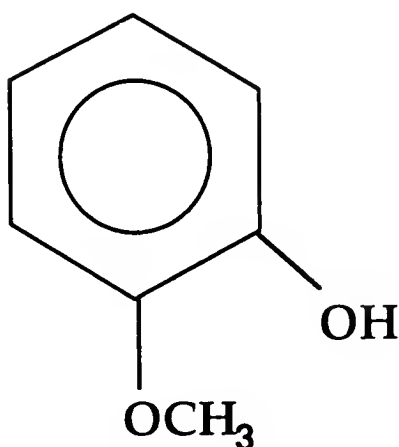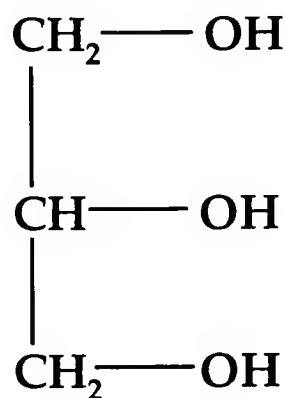
Guaiacol (2-Methoxyphenol) **Glycerol (1,2,3-Propanetriol)**

FIG.1.3 The molecular structures of guaiacol and glycerol. Due to the presence of the hydroxyl group - OH, hydrogen bonds can form between these groups of neighboring molecules. Water is also a strong hydrogen-bonding molecule.

1. 2. Mean Field Theory of Metastability and Unstability

Let us go back to Fig.1.1 and explain how a phase separation experiment is done in general. Assume a binary mixture is made up of two fluids, A and B, and the concentration of A is C_1.

Initially, the fluid mixture is set at temperature T_i, which is close to the coexistence curve but in the one-phase region. The fluid is miscible and is optically homogeneous. The temperature is suddenly and quickly changed to T_f,

inside the two-phase region. The sudden change in temperature is called a quench. Once inside the two-phase region, the fluid is either unstable or metastable. It will demix into the final equilibrium (stable) phases, which will have concentrations C_A and C_B that are at the coexistence curve at the temperature T_f. The final state of the fluid mixture is phase separated, and it consists of 2 phases of fluids: one is A-rich (concentration C_A), the other A-poor or B-rich (concentration C_B). To study the kinetics of phase-separating fluids, various experimental techniques can be used to monitor the growth of the domains after a quench.

The phase separation process starts as soon as the fluid is inside the two-phase region of the phase diagram. It is a nonequilibrium process because it concerns the transition from an unstable or metastable state back to equilibrium. Phase-separation kinetics is the study of this process of how the initially homogeneous fluid mixture demixes into heterogeneous phases. Some technical jargon should be made clear here. The temperature difference $\Delta T \equiv |T_f - T_i|$ is called the quench step, but a more relevant quantity is $\delta T \equiv T_{co} - T_f$, the quench depth (see Fig. 1.1); T_{co} is the temperature at which the fluid first crosses the coexistence curve. If the fluid is of critical concentration C_c, then $T_{co} = T_c$, the critical temperature, as shown in Fig. 1.1 by quench (2).

In the mean-field-approximation picture, the two-phase region is further divided into two regions: unstable and metastable. The boundary line between the two is shown as the dashed line in Fig. 1.1. This line is the so-called spinodal line. The fundamental assumption in the mean-field approximation is the existence of the free energy F as an analytic function of thermodynamic variables temperature T and concentration C, even inside the two-phase region. This may not to be true in general, because these are not equilibrium states inside the two-phase region. But as a starting point, the mean field picture is still very useful in

understanding the phase transition, and even some general features in the phase separation.

The mean field theory starts with the Ginzburg-Landau-like free energy functional $F(C, T)$, where C is the concentration in the case of binary fluids, and T is the temperature. In general, an order parameter ψ corresponding to the phase transition will take the place of the concentration C, e.g., the magnetization M in the case of ferromagnetic-paramagnetic transition.

The Ginzburg-Landau free energy functional $F(C,T)$

$$F\ (C,T) = \int_V d\vec{r}(f(C,T) + \frac{1}{2}k|\nabla C(r)|^2)\qquad(1.3)$$

where

$$f\ (C,T) = \frac{1}{2}a\ (C - C_0)^2\ +\ \frac{1}{4}u(C - C_0)^4\qquad(1.4)$$

and $a = A(T-T_c)$, $A > 0$, k, u are positive constants. The actual thermodynamic equilibrium state is determined through the minimization of F: $\left(\frac{\partial f}{\partial C}\right)_T = 0$, as the equilibrium means the lowest energy state possible, therefore most stable. Notice that a changes from positive to negative as T is varied from the upper side of T_c. Then the shape of $f(C,T)$ as a function of C changes as T crosses T_c: At $T > T_c$, F has only one minimum at $C = C_0$; (see Fig. 1.4 for details). At $T < T_c$, C_0 is no longer an absolute minimum, instead two minima appear at

$$C = C_0 \pm \sqrt{\frac{|a|}{u}}\qquad(1.5)$$

The coexistence curve (binodal line) is determined by the equation:

$$\mu = \left(\frac{\partial f}{\partial C}\right)_T = 0, \tag{1.6}$$

and we can introduce a susceptibility χ:

$$\chi = \left(\frac{\partial^2 f}{\partial C^2}\right)_T \tag{1.7}$$

and the line defined by $\chi = 0$ is the spinodal line. Inside the two-phase region of the phase diagram (see Fig. 1.1), the area between the binodal and spinodal line corresponding to the metastable state, since with $\chi > 0$, a small fluctuation of the concentration $C(r)$ will increase the energy, an energy barrier which needs to overcome before the system can decompose and phase separation can occur. In contrast, the area inside the spinodal line corresponds to the unstable state, because with $\chi < 0$ any spontaneous small fluctuation will drive the system to lower free energy, and the system can phase separate without having to overcome an energy barrier.

The phase separation process is thus the decay of the unstable or metastable state into equilibrium states. Due to the difference in metastability and unstability, the phase separation proceeds differently in general. If the fluid is quenched into the unstable region of its phase diagram, the phase separation is said to proceed via spinodal decomposition. On the other hand, it proceeds via nucleation and growth after being quenched into the metastable state. From the phase diagram, we can see that the unstable region usually has the initial concentration fairly close to the critical concentration C_c, while the metastable part corresponds to concentration further away from C_c, for off-critical quenches.
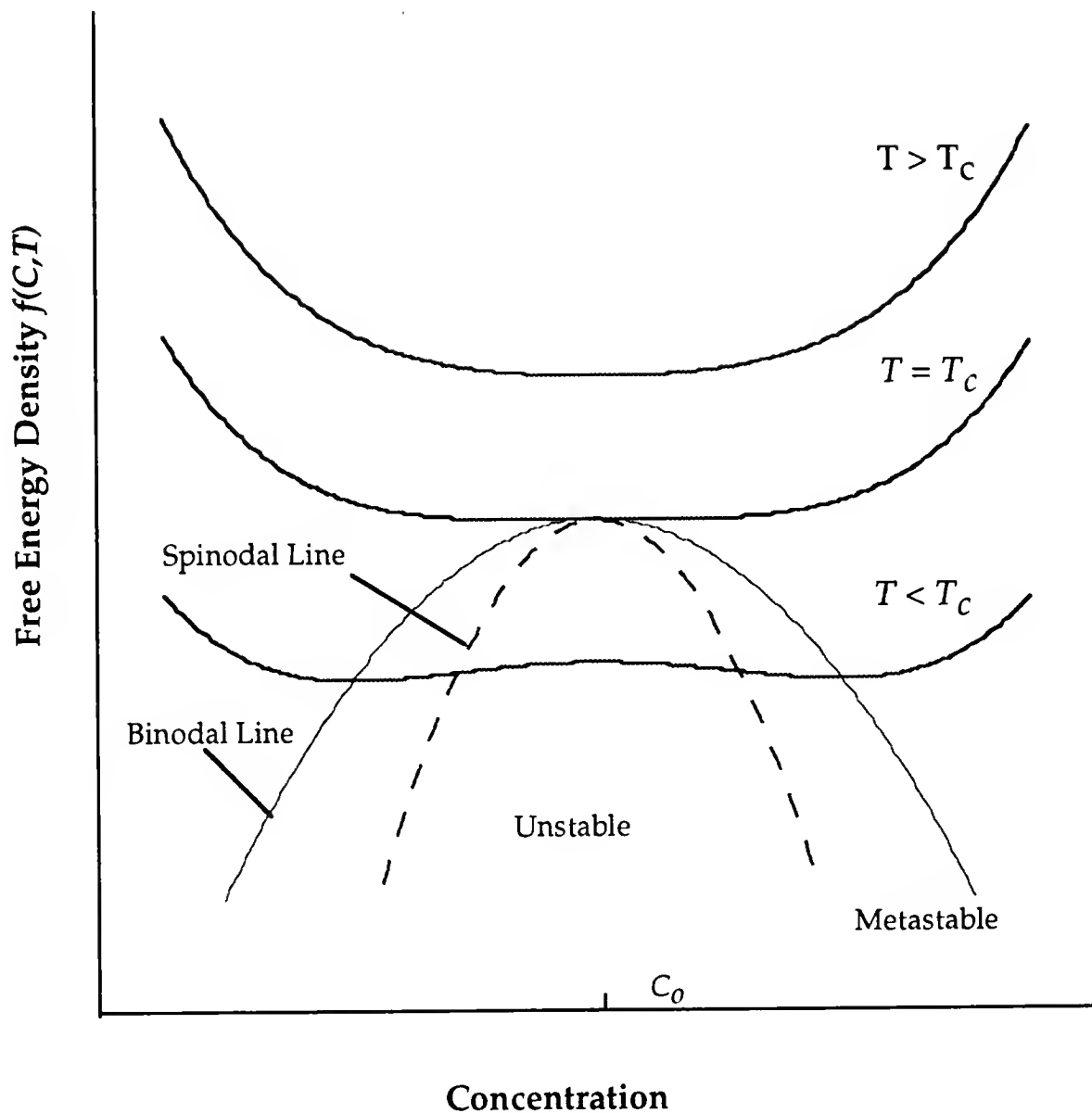
FIG. 1.4 The Ginzburg-Landau form of the free energy density $f(C, T)$ (eq. (4)) at tempertures around critical temperature T_c. At $T > T_c$, f has only one minimum at C_0. But at $T < T_c$, double minima are present, indicating two phases. The coexistence curve (binodal line) can be derived from $f(C,T)$ by eq.(1.6) and the spinodal line by the susceptibility $\chi = 0$ (see eq.(1.7)).

It is important to determine the validity of the mean-field theory. Remember the basic assumption in the theory is that the fluctuations in the system is small compared to the mean value (statistical average). In many cases, it is not valid around the critical point of a phase transition, where the fluctuations are significant. Furthermore, the existence of a free-energy functional in a nonequilibrium state, as inside the two-phase region, is somewhat in doubt. Therefore the validity of the mean field treatment is uncertain, especially near the spinodal line. In fact, it has been shown using the renormalization group method that the spinodal line shifts as a function of the renormalization size L [Langer, 1974; Binder et al., 1978; Kaski et al., 1983]. It is now generally accepted that the spinodal line is not sharp, and the transition from metastable and unstable states is gradual. However, despite all these problems, the mean field theory still provides a simple and elegant picture about the phase transition and its dynamics.

1.3 Cahn's Linear Theory of Spinodal Decomposition

Cahn's treatment of spinodal decomposition is one of the pioneering steps toward the understanding of the general phenomena of the dynamics of phase transition. In a series of papers [Cahn, 1961; 1962; 1966; 1968], Cahn outlined a linearized theory of spinodal decomposition, and concluded an exponential growth of the order parameter occurs at the early stage following the quench into the unstable region of the phase diagram. In the case of phase separation in binary fluids, the order parameter is the local concentration $C(r)$, which is conserved (the molecules of each species do not simply disappear.), in contrast to some other systems where the order parameter is not conserved. A simple case

with nonconserved order parameter is the Ising-like spin system, where spins are allowed to flip. This system can be made to simulate the binary fluid system when the spin flipping is prohibited (so-called spin-exchange models), then the number of up-spins or down-spins is conserved.

The linearized theory can be generally regarded to describe the phase separation as a diffusion process. The diffusion constant D is proportional to χ, which is the susceptibility, as defined in eq. (1.7). Inside the unstable region, where $\chi < 0$, D is negative, the diffusion is along the concentration gradient, therefore achieving phase separation. Conservation of the order parameter is expressed in the continuity equation:

$$\frac{\partial C(\mathbf{r})}{\partial t} + \nabla \cdot \mathbf{j} = 0 , \tag{1.8}$$

where $\mathbf{j}$ is the interdiffusion current

$$\mathbf{j} = -M \, \nabla \mu (\mathbf{r}) , \tag{1.9}$$

and M is the mobility, and $\mu(r)$ is the local chemical potential, which can be related to the free energy F:

$$\mu (\mathbf{r}) = \frac{\delta F}{\delta C(\mathbf{r})}. \tag{1.10}$$

So if we use the Ginzburg-Landau free energy functional F shown in (1.3), we get the following equation

$$\frac{\partial C(\mathbf{r})}{\partial t} = M \nabla^2 \{ -K \, \nabla^2 C + \frac{\partial f}{\partial C} \} \tag{1.11}$$

Cahn linearized this nonlinear equation about the average concentration C_0, and obtained

$$\frac{\partial u(\mathbf{r})}{\partial t} = -M\left[-K \nabla^2 + \left(\frac{\partial^2 f}{\partial C^2}\right)_{C_0}\right] u(\mathbf{r}) \qquad (1.12)$$

where

$$u(\mathbf{r}) \equiv C(\mathbf{r}) - C_0 \qquad (1.13)$$

Note in the long wavelength limit, the term $K \nabla^2$ can be ignored. Then we have a diffusion equation, with a diffusion constant

$$D = M\left(\frac{\partial^2 f}{\partial C^2}\right)_{C_0} \qquad (1.14)$$

Fourier transform eq.(1.12) respect to space leads to the following

$$\frac{\partial \tilde{u}(k)}{\partial t} = \omega(k)\,\tilde{u}(k) \qquad , \qquad (1.15)$$

here $\tilde{u}(k)$ is the Fourier component of $u(r)$ and

$$\omega(k) = -M\,K\,k^2\left(k^2 + K^{-1}\left(\frac{\partial^2 f}{\partial C^2}\right)_{C_0}\right) \qquad (1.16)$$

and the shape of ω as a function of k is shown in Fig. 1.5. Inside the spinodal region where χ is negative, ω is positive for $k < k_c$ where

$$k_c = K^{-1}\left|\left(\frac{\partial^2 f}{\partial C^2}\right)_T\right|. \qquad (1.17)$$

So the long wavelength fluctuations will grow exponentially in the spinodal region. Notice ω reaches its maximum at $k_m = k_c/\sqrt{2}$.

The experimentally more relevant quantity is the structure function $S\ (k,\ t)$ $= \langle|\tilde{u}\ (k)|^2\rangle$, which is the Fourier transform of the two-point correlation function. It can be measured by the scattering methods commonly used in physics (X-ray, light, *etc.*). Cahn's theory thus predicted an exponential growth

$$S\ (k,t) = S\ (k,0)\ exp(\ 2\ \omega(k)\ t) \tag{1.18}$$

Therefore at the initial stage, the spinodal decomposition should undergo an exponential growth in time in the scattering intensity for $k < k_c$, and the intensity profile has a peak at k_m , which does not change during this stage of growth. Due to the fast growth, the peak wave number k_m will soon dominate over the other length scale. As a result, k_m characterizes the typical size of the domain seen in spinodal decomposition experiments.

The linearization can only hold at the very early stage of spinodal decomposition when the fluctuation amplitude is small, and beyond that nonlinear effects will become important. This exponential-growth stage passes too quickly to be observed experimentally in most of the physical systems such as binary fluids, with the exception of the polymer blends, where due to its high viscosity, the dynamics is slowed down tremendously.

Here it is convenient to point out the difference in dynamics if the order parameter ψ is not conserved. The corresponding equation to eq.(1.12) can be obtained by replacing $M \nabla^2$ in eq. (12) by $- M$,
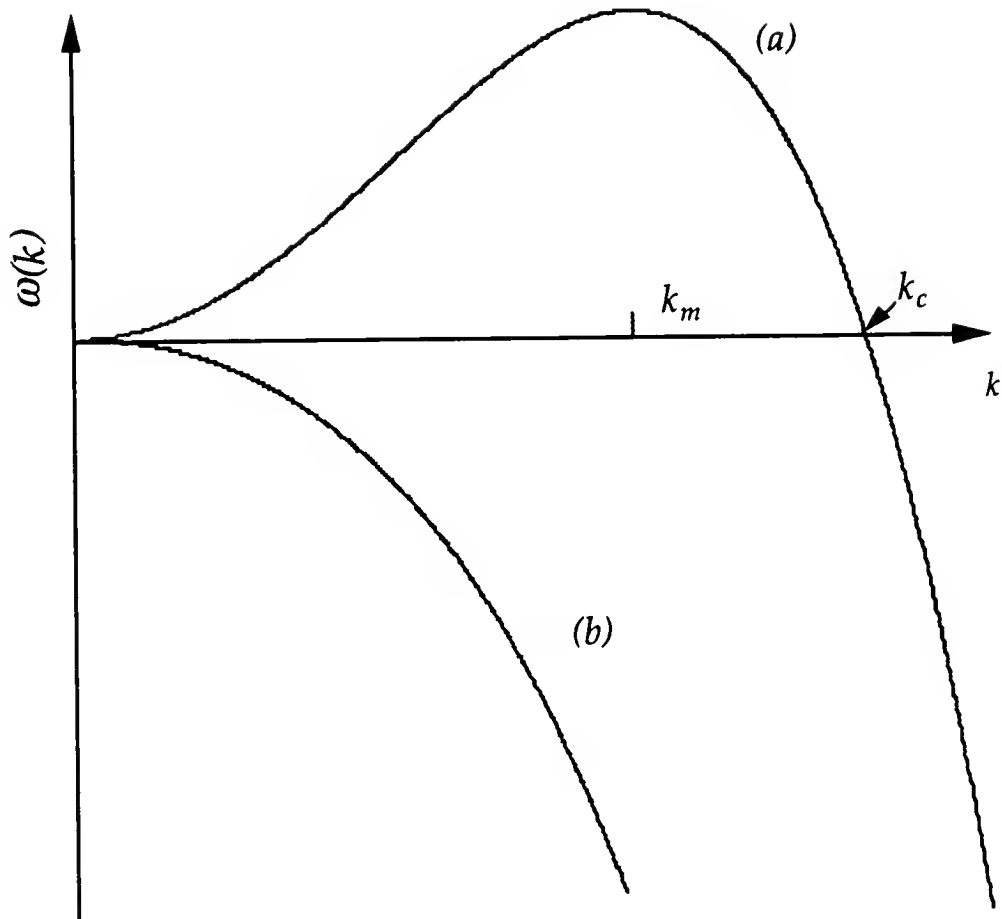
FIG. 1.5 The growth rate as predicted by the linear theory for (a) a unstable quench, (b) a metastable quench. In the linear theory, the peak which has maximum rate is wave number k_m, which doesn't change with time. But if nonlinear effect are incorporated, k_m will shift toward smaller k as time proceeds.

$$\frac{\partial \psi(r)}{\partial t} = -M \left[-K \ \nabla^2 + \left(\frac{\partial^2 f}{\partial C^2} \right)_{\!co} \right] \psi(r) \tag{1.19}$$

and the corresponding rate of growth

$$\omega(k) = -M\left(k^2 + K^{-1}\left(\frac{\partial^2 f}{\partial C^2}\right)_{C_0}\right) \tag{1.20}$$

Here the maximal growth occurs at $k = 0$ instead of at some wave number k_m.

An important extension to Cahn's linear theory was made by Cook [Cook, 1970]. He observed it was necessary to add a noise term to eq. (1.12) to have a correct statistical description of the dynamics in alloys. The noise arises from the random thermal motion of the atoms or molecules in the system. Within the context of linear theory, the noise term does not affect the major results we have discussed so far.

Attempts have been made to include the nonlinear effects. Immediately we encounter an equation that includes higher order correlation functions, and it leads to the typical hierarchy of coupled equations. So some kind of truncation approximation has to be employed. One of the simplest schemes is due to Langer, Bar-on and Miller (LBM) [Langer et al., 1975], which assumes the odd order-n two-point functions are zero, and if we only keep the first higher order correlation function $S_4(k)$, which is related to the normal, or second order, two-point correlation function $S(k)$ $(= S_2(k))$ as follows

$$S_4(k) = 3\langle u^2 \rangle S(k) \tag{1.21}$$

with

$$\langle u^2(t) \rangle = (2\pi)^{-3} \int d\vec{k}\, S(k) \tag{1.22}$$

then the correction to the linear theory is the replacement of $\left(\frac{\partial^2 f}{\partial C^2}\right)_{C_0}$ by

$$\left(\frac{\partial^2 f}{\partial C^2}\right)_{C_o} + \frac{1}{2}\left(\frac{\partial^4 f}{\partial C^4}\right)_{C_o}\langle u^2(t)\rangle \qquad (1.23)$$

Consequently k_c will decrease as $\langle u^2(t)\rangle$ increases with time, (see eq. (1.17)), and the peak k_m in the scattering profile will shift toward to lower k, indicating growth of the domain structure. This coarsening behavior is qualitatively accurate for the early stage of spinodal decomposition.

Another effect that is specific to fluids is hydrodynamic motion, which has not been included into consideration so far. Efforts have been made to take it into account [Kawasaki and Ohta, 1978], and it brought significant modification to the LBM results. But its agreement with experimental data is still only qualitative. Hydrodynamics will have a significant effect at the later stage of coarsening, and we will discuss it in the next section.

1.4 Later Stage Coarsening

It is difficult to develop a theory for the later stage, that is the coarsening process of phase separation. The main difficulties stem from the nature of nonequilibrium and nonlinearity in the phase separation process itself. So far our understanding at the later stage of phase separation remains qualitative. Most of the theories attempt to find universal growth laws and mechanisms in some simple scenarios. But in real systems there is no way to make these distinctions, many of these mechanisms are at work at the same time. The following discussion in section 1.4.3 is largely based on the paper by Siggia [Siggia, 1979], who discussed the key coarsening mechanisms responsible at the later stage of phase separation, especially the hydrodynamic effects.

The division of the phase separation process into early and later stages is somewhat vague. Qualitatively the later stage starts after domains of two distinct phases have formed, *i.e.*, the concentrations of the domains have reached C_A and C_B, respectively, so the driving force is mainly derived from the minimization of the domain wall, namely the reduction of the interface area and thickness.

1.4.1 Droplet Coalescence

Droplet coalescence, also known as coagulation, is the recombination process of small droplets (usually of liquids) upon encounter. As a result, larger droplets form as more and more small ones bump into each other and recombine into larger ones. It is readily observed in colloids and aerosols, in which aggregates form. In binary fluids, we can imagine the minor phase may form a suspension of small droplets in the medium of the majority phase at later stage, (in the case of Fig. 1.1, the majority phase is the A-rich phase with concentration C_A, and the minor phase is B-rich with concentration C_B). Small droplets have larger surface-to-volume ratio compared to larger ones, so the energy can be reduced by recombining into large droplets.

Consider a droplet with radius R_1, fixed at the origin and surrounded in a mist of droplets with radius R_2, with number density n_0. The motion of the droplets are Brownian, *i. e.*, diffusive. And the number of droplets that collide into the drop in the origin and thus recombine can be calculated through the diffusion equation :

$$\frac{\partial n}{\partial t} = D \frac{1}{r^2} \frac{\partial}{\partial r}\left(r^2 \frac{\partial n}{\partial r}\right)$$

(1.24)

with the boundary conditions

$$n = n_0 \qquad \text{for } r > R_1 + R_2 \text{ at } t = 0$$

$$n = 0 \qquad \text{for } r = R_1 + R_2 , \ t > 0, \qquad (1.25)$$

$$n = n_0 \qquad \text{for } r \to \infty$$

The number of collisions per unit time I can be calculated (see, *e.g.*, Levich, 1962) as

$$I = 4 \pi (R_1 + R_2) D_2 n_0, \qquad (1.26)$$

where D_2 is the diffusion constant of droplets with radius R_2, which are related through the Einstein relation

$$D_2 = \frac{k_B T}{6\pi \rho v R_2} \qquad (1.27)$$

where ρ is the density, v is the kinetic viscosity of the medium, and k_B is the Boltzmann constant.

In reality the droplet at the origin is moving as well; then the number of collision per unit time per volume is

$$I_{1,2} = 4 \pi (R_1 + R_2) (D_2 + D_1) n_1 n_0, \qquad (1.28)$$

Assuming that droplets are approximately monodisperse at a given moment, then the number density will decrease due to the recombination as

$$\frac{dn}{dt} = -16\,\pi\,D\,R\,n^2 \tag{1.29}$$

where we have set $D_1 = D_2 = D$, and $R_1 = R_2 = R$.

From eq. (1.27), $(D\,R)$ is independent of the time, we can find

$$R^3 = 12\,(DR)\,v\,t \tag{1.30}$$

where v is the volume fraction of the droplets. We get from this simple model of droplet coalescence that the droplet size grows as $t^{1/3}$ approximately.

In the above simplistic droplet coalescence model, the droplets are treated as free particles and the medium is static, and all the interactions between the droplets are neglected. The reality is that both medium and the droplets are fluids, and they are undergoing hydrodynamic motion. At the level of droplets, they have to squeeze aside the liquid along the way upon approach. We can imagine that will slow down the recombination rate of droplets. In his paper [Siggia, 1979], Siggia took into account both the effects of the hydrodynamics and the van der Waals forces between the droplets. He found the correction to eq. (1.30) as following

$$R^3 \sim \frac{(DR)\,v\,t}{\log\,(R)} \tag{1.31}$$

So at the later time R still grows as $t^{1/3}$ asymptotically.

In the above argument we have explicitly assumed the spherical droplets, which means that the above coalescence model can only apply when the volume fraction of the minor phase v is small, so the minor phase forms the isolated droplets. In this picture, the process is distinctively nucleation and growth. However, it has been argued [Voorhees and Glicksman, 1984; Huse, 1986] that the $R \sim t^{1/3}$ law still applies, when the morphology is far from spherical, as in the case of spinodal decomposition.

1.4.2. Lifshitz - Slyozov Theory

As mentioned before, the Lifshitz-Slyozov (LS) theory [Lifshitz and Slyozov, 1961] is one of the few well established results in the field of phase transition kinetics. The change from metastable to stable phases occurs as a result of fluctuations, which form a new phase or nuclei out of the original homogeneous medium. There are two main factors contributing to the energy of these nuclei, and thus determine their stability. They are the free energy of the nuclei and the surface energy due to the creation of the interface. The former is negative in the metastable state, because the nuclei usually have energy of the equilibrium state, and it is proportional to the volume of each nucleus. On the order hand, the creation of an interface always costs energy. It is positive and proportional to the surface area of the individual nucleus. The competition between the two terms results that those nuclei smaller than a critical radius R_{cr} unstable, due to their lower volume-to-surface area ratio, and thus tend to evaporate, while those larger than R_{cr} are stable and thus grow larger. The larger nuclei grow at the expense of the smaller ones, thus Lifshitz-Slyozov theory is also known as the evaporation-condensation mechanism.

The coarsening process is still governed by diffusion. In the limit of small supersaturation, the diffusion gradient will be small. And we can use the steady state approximation to the diffusion equation

$$\nabla^2 C = 0 \tag{1.32}$$

with appropriate boundary conditions. From the solution, one can obtain the growth rate equation (see, e.g., Lifshitz and Pitaevskii, 1981)

$$\frac{dR}{dt} = \frac{D}{R} \frac{\delta C}{\Delta C} \left(1 - \frac{R_{cr}}{R}\right) \tag{1.33}$$

where $\delta C(t) = C(t) - C_A$ is the supersaturation, and $\Delta C = C_B - C_A$. If the radius of the droplet $R > R_{cr}$, then $dR/dr > 0$, it grows. And if $R < R_{cr}$, then $dR/dt < 0$, it shrinks and eventually evaporates. The critical radius R_{cr} is related to the supersaturation through

$$R_{cr}(t) = \alpha / \delta C (t) \tag{1.34}$$

where α is a constant proportional to the surface tension σ.

The distribution function $f(R,t)$ satisfies the continuity equation

$$\frac{\partial f(R)}{\partial t} = - \frac{\partial}{\partial R} \left[v(R) f(R) \right] \tag{1.35}$$

where $v(R)$ is the radial velocity, given by the eq. (1.34), and $f(R)dR$ is the number density of nuclei with radius between R and $R + dR$. And finally, we have the conservation of the solute

$$\frac{\delta C_0 - \delta C(t)}{\Delta C - \delta C(t)} = \frac{4\pi \overline{R}^3}{3} N \qquad (1.36)$$

where δC_0 is the initial supersaturation, N is the number of the nuclei droplet per unit volume and $\frac{4\pi \overline{R}^3}{3} N$ is the average volume of the nuclei..

Lifshitz and Slyozov were able to obtain the asymptotic solution to the above coupled equations. Besides the distribution function $f(R,t)$, they found the growth law

$$\overline{R}^3(t) = \frac{4}{9} D\alpha\, t \qquad (1.37)$$

This LS theory is only strictly true at small supersaturation, when the volume ratio of the minor phase to the major phase is small. With increased volume ratio, significant deviation from LS theory has been found. Hence, unlike the previous model of droplet coalescence, LS mode of growth is specific to the decay of metastable state, $i.\ e.$, to the nucleation and growth.

1.4.3. Hydrodynamic Growth Mode in Concentrated Mixture [E. Siggia, 1979]

The observation of phase separation of binary fluids reveals two types of distinct morphologies at later stage. One type is usually seen in systems with small volume ratio, so there is clearly a minor phase and a major phase. In this case, the minor phase grows as isolated spherical droplets in the medium of the major phase. However, in the systems where the volume ratio of the two phases is comparable, as in spinodal decomposition of a near critical concentration, a

different type of morphology emerges: the structure of a jumbled network of interpenetrating tubes. An idealization of the structure is two interconnecting 3-d networks of A and B phases, like those that have been clearly identified in the amphiphilic systems. This change of morphology is gradual as the volume ratio is increased.

At the later stage of growth, we expect that two distinct phases have formed that and the interface between the two phases is well defined and has a definite surface tension, σ. In the concentrated mixture, the two phases exhibit the morphology of an interpenetrating tube-like network. Siggia has pointed out that the tube-like structure is unstable against pinching. This can be readily understood from the Laplace formula

$$p = \sigma\left(\frac{1}{r_1} + \frac{1}{r_2}\right) \tag{1.38}$$

where p is the pressure difference between two sides of the tube, and r_1 and r_2 are the principal radii of curvature at a given point on the surface of the tube. As shown in Fig.1.6, when a tube is pinched at a given point, the pressure p at the point will increase due to the decrease of r's, that will push the fluid away from the point of pinching, and decrease the radius even further.

Siggia proposed a novel mechanism of growth due to the instability of the tube-like structure in binary fluids. Image a long wavelength disturbance along the axis of a tube of radius R, where the wavelength $l \gg R$. According to eq. (1.38), it will lead a pressure gradient $\sim \sigma/R\, l$ along the tube axis, that will tend to transfer the liquid from the neck to the bulges. The corresponding average velocity due to the Poiseuille flow is

$$v \sim 0.1 \, \sigma R/l \, \eta \qquad\qquad (1.39)$$

Take this as the rate of growth dR/dt, then

$$R \sim (0.1 \, \sigma/\eta) \, t \qquad\qquad (1.40)$$

The prefactor 0.1 is only based on rough estimations, and η is the shear viscosity of the fluid. As a results of the hydrodynamic flow, the coarsening

(a) (b) (c)
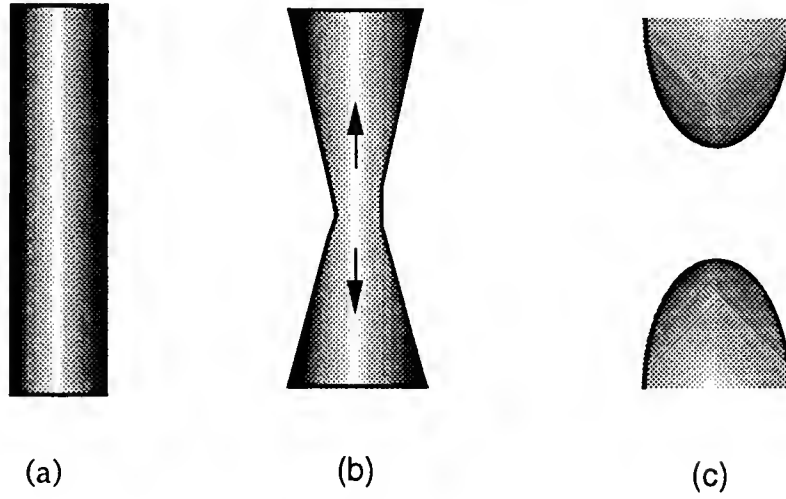
FIG. 1.6 The tube-like structure is unstable against the pinching, which will lead to the eventual breakdown of the tube. (a) shows a section of tube which forms the interface between the two phases; (b) As the tube is pinched, the pressure inside the tube at the pinching site increases according to eq. (38), which consequently induce a pressure gradient that push the fluid away from the pinching site (as indicated by the arrows), and that further shrinks the tube, and eventually the tube breaks down, as shown in (c).

induces the growth to be linear with time. It is not essential to assume tube-like structure in the above argument. At the concentrated mixture, any kind of nonflat interface may induce this type of coarsening.

The above mechanism is observed in the spinodal decomposition of binary fluid. Up to now, the general consensus on the process is that early on the diffusive mode dominates, *i.e.*, the domain grows as $t^{1/3}$, when the interface may not yet be well defined and the hydrodynamic growth mechanism by surface tension is not possible. Gradually there is a crossover from the diffusive growth to the faster hydrodynamic growth regime, and domain size grows as t. In the nucleation and growth process, the surface tension does not come into play, and consequently the growth should be diffusive for all times.

1.4.4. Scaling Hypothesis for Structure Function at the Later Stage

The renormalization group has brought a revolutionary leap to our understanding of critical phenomena and phase transitions. At the basic level, it is recognized that the correlation length ξ is divergent at the critical point. As a result around the critical point, the only relevant length scale is ξ, and at length scales $L \ll \xi$, the physical system is scale invariant. Or simply put, the system looks self-similar at any scale L exactly at critical point, where $\xi \rightarrow \infty$. Then the thermodynamic functions scale around the critical point with respect to ξ. And these functions only depend on some very general properties of the Hamiltonian of the system, like the symmetry of the system and the space dimensions of the system and order parameter, but not on the details of the interactions in the system. This enables us to classify phase transitions into different broad universality classes, in which all the systems in the same class have the same properties around the critical point.

So far the quantities involved are the equilibrium quantities such as the heat capacity, susceptibility, *etc.* It is tempting to extend the same type of argument into the dynamic aspect of the phase transitions. But so far it has proven to be much more difficult. The dynamic properties of system seem to be more system specific then the static quantities around the critical point. However, it is still desirable to apply similar concepts to the dynamic aspects of the criticality, which is the so-called dynamic scaling hypothesis.

The most important function in the kinetics of phase-separating is the 2-point structure function $S(k,t)$. The basic idea of the dynamic scaling hypothesis in this case is as follows: After an initial period of transient time following the quench, a characteristic length scale $l(t)$ is well established which represents the average size of the domain structure. The $l(t)$ is the only relevant length in the problem, and it plays the similar role as the correlation length ξ in the critical phenomena. Then the structure function $S(k,t)$ is scale invariant if all its lengths are scaled relative to $l(t)$.

The definition of the characteristic length scale $l(t)$ may vary. For example, in experiment where $S(k,t)$ is measured, it is convenient to choose the inverse of the peak position, $k_m^{-1}(t)$. In the case of computer simulation studies, k_1^{-1} is usually used, where k_1 is the first moment of the structure function $S(k,t)$. In this study, we will stick to the peak position $k_m^{-1}(t)$. Let us first introduce a normalized structure function $\widetilde{S}(k,t)$:

$$\widetilde{S}(k,t) = \frac{S(k,t)}{\sum_{k} k^2 S(k,t)}$$

so that $\sum_{k} k^2 \widetilde{S}(k,t)$ is independent of time.

Then the scaling hypothesis assumes the renormalized structure function has the following form

$$\widetilde{S}(k,t) = k_m^{-d}F(k/k_m) \qquad (1.41)$$

where d is the dimensionality of the system. The functional form of $F(x)$ is universal to some degree. In the phenomenological theories of Furukawa [Furukawa, 1977; 1978; 1979; 1985.], a family of functions $F(x)$ is proposed

$$F(x) = \frac{(1 + \gamma/2)\,x^2}{\gamma/2 + x^{2+\gamma}} \qquad (1.42)$$

where the constant γ is related to the dimension d: (1) Critical quench, $\gamma = 2d$; (2) Off-critical quench, $\gamma = d+1$.

As a result of the scaling hypothesis (1.42), the time t only enters the structure function through $k_m(t)$. Otherwise the structure function $S(k,t)$ doesn't depend on time explicitly. In addition, if we let $k = k_m$ in equation (1.42), we will have

$$\widetilde{S}(k_m) \sim k_m^{-d} \qquad (1.43)$$

If plotting on log-log axes, it is a straight line with slope $-d$.

Another straightforward result from eq. (1.41), if it is true, is that the ratio of the second moment of the structure function, $k_2(t)$, to the square of the first moment $k_1(t)$,

$$r(t) = \frac{k_2(t)}{k_1^2(t)} \qquad (1.44)$$

should be independent of time t.

The scaling behavior was noticed first in the computer simulations of phase separation process in Ising-like lattice models, where the structure function satisfies (1.42) at later stage. In the simple binary fluids, it has been shown experimentally that it holds approximately. But the function form $F(x)$ can vary with temperature, quench depth, and concentrations. We should only take (1.42) as a first order approximation, as various type of corrections may be present in real systems.

I have summarized the key mechanisms related to the phase separation in the binary fluids. Rather than attempting to give an exhaustive list of the results, I chose to concentrate on several key elements and well established models instead. In terms of results, I have ignored most of the contributions from the computer simulation studies, except just to say that most of the results are consistent with the experiments.

Our understanding of the phase separation process is still very limited, *e.g.*, we are unable to calculate some of the most important and basic quantities like the correlation functions and thus the structure factor, which can be directly measured experimentally. The intrinsic problems about the process are its nonlinearity, which we still do not know how to deal with analytically, and the fact that it is a nonequilibrium process. Most of our current knowledge in this field is qualitative, restricted to the certain modes of growth laws. It is not surprising to see that new phenomena still being discovered over the years. The phenomena of spinodal decomposition and nucleation and growth are far richer and complex than the current models have suggested.

1.5 Experimental Results

As I have mentioned, the phase separation phenomena have been studied in a variety of systems. Among these, the most detailed studies have been conducted in alloys, binary fluids and polymer blends. Here we will concentrate on the results from binary fluids, and furthermore limit our discussion mostly to the spinodal decomposition process in critically quenched systems.

The binary fluid systems used most in the phase separation experiments are 2, 6 lutidine - water (L-W), and isobutyric acid - water (I-W), as pioneered by Goldburg and coworkers [Chou and Goldburg, 1979; 1981], and Knobler and coworkers [Wong and Knobler, 1978; 1979; 1981; Knobler and Wong, 1981]. Later the French group headed by Beysens [Guenoun et al., 1987] used a quasi-binary system, deuterated cyclohexane (D-cyclohexane) - cyclohexane - methanol, which has the advantage of density matching between methanol and the D-cyclohexane -cyclohexane mixture of the right proportion, thereby minimizing the effect of gravity.

All three groups used time-resolved light scattering to probe the evolution of the phase separation. I will discuss the details of the techniques later. Following a temperature or pressure quench of the system into the unstable state, the mixture will turn milky and thus starts to scatter light strongly. Because fluids are isotropic, the scattered light forms a ring, known as the spinodal ring, which brightens and decreases in its diameter as time proceeds. Experimentally the scattered light intensity profile $I(q,t)$ is measured, where q, the momentum transfer, is a function of the scattering angle θ. We can determine the ring diameter $q_m(t)$ and the peak intensity $I(q_m,t)$. When the multiple scattering effect is small and can be ignored, $I(q,t)$ is proportional to the structure function $S(q,t)$,

then q_m^{-1} represents the average length scale of the structures growing in the phase separating mixture, and therefore we can directly compare with theories.

If the quench depthes are well within the critical region, it is natural to use the scaled variables k and τ,

$$k = q\,\xi \qquad \text{and} \qquad \tau = Dt/\xi^2 \qquad (1.45)$$

where ξ and D are the correlation length and diffusion coefficient, respectively. In these dimensionless variables, the evolution of k_m vs. τ falls remarkably onto a single curve for quenches of different depths. Experimental results from different binary systems showed excellent agreement [Goldburg, 1983]. In the two opposite limits $k_m \approx 1$ and $k_m \ll 1$ the growth can be approximated as a power law:

$$k_m = A\tau^{-b}$$

and the kinetic exponents are

$$b = 0.3 \pm 0.1, \qquad \text{for } 0.6 \geq k_m \geq 0.3,$$

$$b = 1.1 \pm 0.1 \qquad \text{for } 0.1 \geq k_m \geq 0.08.$$

There is a gentle crossover between the two limits. This is just what the theories predicted for the coalescence process. In the beginning the phase separation is diffusive, and the length scale L grows as $L \sim t^{1/3}$. At later stage when interfaces are well developed, the interfacial tension will induce the hydrodynamic flow, and that will speed up the coarsening process, and the

growth law approaches $L \sim t$, just as pointed out by Siggia. However, it should be pointed out that the agreements are only qualitative, there are large discrepancies in the estimation of the constant A between the theories and experiments.

In the simple binary fluid systems, the linear regime in early stage as predicted by Cahn has not been observed experimentally. Only in the polymer blends do we have convincing evidence of the existence of this linear regime, where the structure function grows exponentially with time [Bates and Wiltzius, 1989; Hashimoto, 1988;]. Evidently the high viscosity of the polymeric systems slows down the dynamics of phase separation significantly, which makes it feasible to study the early stage of phase separation.

A more difficult comparison between experiments and theories is in peak intensity behavior and the structure function $S(k,t)$. Apart from linear Cahn theory, there are no satisfactory calculations up to now which can be used to fit the experimental results, especially at the later stage. However, most of the experimental results were tested to see if they satisfy the dynamic scaling hypothesis (eq. (1.42)). (see § 1.4.4).

Define a normalized structure function $\widetilde{S}(k,t)$ in terms of the scattering intensity as

$$\widetilde{S}(k,t) = \frac{I(k,t)}{\displaystyle\int_{k_a}^{k_b} dk\, k^2 I(k,t)}$$

The range of integration covers most of the ring area, where the peak in $I(k,t)$ is centered. The $\widetilde{S}(k,t)$ defined in such way was shown to follow roughly the scaling hypothesis (eq. (1.42)), especially at the later stage when $\tau \geq 10$, with the scaling

function $F(q/q_m(t))$ exhibiting no time dependence. But generally the function form $F(x)$ is believed not to be universal, it shows some dependence on the concentrations of the samples, and even on the quench depth. Later experiments [Hashimoto et al., 1986a; 1986b; Izumitani et al., 1990; Takenaka et al., 1990] on polymer blends exhibit similar behaviors.

From the scaling hypothesis (eq. (1.42)), the peak intensity

$$I(k_m,t) \sim \widetilde{S}(k_m,t) = k_m^{-d} F(1)$$

where d=3 for bulk samples. At later stage, $k_m \sim \tau^{-1}$ for critical mixtures, and therefore $I(k_m,\tau) \sim \tau^3$. This power law was confirmed in experimentally.

The exponential growth predicted in Cahn's theory was not observed, the LBM theory and extensions due to Kawasaki and Ohta, who included hydrodynamic interaction, have some qualitative features similar to the experimental observation, but did not fit the data properly. In general, it can be said that those results are consistent with the theoretical results although there might still be intricacies that need to be clarified.

1.6 Wetting Phenomena and Phase Separation

Wetting is a phenomenon associated with the interfaces between different phases of matter, of which the most familiar is the contact angle, *e.g.*, a sessile liquid drop on a solid substrate (see Fig 1.7). At equilibrium the contact angle θ is determined by the surface tensions σ of different phases through the Young equation:

$$cos \; \theta \; = \frac{\sigma_{VS} - \sigma_{LS}}{\sigma_{LV}}.$$ (1.46)

where the subscript V, L, S stand for the three phases, vapor, liquid and solid (substrate) respectively.
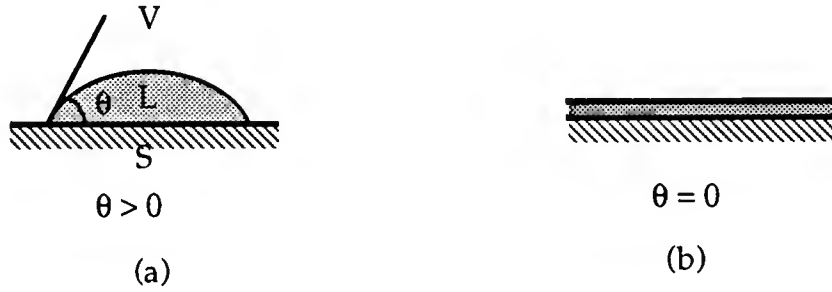

Fig. 1.7. Partial and complete wetting: (a) Partial wetting, the contact angle θ is finite, the liquid phase form isolated droplets on solid substrate;
(b) Complete wetting, angle $\theta = 0$. the liquid phase form a continuous layer of film on the substrate, separating the vapor and the substrate.

The similar phenomena can be observed in binary fluids when they are fully phase separated. Now instead of the vapor and the liquid phase, we have two liquid phases α and β, in contact with a solid substrate, which is usually the container wall. The Young equation still applies, and the contact angle θ can be measured at the edge of the meniscus as shown in Fig. 1.8.

From the Young equation, we can see that

$$\left| \sigma_{\alpha s} - \sigma_{\beta s} \right| < \sigma_{\alpha \beta} ,$$ (1.47)

for any finite contact angle θ, where the subscript s stands for the substrate or solid phase. This case is usually called the partial wetting. If the equality holds, i. e.,

$$\left|\sigma_{\alpha s} - \sigma_{\beta s}\right| = \sigma_{\alpha\beta}, \qquad (1.48)$$

then the contact angle must be zero. In this case, it is more energetically favorable to have the two phases with the highest surface tension physically separated by a layer of the third phase, as shown in Fig. 1.8b. This case is known as complete wetting. To be more concrete, we assume $\sigma_{\alpha s} > \sigma_{\beta s}$, then the β phase will be sandwiched between the α phase and the substrate, and we will say that the β phase wets the substrate.
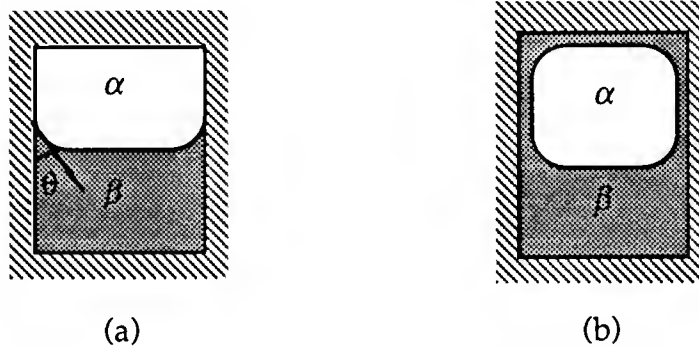

(a)   (b)

Fig. 1.8 Wetting in binary fluids with the container wall; (a) Partial wetting in fully phase separated binary fluids, the finite contact angle θ can be measure at the edge of the meniscus; (b) Complete wetting: a layer of phase β completely covers the substrate, insulating phase α from it.

The interests in wetting phenomena increased significantly after Cahn [Cahn, 1977] pointed out that there is always a phase transition from partial to complete wetting upon the approach to a critical point. His argument was simple and intuitive, based on the thermodynamics of the phase transition. Upon approach to the critical point inside the two-phase region, the interfacial tension $\sigma_{\alpha\beta}$ vanishes as the inverse square of the bulk correlation length ξ, *i.e.*,

$$\sigma_{\alpha\beta} \sim \xi^{-2} \sim t^{2\nu} \ ,$$
(1.49)

with $\nu = 0.63$ is a universal exponent, and the t is the reduced temperature. On the other hand the difference in surface tension $\sigma_{\alpha s} - \sigma_{\beta s}$ should vanish as the order parameter close to the substrate (in the case of vapor and liquid, the density difference between the two phases), i. e., it goes to zero as t^{β_1}, with $\beta_1 = 0.8$. Then according to Young's equation (1.46), the contact angle

$$cos \ \theta \sim t^{\beta_1 - 2\nu} \sim t^{-0.5},$$
(1.50)

thus it will reach unity as the critical point is approached. That point marks the transition from partial to complete wetting, and it is known as the wetting temperature T_w. In the case of binary fluids, in the two phase regions of the phase diagram, there is a temperature T_w that marks the boundary.

In the last decade we have seen remarkable advances in our understanding about the wetting phenomena, especially on the wetting transition. Most of the effects have been concentrated on the equilibrium properties. But gradually the dynamic aspect of the wetting effect started to catch certain attentions among physicists, especially in the topics of liquid or polymer spreading [Chen and Wada, 1989; Heslot et al., 1989]or dewetting

[Redon et al., 1991] on solid substrates . The study of the effect of wetting on the dynamics of phase separation started relatively recently. Because usually T_w is at least several degrees Celsius away from the critical point, the final state in the quench experiments will be within the complete wetting regime. As a result, there is a complete wetting layer of the preferentially adsorbed phase next to the solid substrate (usually the container wall). It is of great interest to understand the growth of this wetting layer. Early on it was pointed out theoretically [Lipowsky and Huse 1986] that the thickness $l(t)$ of the wetting layer will grow as a power law at the late stage of the phase separation if it is diffusion limited, i.e.,

$$l(t) \sim t^b,$$

(1.51)

where b is equal to 1/8 and 1/10 respectively for nonretarded and retarded van der Waals force. It is much slower than the coarsening process, e.g., Lifshitz - Slyozov theory, largely because after the initial wetting layer formed on the substrate, it leaves a depletion zone right next to the wetting layer. Any further growth of the wetting layer will have to diffuse through this zone, which act like an energy barrier in slowing down the process. The type of slow growth law was confirmed in some computer simulations, even though it hasn't been observed experimentally in binary fluid systems.

More recently Guenoun, Beysens and Robert [Guenoun et al., 1990] undertook optical microscopy study on the morphology and domain growth in a binary fluid mixture undergoing spinodal decomposition near the container wall. Besides observing the morphology changes due to the wetting effect, they found the wetting layer thickness l grows with time roughly like $t^{1/2}$. But that result should be taken with certain caution, as it is well known that the kinetic exponent extracted from microscopic observation is unreliable. (see, e. g., Chou,

1979). More recently, light scattering was used by Wiltzius and Cumming [Wiltzius and Cumming, 1991] on a quenched binary polymer mixture, there they discovered a new "fast" mode where the length scale L grows as $t^{3/2}$ with time. This fast mode was attributed to the wetting effect of the container wall on the fluids. But up to the moment we have still no theoretical understanding that can explain the nature of this fast growth process.

Our work had been motivated by that of Wiltzius and Cumming. First of all, we sought to establish the generality of the fast mode by studying a simple low-molecular-weight binary system, guaiacol-glycerol-water (GGW), and we gave a detailed characterization of the fast mode and its relations to the other physical quantities of the system. From there, we hoped to gain a deeper understanding of the phenomena which might shed light on certain aspects of phase separation processes, especially on the role of wetting. Also through these experiments, we hoped to provide interested theorists enough experimental input and incentive to develop a comprehensive theoretical model.

CHAPTER 2

LIGHT SCATTERING METHOD: CONCEPTS

Light scattering has been widely used nowadays in almost every discipline of natural science, particularly in physics and chemistry, where it has become one of the basic tools in studying the structures and the dynamics of many systems. Over the past century, light scattering method had enjoyed a steady development starting with the classical work of Lord Rayleigh and others. The advent of lasers as a primary light source brought a revolution to this field, during which the dynamic light scattering method was invented and widely applied to a whole range of systems. Nowadays laser light scattering, along with X-ray and neutron scattering, are the standard tools for studying the structures of various materials in science and engineering. As light scattering is the most convenient and inexpensive among the scattering methods, it is more widely available and used. Over the years, there have been excellent reviews and books published on the subject of light scattering [Berne & Pecora 1976; Chu, 1974; Chu, 1991; Kerker, 1969; van der Hulst, 1957], where its principles have been well elucidated and its applications to a varieties of physical and chemical systems outlined. Therefore, here in this chapter I will limit myself to a brief review the basic concepts and some of the common notations involving light scattering. Furthermore, in relevance to our experiments we will confine our discussion here largely to elastic light scattering.
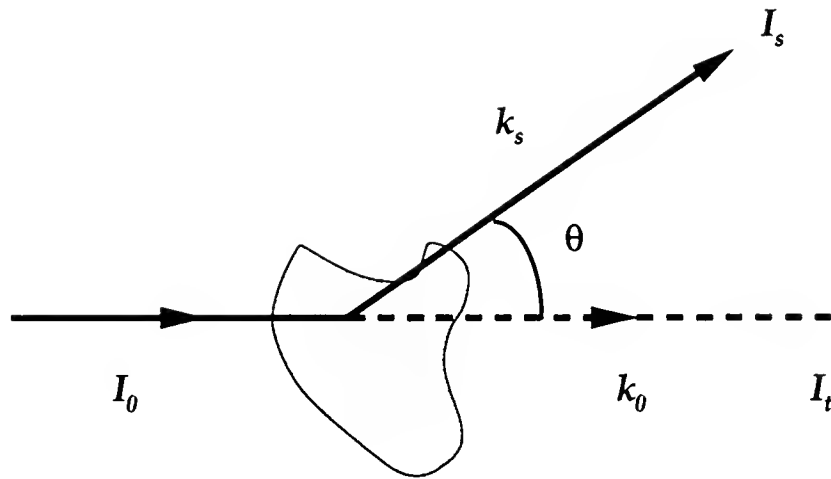
Fig. 2.1. Scattering geometry. I_0, I_s, and I_t are incident, scattered and transmitted light intensity respectively, θ is the scattering angle. k_0 and k_s are respectively the incident and scattered wave vectors, whose magnitudes are $2\pi/\lambda_s$, where $\lambda_s = \lambda_0/n$, with λ_0 and n being the wavelength *in vacuo* and the refractive index of the scattering medium.

Fig. 2.1 shows the typical light-scattering geometry, where the incident light beam impinges on the scattering medium (shaded area). Most of the light will transmit through the medium without any scattering, which is the transmitted light with intensity I_t, and a small portion of light is scattered that has the intensity I_s at angle θ. In this geometry we have ignored variations with respect to the azimuthal angle, which is appropriate for systems which are isotropic, like most liquids. Experimentally we can measure not only the intensities and the direction (the scattering angle), but also the frequency (energy) changes of the scattered photons, as there can be energy exchange between the scattered photon and the scattering medium. Whereas the scattered intensity can be related to the structures of particles or

inhomogeneities in the medium, the optical spectra reveal the dynamical motions. In the experiments we are concerned with here, we are interested mostly in the structures of domains and their growth, therefore experimentally we only measure the scattered light intensity I_s and its profile, i. e., its variation over the scattering angle θ. This is known as elastic light scattering, where we are not concerned with the change of energy of the scattered photons, only their numbers (intensity). Equivalently we assume that the photon energy (frequency) isn't changed from the scattering, or the photon scatters elastically. In contrast, those light scattering experiments which also probe the energy (frequency) change of the photons are generally called dynamic light scattering. I will limit the discussion here only to elastic scattering.

We want to measure the variation of the scattered light $I_s(\theta, t)$. Conventionally the more relevant quantity is the momentum transfer $\mathbf{q}$ which is defined as

$$\mathbf{q} = \mathbf{k}_s - \mathbf{k}_0,$$ (2.1)

where and $\mathbf{k}_s$ are $\mathbf{k}_0$ are the wave vectors of the scattered and the incident photon, respectively, as shown in Fig. 2.1. Because the magnitudes of $\mathbf{k}_s$ and $\mathbf{k}_0$ are the same, and equal to $2\pi/\lambda_s$, the magnitude of $\mathbf{q}$ is simply

$$q = \frac{4\pi}{\lambda_s} sin(\frac{\theta}{2}) = \frac{4\pi n}{\lambda_o} sin(\frac{\theta}{2})$$ (2.2).

Therefore, q is a function of the scattering angle θ, but it has the dimensional of inverse length. In isotropic medium, the scattered intensity I_s only depends on the magnitudes of $\mathbf{q}$, i. e., q.

The structures and dynamics of a system are characterized by its structure factor. The dynamic structure factor $S(q,\omega)$ is defined as the Fourier transform of the time-dependent correlation function $G(r, t)$, which is

$$G(r, t) \equiv \left\langle \delta\varphi(r, t)\, \delta\varphi(0, 0) \right\rangle \qquad (2.3)$$

where $\varphi(r, t)$ is the local order parameter, and for binary fluids, φ is the local concentration C of one of the molecular species. The angular brackets denotes an equilibrium ensemble average, and

$$\delta\varphi(r, t) \equiv \varphi(r, t) - \langle\varphi\rangle \qquad (2.4)$$

is the local deviation or fluctuation of the order parameter from the equilibrium value. Then $S(q,\omega)$ is defined through $G(r, t)$ as

$$S(q,\omega) \equiv \int dr \int_{-\infty}^{\infty} dt\, G(r, t)\, e^{-i(q\cdot r - \omega t)}. \qquad (2.5)$$

In concert with $S(q,\omega)$, the static structure factor is defined as

$$S_0(q) \equiv \int \frac{d\omega}{2\pi} S(q,\omega). \qquad (2.6)$$

What makes the scattering methods so important in determining the structures and dynamics experimentally is the following relation: the frequency-resolved scattering intensity $I_s(q,\omega)$ is proportional to $S(q,\omega)$ if multiple scattering can be ignored, and in the absence of frequency-resolution, the scattering intensity $I_s(q)$ is proportional to the static structure factor $S_0(q)$.

This relation is the basis for understanding and interpreting any experimental data. Here I will not bother with its derivation from first principles, as it has been dealt with in most books on scattering, (Stanley [Stanley, 1971] gives a simple and neat derivation), but rather try to emphasize certain important points associated with it.

The above relation is strictly true in the single scattering limit, namely when multiple scattering is negligible. An incident photon scatters only once at most inside the scattering medium before exiting [see, e.g., van der Hulst, 1957]. Multiple scattering poses a problem too complicated to deal with mathematically, although theories have existed to treat double scattering analytically, but even that isn't straightforward. Therefore light scattering experiments are usually conducted in the single scattering limit, where multiple scattering probability is small. The contribution from multiple scattering can be monitored qualitatively by measuring the beam attenuation or the turbidity τ of the scattering medium, which is defined through

$$\frac{I_t}{I_0} = e^{-\tau d},$$
(2.7)

where d is the path length through the scattering medium. In the single scattering limit, the turbidity is small.

In studying the kinetics of phase separation in binary fluids, keeping at low turbidity limits the quench depth ΔT, which indicates how deep the system can be quenched into its 2 - phase regime (see Fig. 1.1). Deep quench will turn the fluid too turbid to be in the single scattering limit. Turbidity could also be a problem at late stage of phase separation process.

To study the kinetics of the phase separation process, we measure the scattered light profile $I_s(q)$ at different times following a quench into the 2-phase region of the phase diagram, and thus observe its evolution with time. From each scattering profile at specific time, we can extract a length scale L that is indicative of the average size of the domains growing in the fluids, and thence the growth law of L.

CHAPTER 3

APPARATUS

We have been using time-resolved light scattering to study the kinetics of phase separation in GGW mixtures. The experimental setup of our light scattering apparatus resembled that described in Cumming et al. [Cumming et al., 1992]. We started by choosing a CCD (charge-coupled device) camera as the detector for measuring the intensity of the scattered light. Compared to other light detectors, e.g., photomultiplier, etc., CCD cameras offer distinctive advantages for our purpose. The main component of the camera, the imaging area, is a silicon chip with a 2-d array of imaging elememts called pixels. An off-axis paraboloidal mirror and optical components were used to focus and adjust the light beam onto the CCD chip, which has an imaging area about 2 cm * 2 cm. The apparatus was noted for its simplicity in design and relatively small number of components. Here I will first present the setup of our light scattering apparatus, and then discuss its major components in detail, where its design will be emphasized. Afterwards I will describe the temperature control system, that enabled us to change the temperature quickly, whereas still have a good temperature stability. These two systems constituted the essential elements for our experiments.

3.1 Light Scattering Apparatus

The initial setup of our light scattering apparatus was very similar to that used by Cumming et al. [Cumming et al., 1992]. A schematic plan view diagram of the apparatus is shown in Fig. 3.1, where all the components shown are on a horizontal plane. Of these components listed, the two plano-convex lenses (condenser#1: Product No. 01LPX311, focal length f = 330 mm, diameter 145 mm; condenser#2: Product No. 01LPX127, focal length f = 60 mm, diameter 42 mm) and the paraboloidal mirror (Product No. 02-POA-019, diameter 95 mm, off-axis distance 83.6 mm) were purchased from Melles Griot, and the other optical components, including the 5-axis lens positioner (model 740) on which the paraboloidal mirror is mounted, were purchased from Newport. Our light source was a 5mW power HeNe laser from Jodon Inc. (model # HN-5HFP). Non-essential components (not shown in Fig. 3.1) included two XYZ translation stages (model # 460-XYZ) on which the two lenses were mounted, and a dual-axis translation stage (model # 405) on which the CCD camera head rested. These components enabled us to finely tune the positions of the lenses and the camera within the precision of 1 micron in order to achieve the full resolution of our apparatus. Other non-essential components used in the apparatus were several types of rod/clamp assemblies (model # 305, 340,345, 370) that anchored optical elements onto the optical table, and a beam steering instrument (model # 670) which adjusted the laser beam direction. All of the above listed non-essential elements were purchased from Newport.

As I have mentioned above, we chose a CCD camera as the light detector that measures the scattered light from a phase separating fluids. The main component of the camera is a CCD chip, which is one of the silicon

array imaging devices developed since the late 60s. A CCD chip consists of a

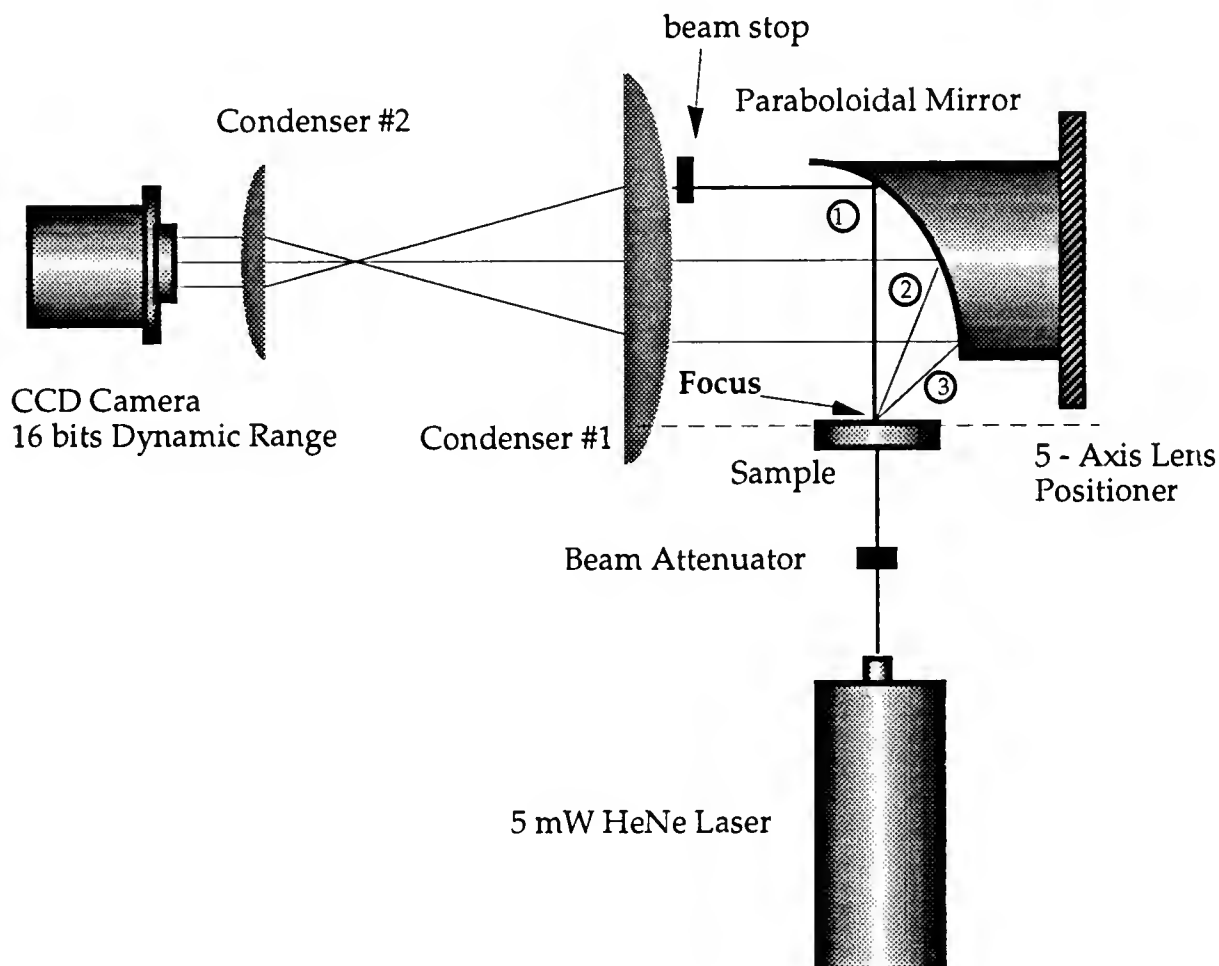2-dimensional array of imaging elements called pixels. A pixel on a CCD chip

Fig. 3.1 Top view of the elastic light scattering apparatus. All major components are listed. The light from a 5 mW laser impinges on the sample via an attenuator. The sample is positioned at the focus of an off-axis paraboloidal mirror capable of collecting light scattered up to 50° away from incidence. The dashed line indicates the axis of the paraboloidal mirror. Light ray (1) indicates the transmitted beam, while 2 and 3 the scattered rays. The scattered light ray column is reduced to appropriate size by a pair of confocal condenser lenses before sending onto a CCD camera.

is essentially a quantum well. As photons strike the silicon chip and they create electron-hole pairs, the holes leak away and the electrons are trapped in the well. Therefore the number of electrons accumulated in the well is proportional to the number of photons that had struck the pixel, and thus measuring the intensity of light is a matter of counting the number of electrons in the well, that is done by a set of registers inside the camera. Our camera was purchased commercially as a package from Photometrics. The whole package consisted of a camera head (model No. CH250), where the CCD chip was mounted, an electronic control unit (model No. CE 200A) and liquid cooling unit (model No. LC200). It came also with a interface board so that the camera could be operated from a Macintosh II fx computer. The CCD chip in the camera was a Thomson CSF chip of size 1024 × 1024 pixels. Each pixel had dimension of 19 μm by 19 μm.

For our purpose, CCD chips offer great advantages over other detectors. First of all, because it consists of a 2-dimensional lattice of pixels, it can measure the whole scattered light profile in a single exposure, thus eliminating the complications associated with having to take the measurements sequentially. This feature was particularly suitable for studying the early stages of the phase separation. With a CCD camera as the detector, the measurement of the scattered light profile only takes as little as a fraction of a second. Another advantage of CCD chip is its high sensitivity, which is determined by two factors: the quantum efficiency (Q.E.) and the noise level. Q. E. is the probability of a incoming photon being detected by a device or detector, for a CCD chip it can reach up to 80%, which is an order of magnitude higher than the sensitivity of photographic films. For the CCD chip used in the present experiments, its Q. E. was at about 40% at the wavelength of the NeHe laser, which is 632.8 nm. With regard to noise, the

CCD camera head used in the present experiments was Peltier cooled to about -40 °C, at that temperature the noise level was significantly reduced compared to that at room temperature. Other benefits of a high quality CCD camera include the wide dynamic range and extremely good linearity. Dynamic range is defined as the ratio of the device saturation charge to the system noise level, expressed in electrons. Our camera had 16 bits of dynamic range. Linearity is the strict proportionality of the number of electrons accumulated to the intensity of light, and in our camera, the deviation from the linearity within the saturation limit was below 0.1%.

The setup of the rest of the optical components was designed to collect the scattered light and reduce it to appropriate size before sending onto the CCD camera. For the former, we used an off-axis paraboloidal mirror whose reflective surface was an inside section of a spherical paraboloid, the curved surface swept by a parabola undergoing a full revolution around its axis. We positioned the mirror in relation to the sample cell so that the spot where the laser beam impinged on the sample cell was also the focal point of the paraboloidal mirror. In the scattering plane as shown in Fig. 3.1, the transmitted laser beam was the *lactus rectum* of the parabola (shown in Fig. 3.1 as light ray #1), and the revolution axis of the parabola intersected the transmitted beam perpendicularly right at the spot where the beam impinged onto the sample cell. Here the scattering volume was the volume of the GGW mixture in the sample cell that directly illuminated by the incident laser beam, whose beam spot was about 2 to 3 mm in diameter, and our sample cell thickness was 0.8 mm, therefore the volume was of about 4 to 7 mm^3. In this configuration, the scattered light rays emanated from the scattering volume in the sample cell and then reflected from the mirror, they became a parallel ray bundle (see Fig. 3.1). In this way, the mirror served to

columnate the scattered light rays, whereupon they could be passed through a pair of convex lenses which share a focus, and then onto the CCD camera. The pair of confocal lenses are used to reduce the cross section of the parallel rays to the size of the CCD chip, so all of the light rays collected by the mirror would land on the CCD camera.

The paraboloidal mirror collects the light scattered up to 50°, which corresponds to photon momentum transfer magnitude up to 86,000 cm^{-1} or 8. 600 μm^{-1}. To achieve the full resolution of the CCD chip, we required that all light rays emanating from the scattering volume in a given direction or a given momentum transfer q be directed to a single pixel on the chip, *i.e.*, all the parallel rays from the scattering volume must map onto a single pixel. This was the real technical challenge of this apparatus for achieving the best resolution. For adjustment and fine tuning, we first aligned the mirror and the condensers on an optical axis by a laser beam. Each of the lenses was mounted on an XYZ stage (from Newport), and it enabled us to fine tune the positions of these optical components. Naturally, the CCD camera had to be adjusted along the optical axis to yield the best resolution. The most important adjustment was the 5-axis lens positioner on which the paraboloidal mirror was mounted. Its fine tuning was done in combination with the calibration of the CCD chip.

The calibration of the apparatus consisted of finding the mapping from momentum transfer q to pixel positions on the CCD chip. For that purpose we put a grating in the position of the sample cell. The interference pattern by a laser beam is well known. Because of the high coherence of laser light, we were able to trace every order of interference maxima from the image taken by the CCD camera. In order to fully calibrate every pixel on the CCD chip, we built a rotor with a low speed motor (60 revolutions per minute) to

rotate the grating in the plane perpendicular to the incident laser beam. For every revolution, the interference maxima swept through 360° and traced a set of coaxial light cones, which can be imaged on the CCD by making an exposure of appropriate duration, in our case that is half of the period of the rotation, about 0.5 second. From the image taken by the CCD camera, we could find the exact pixel location for each order of the interference maxima, which also satisfy the positive interference condition (see, e. g., Hecht, 1987)

$$d \sin \theta_m = m \lambda \ , \tag{3.1}$$

with $m = 0, \pm 1, \pm 2, \pm 3, \ldots$, where d is the grating spacing, and angle θ is the scattering angle, and λ is the wavelength of the incoming light, i. e., 632.8 nm in our case. Thus we could calculate the momentum transfer q for each maximum because q is a function of scattering angle θ. In this way, we calibrated all the pixels that the interference maxima had swept through on the CCD chip. From these maxima, we found a fitting equation from their pixel positions to the corresponding q's. The q of these pixels in between two neighboring maxima could be calculated from this fitting equation. The CCD image of the rotating grating also provided a good assessment about the alignment of the paraboloidal mirror, and allowed further fine tuning to reach the best resolution possible. We have used several gratings of different spacing ranging from 100 lines/mm to 20 lines/mm for the calibration, the resultant calibration maps differed by less than 0.02 μm^{-1} in the q values, which was less than a pixel on the CCD. Fig. 3.2 shows a calibration curve from the grating images.

The setup of the light scattering apparatus was modified slightly from the initial design (Fig. 3.1) after a period of preliminary experimentations. A

schematic diagram of the final setup is shown in Fig. 3.3. The main reason for the modification was to change the orientation of the sample cell from vertical as in Fig 3.1 to horizontal as shown in Fig. 3.3, in order to minimizing the gravitational effect on the process of phase separation and annealing, which turned out to be of particular importance on the fast mode.
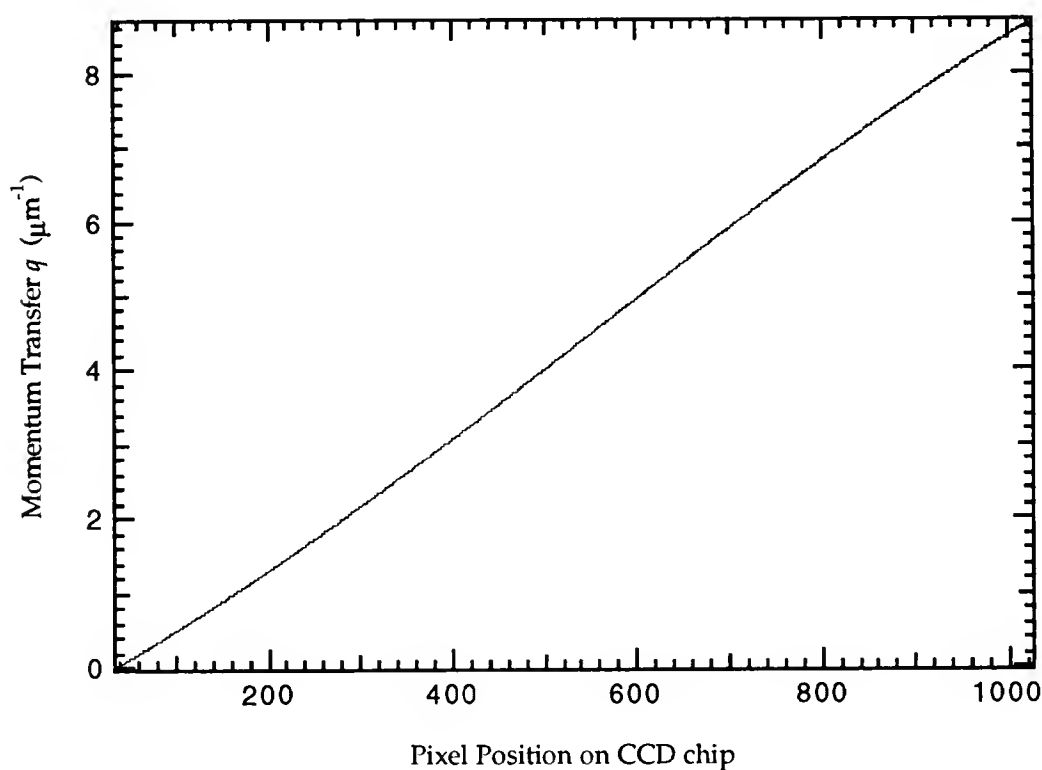

Fig. 3.2 Calibration curve for the CCD chip. It maps each pixel in a row on the CCD chip onto its corresponding q value. It was made form a 20 line per mm grating.

Our sample cells shape like a disk, and the fluids are confined between two disk windows about 1 inch in diameter and usually about 0.8 mm thick (see the next chapter for details of the sample cell geometry.). The thickness could be changed if necessary. The GGW mixture used in this study has a density mismatch about 10% in their pure forms, which is relatively large among the fluid mixtures extensively used for the similar studies (L-W, I-W, *etc.*). In the initial orientation, the large density mismatch could induce sedimentation and convection of the heavier phase sinks to the bottom and lighter phase rises to the top, which causes macroscopic phase separation. That eventually
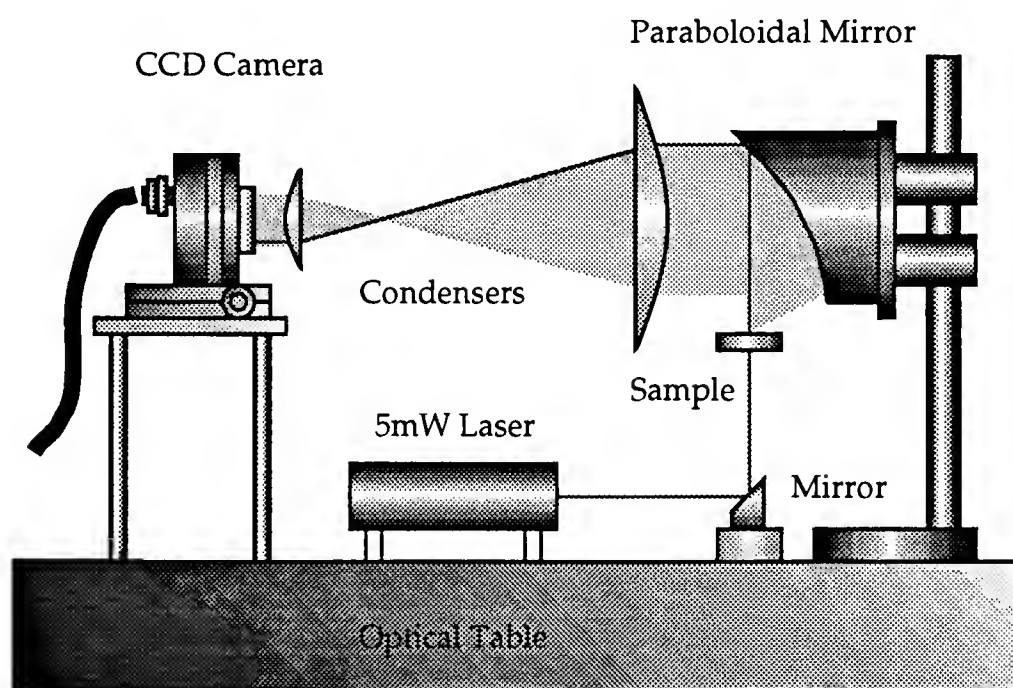
Fig. 3.3   Side view of the final setup of the elastic light scattering apparatus. The major change was the orientation of the sample cell, and correspondingly other optical components had to be readjusted for the purpose. But the same components were used as the initial set up (Fig. 3.1), and the design principle and concepts were kept the same.

creates concentration gradient in the sample cell along the vertical direction. A change of the orientation eliminated most of these problems. The details of the gravitational effects will be discussed in chapter 5.

The final setup (Fig. 3.3) used most of the original components, the major optical components were the same, so was the design principle. The alignments and calibration procedure are almost exactly the same as described above.

The whole light scattering apparatus was mounted on a Newport optical table (model No. RS-48-12) equipped with pneumatic vibration isolation legs (model No. XL4A-23.5).

3.2 Temperature Regulation and Quench System

To study the dynamics of the phase transition, we needed a temperature regulation system which could quench the temperature from one point to another and then stabilize at that temperature quickly. This requirement is especially stringent for binary fluids, whose interdiffusion constant D is normally several orders of magnitude larger than that of other systems frequently used in the studies, like alloys and glasses. Because of this, it was initially believed that it was not experimentally feasible to study spinodal decomposition in these liquid mixtures, as the time scales are typically very small due to the large diffusion constant. However, this difficulty could be circumvented by making measurements very close the critical point, where D vanishes as

$$D = \frac{k_B T_c}{6\pi \eta^* \xi},$$
(3.2)

where η^* is the high frequency kinematic viscosity, and ξ is the correlation length, which diverges at critical point T_c according to eq. (1.1a).

Further restrictions on the quench depth $\Delta T = |T_f - T_c|$ (see Fig. 1.1) come from the light scattering experiments. Only in the single scattering limit, the scattered light intensity profile $I(q, t)$ is strictly proportional to the structure function $S(q, t)$, whose physical meaning is well understood. Beyond this limit, the multiple scattering sets in and can render the experimental data hard to interpret. Therefore, we had to require the quench depth to be shallow enough that most of experimental data are within the single scattering limit.

The restrictions posed above limits the quench depth ΔT to be fairly small. For usual binary systems, e. g., 2, 6 lutidine - water (L-W), ΔT is limited to be below 10 mK. For our system of GGW, which has a much higher viscosity comparing to that of L-W, the single scattering limit will be met if the quench depth is below 100 mK or 0.1 K.

In relation to this quench depth, we needed to have a temperature control system that had a temperature stability at least one order of magnitude lower, that is, 10 mK. We set out to design a simple control system that met this requirement, and also could quench relatively quickly. These two goals were often in conflict, as stability meant resistance to changes or fluctuations, and we had to strike a balance between the two factors.

We built two separate circulation circuits with independent circulation pumps and thermal regulation circuitry set up at two temperatures. One was at anneal temperature T_i (initial temperature), which was about 0.1 °C away from the critical temperature T_c but on the one phase side, and the other was set at quench temperature T_f (final temperature). For the GGW mixture close

to the LCST, it happens that $T_i < T_c$ and $T_f > T_c$. Water was used as the temperature regulation medium. A schematic diagram of the circuit is shown in Fig. 3.4. Each circuit had a heat exchanger made of copper tubing that submerged in a Neslab RTE 210 refrigerated bath/circulator, which had a stability better than 0.1 °C. Within the circuit loop, the temperature was further regulated by a Lakeshore DRC 93C temperature controller through a resistive heater, which was made from a resistive wire wrapped around a segment of copper tubing of diameter 7/8 inch and about 10 inches in length, and then sealed with a thermally conducting epoxy. Each circulation circuit also included a Millipore filter of mesh size 0.22 μm to rid air bubbles and dirt from the circulation water, and the water circulation was sustained by a Little Giant pump (model#: 3-MD) with 9 gallon per minute pumping power. This two stage temperature control system achieved temperature stability of ±2.5 mK or better over the duration of most of our experiments, which could last from several minutes to hours. Fig. 3.5 shows a typical temperature readings during a period about one hour and a histogram of the data, where the distribution of the temperature fluctuation fits well with a gaussian, from the fit we had got the average to be 29829.4 Ohms with standard deviation of 0.9 Ohm, with corresponds to 0.7 mK in temperature. The temperature was monitored through a YSI thermistor, which had a nominal resistance of 30,000 Ohms at 25 °C.

A pair of four-way ball valves (Whitey 4-way crossover valves, material: stainless steel, Cat. # 45YF8) were used to switch the water flow tothe sample cell from one circuit to another, thus making the sudden quench of temperature from T_i to T_f. They were interconnected in such a way that one circuit flow pass through the sample cell, while the other circuit flow was shunted. The roles of the two water flow circuits could be reversed by a
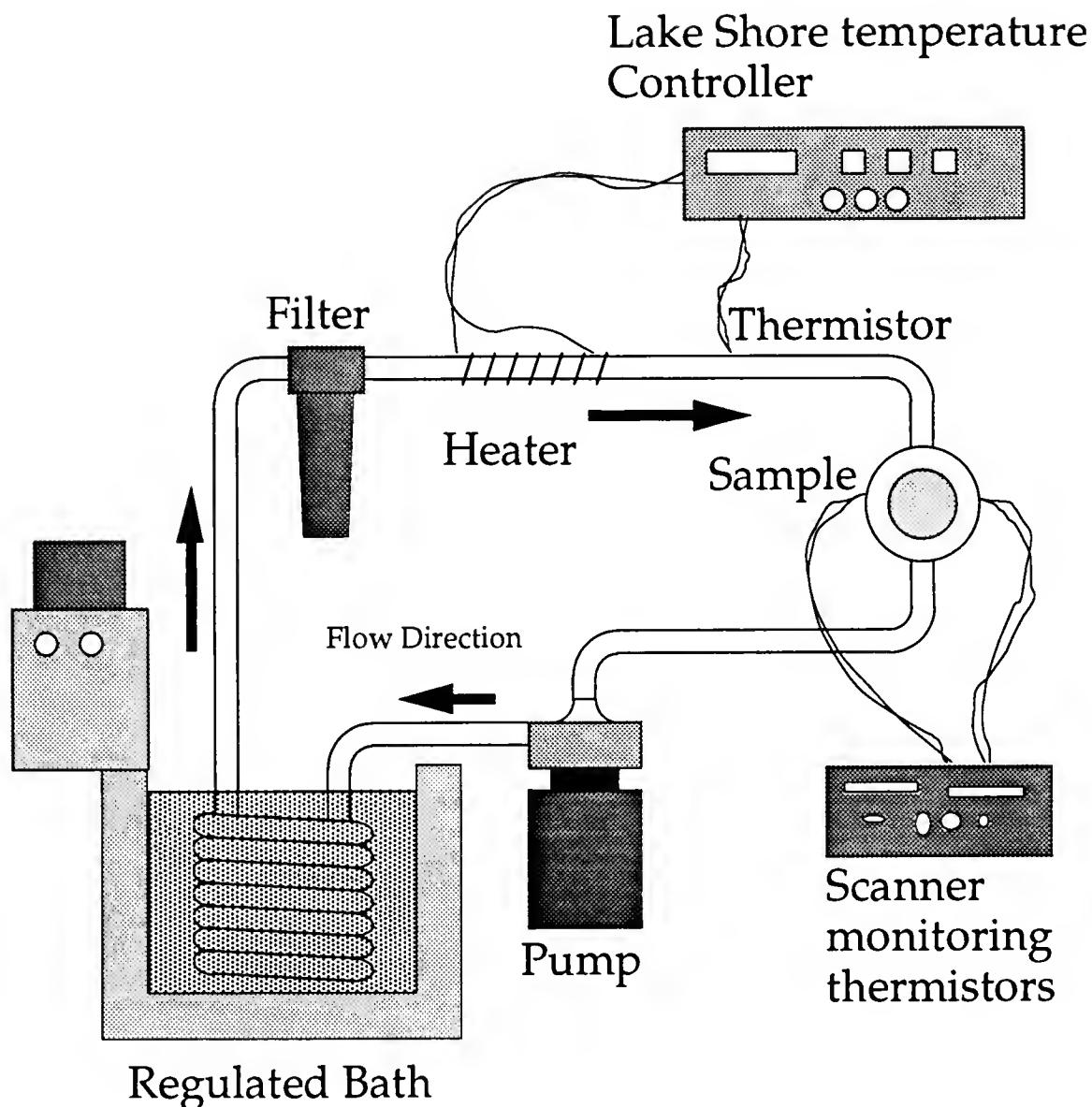
Lake Shore temperature
Controller

Filter

Thermistor

Heater

Sample

Flow Direction

Scanner
monitoring
thermistors

Pump

Regulated Bath

Fig. 3.4 One half of the temperature regulation system . It is a closed water circulation system, and the temperature was controlled through the heat exchange with the regulated bath, and a wire heater that was regulated by a Lakeshore temperature controller. A water filter with small pore size ridded the dirt and air bubble of the circulating water. Similar circuits were used to regulate and pump water at each of T_i and T_f, but for clarity, only one side is shown.
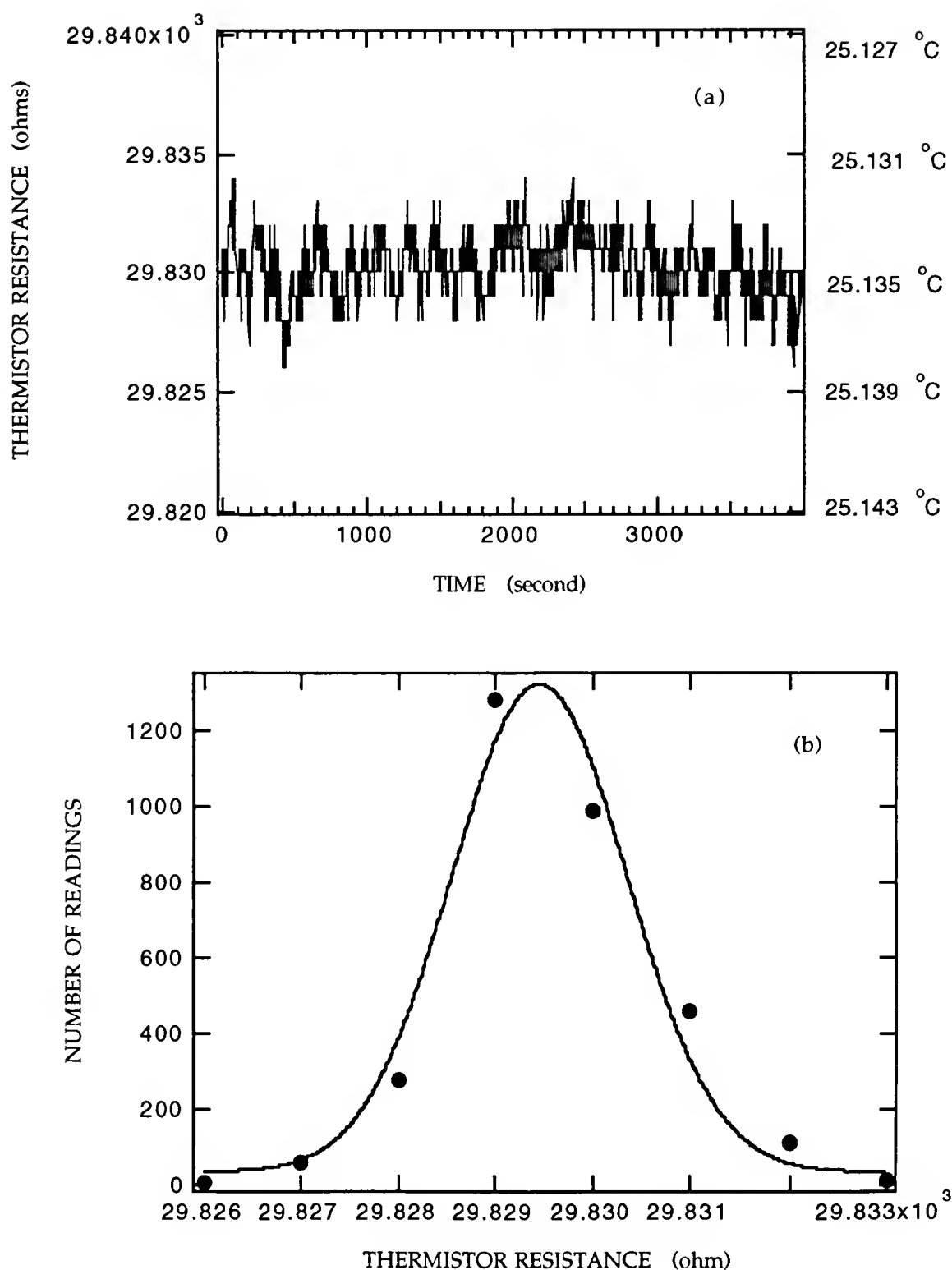
Fig. 3.5 Temperature stability over a period of a hour. (a): Temperature readings over that period; (b): historgram of the data in (a), with a gaussian fit.
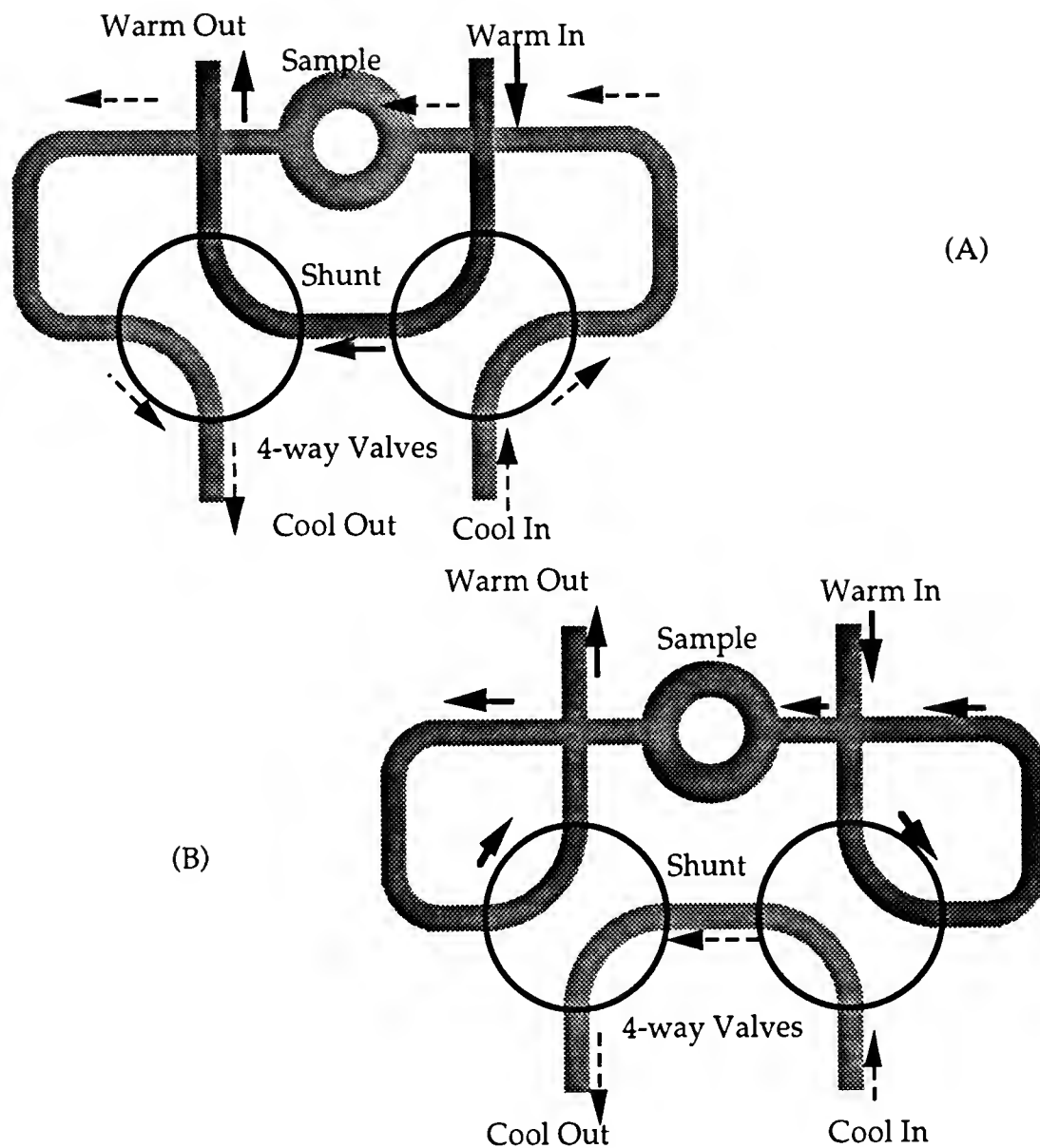
Fig. 3.6 Two configurations of a pair of 4-way valves which rerouted circulation waters to the sample cell. The solid arrow ➡ indicates flow of hot water while the dashed arrow ╍➤ the flow of cooling water. (A) Annealing configuration, cool water flows through the sample while hot water is shunted. (B) Quench configuration, hot water flowing through the sample cell.
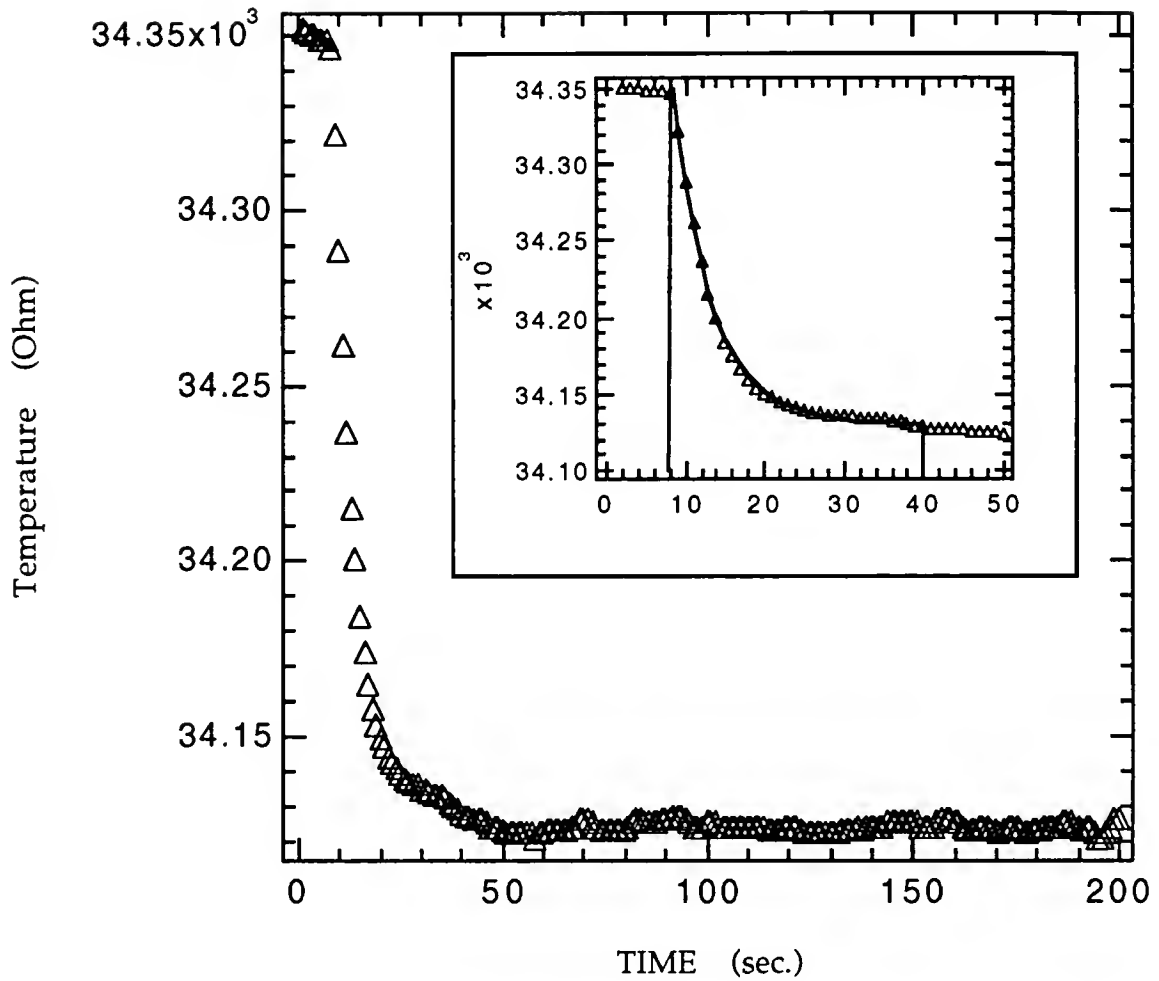
Fig. 3.7 Temperature profile of a quench with time. The insert window is the blowup of the profile first 50 seconds, when an equilibrium was reached. That part of temperature readings can be fitted with an exponential function with time constant about 5 seconds.

simple switching of the valves. A schematic presentation of the flow directions in two configurations is shown in Fig. 3.6, where the temperature of the cool water is T_i , and hot water T_f, and the two circles present the two 4-

way valves. The scheme allows for a minimal exchange volume between the two flow circuits while keeping the majority of the plumbing with constant temperature flow. After the switching the valves, the temperature increased exponentially, with the time constant about 3 ~ 5 sec., upon approach to final temperature T_f. A typical quench profile is shown in Fig. 3.7, the time constant for the quench was 5 seconds. It effectively reached the final temperature within 40 seconds after the quench.

CHAPTER 4

EXPERIMENTAL PROCEDURES

The binary fluid system we have chosen for the kinetics study of was guaiacol-glycerol-water (GGW), as mentioned earlier in Chapter 1 where we discussed its phase diagram. Strictly speaking, it is a ternary system, but because of the relatively small quantity of water (H_2O) presented and the physical and chemical properties of the three components, we argued (see § 1.1) that the mixture was quasi-binary and almost all of its physical properties (e.g., critical exponents, *etc.*) were binary like. This assumption was confirmed by the experimental studies on critical properties of the system [Johnston, 1983; Johnston et al. 1985].

We chose GGW mainly because of its high viscosity of glycerol, which in its pure form is 1000 times more viscous than the common molecular fluid like water. Wiltzius and Cumming [Wiltzius and Cumming, 1991] observed the fast mode in a polymer mixture, which was highly viscous that its critical dynamics was slowed down drastically in comparison to the binary fluids used extensively for previous phase separation studies, *e.g.* L-W, I-W, *etc.*. Even in the polymer mixture, the fast mode was observed only within a time window of 1000 seconds following the quench. If we rescale this time with viscosity to the simple binary fluid systems like L-W, it will be reduced to the order of seconds, which roughly equals the quench time. Therefore, to

observe the fast mode in a simple binary fluids, we had to search for a system with relatively high viscosity, and GGW fulfilled the requirement. In addition, GGW also provides the convenience of tunable T_c with water content in the mixture, with 5 to 6% of water, T_c happens to be between 20 to 30 °C, which is in the neighborhood of room temperature. There are other binary mixtures involving glycerol, but their critical temperatures are either close to 0 °C or above 80 °C. Therefore, GGW was most suitable experimentally besides being most well studied, and the chemicals were readily available and inexpensive.

4.1 Sample Preparation

The glycerol and guaiacol used were purchased from Aldrich. Glycerol was of spectrophotometric grade, and 99.5+% in purity. Guaiacol was of 98% of purity. Distilled water was purchased from VWR Scientific, and it was a product of EM Industries, Inc.. All three were used without further purification. The glycerol is highly hygroscopic, it will readily absorb moist from the air if left open, and guaiacol is light and air sensitive. Therefore their containers were only opened inside an argon environment (glove box) during the preparation of the mixtures. We used 15 ml vials as the container for the mixture, with Teflon lined caps and parafilm each vial was carefully sealed and then stored in a refrigerator, which provided an environment of relatively stable ambient temperature below the phase separation threshold of the mixture and with minimal exposure to light. If it happened, air and light contamination could be readily detected as the color of the mixture turned increasingly dark over a period of a week or two.

We prepared the GGW mixture in an argon glove box, which had a filter system that recycled the argon gas inside the box constantly and rid the moisture and oxygen from the environment. First we mixed the water with glycerol, the water was never more than 6% of the water-glycerol mixture by mass. Throughout this thesis, we define the water content x of a mixture as

$$\text{water content } x = \frac{\text{Mass of water}}{\text{Mass of water} + \text{Mass of glycerol}} \qquad (4.1)$$

in its glycerol-water mixture. Then the mixture was shaken and agitated, and finally stirred with a magnetic stirrer for at least 3 hours before mixing with guaiacol. After the finally adding guaiacol to the mixture, it was tumbled and stirred at a temperature well below its LCST for at least a day before use.

4.2 Phase Diagram of Guaiacol-Glycerol-Water Mixture

The general features of the phase diagram of GGW have already been discussed in section 1.1, and its general miscibility behavior was explained qualitatively in terms of thermodynamics and peculiar interactions among the molecules. A schematic phase diagram of GGW mixture is shown in Fig. 4.1. The critical behavior the mixture has been investigated by Johnston and coworkers [Johnston et al., 1985], and they found when the mixture had over 5% of water content x (defined by eq.(4.1)), the two critical points, LCST and UCST, were then essentially independent, and each had the same critical exponents as 3-D Ising model (see § 1.1), which is the universal class to which the binary fluids belong. For our experiments, we only concerned with the
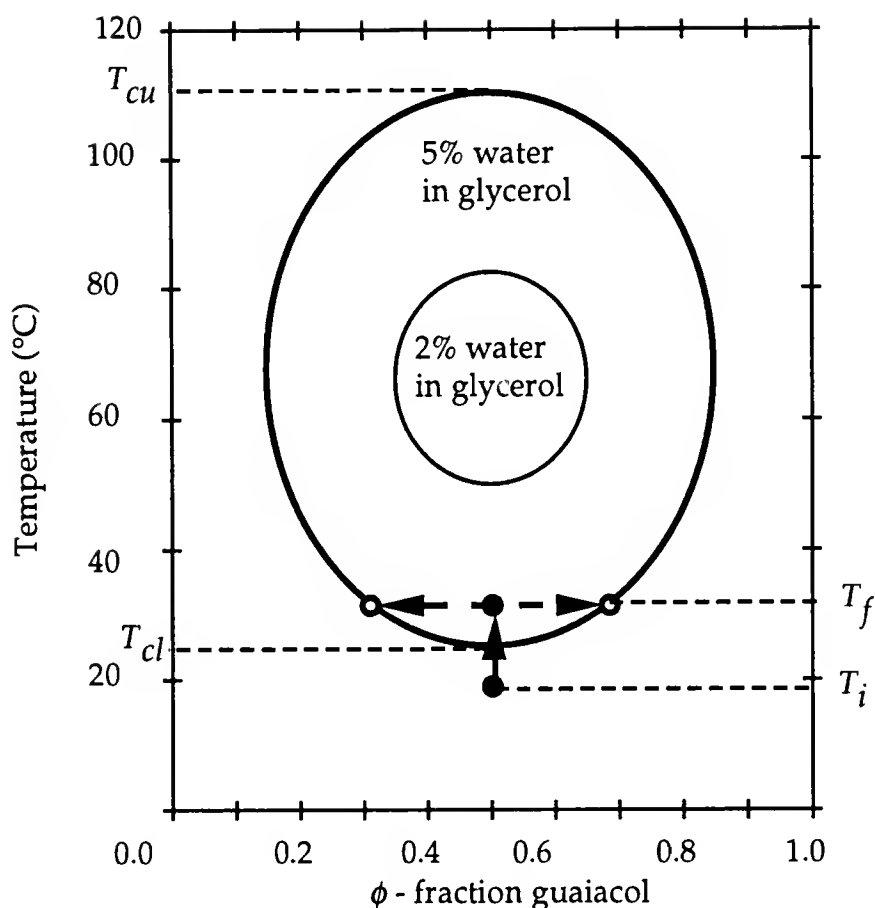
Fig. 4.1 A schematic phase diagram of GGW mixtures with different water contents x. Without water (x=0), glycerol and guaiacol are fully miscible in any proportion. A miscibility gap opens up when $x \geq 1.4\%$, and the coexistence curve is a closed loop centered around temperature T_0= 63.1⁰C. Inside the loop, the mixture phase separates into two phases. The size of the loop increases with the water content x, as shown schematically with two loops for x is about 2% and 5% respectively. Each loop has two critical temperatures T_{cu} (UCST) and T_{cl} (LCST), when $x \geq 5\%$, the loop is large enough that the two temperatures are well separated and independent from each other. Our experiments were restricted in the neighborhood of T_{cl} (LCST) on the phase diagram, where the mixture was initially equilibrated at T_i, then quenched to T_f inside the coexistence loop and started phase-separating, which we studied by means of light scattering.
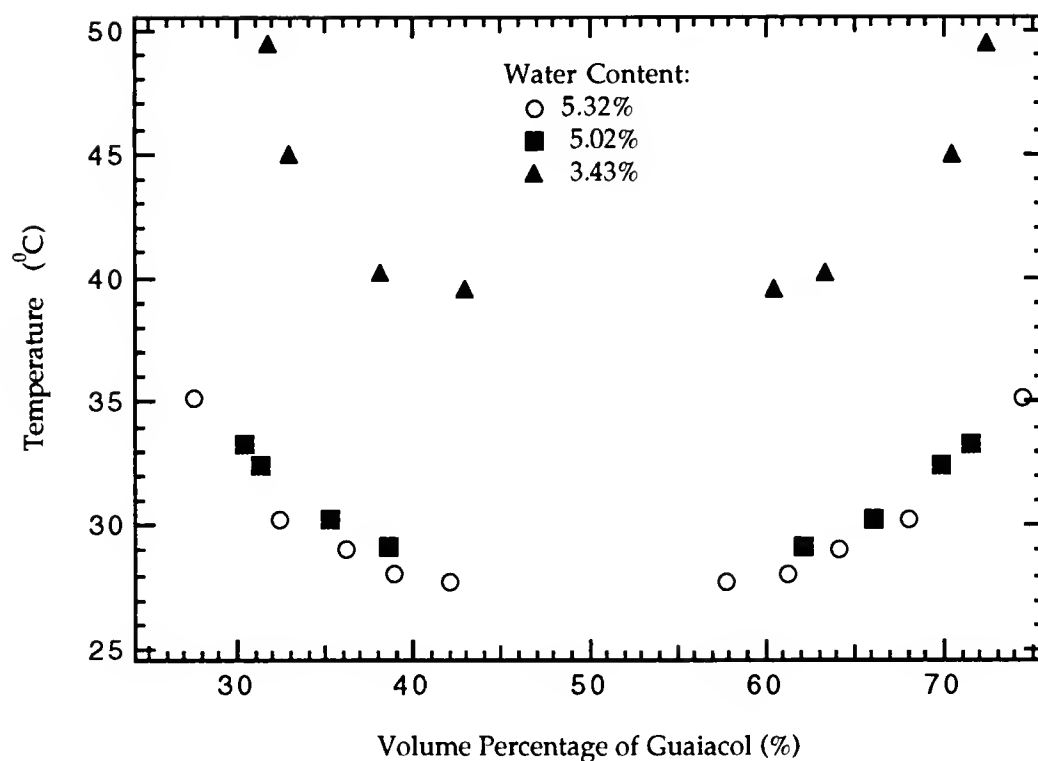
Fig. 4.2 Coexistence curves in the neighborhood of LCST for several GGW mixtures with different water concentrations. The LCST T_{cl} is very sensitive to the water content in the mixture, as it decreases significantly with the increase of the water content.

LCST. The water content of the mixtures we have used was about 5.9%, where the difference $T_{cu} - T_{cl}$ is over 60 °C.

We mapped out the phase boundary (coexistence curve) around the LCST for several mixtures with different water contents, and the results are shown in Fig 4.2. For each water content, we made a whole series of mixtures with different mass ratios of glycerol-water and guaiacol, ranging from 80%:20% to 20%:80%, contained in 15 ml vials. Then the vials were submerged in a refrigerated Neslab water bath. At any temperature within

the range of the miscibility gap $(T_{cl} < T < T_{cu})$, some vials would phase separate while other still be homogeneous. At each temperature, we measured the volume ratios of the two phases in those vials that had been fully phase-separated. From the volume ratio and the original concentration of the mixture, we determined the phase boundary. Before taking measurements at the next temperature, these phase separated samples had to be remixed again, preferably at a temperature where they were miscible. The results from three series of mixtures are plotted in Fig. 4.2. As we were only interested in the part of phase diagram in the neighborhood of the LCST T_{cl}, we limited our measurements to the relevant area.

As we can see from Fig. 4.2 that the phase diagram around the LCST is remarkably flat. This feature was found in earlier experimental studies [Johnston, 1983] and the WV model. It made difficult to find the critical concentration C_c. Fortunately the phase diagram is approximately symmetric, therefore it is reasonable to assume the midpoint of the flat part as the critical concentration, which is about 50% of guaiacol by volume and 48% by mass.

4.3 Sample Cell and Carrier

Our sample cells consisted of a sandwich of a fused quartz window and a sapphire window separated by a Teflon gasket, with the GGW mixture in between, and clamped in a stainless steel carrier with four screws (see Fig. 4.3). Both of windows had diameters of 1 inch, but the sapphire window was 0.5 mm in thickness while the quartz was about 1.6 mm (1/16 inch). We chose Teflon gaskets because of its chemical stability, after we had numerous experiences with the corrosiveness of guaiacol, which dissolved several kinds

of epoxies that we could find. The Teflon gaskets were made from virgin skived Teflon sheet purchased from PTFE Industries Inc., these sheets have a superior surface smoothness compared to those commonly available. We purchased these Teflon sheets of various thicknesses in order to have samples of different thickness, which ranged from 0.2 mm to 1.0 mm.
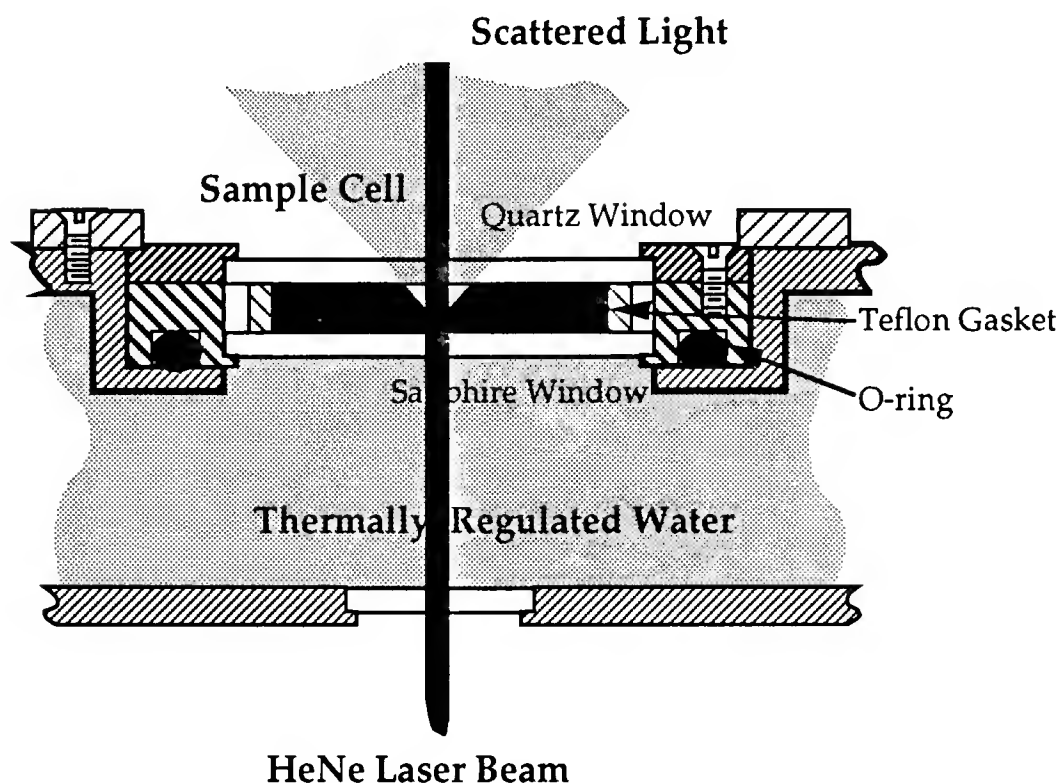

Fig. 4.3 A cutaway view of sample cell and heat exchange chamber configuration as in the light scattering apparatus. The stainless steel parts are slant shaded, the GGW mixture (dark shaded) is enclosed between a sapphire window and a fused quartz window by a Teflon gasket, the sapphire window is in contact with the thermally regulated water(light shaded). A laser beam incidents upwards from below, as shown in Fig. 3.3.

The sample cell was then mounted onto a heat exchange chamber, with the sapphire-window side in contact with the circulation water of constant temperature, and the fused quartz window exposed to air (see Fig. 4.3). Sapphire is known to have a much higher heat conductivity and hardness than fused quartz or any other types of glass because of its crystallinity. The hardness of sapphire enabled us to use thin window that still could stand the force of clamping without breaking. Also because of the low thermal conductivity and larger thickness, the heat exchange across the quartz window should be minimal compared to the sapphire side. Consequently the sample was able to reach thermal equilibrium with the circulating water quickly and was not much affected by the ambient temperature on the quartz window side. In addition to the quartz window, we chose the water content of the GGW mixture so that its LCST, T_{cl}, was close to the room temperature of the our laboratory, the heat exchange between air and the sample through the fused quartz window should be negligible.

The GGW mixture was loaded into the sample cell inside a refrigerated purge box, which was modified from a small commercial refrigerator purchased from Sears, equipped with gloves and a see-through window. Before and throughout the loading process, the box was constantly purged with a dry nitrogen flow. Thus it provided a dry environment at a temperature several degrees lower than the room temperature, which prevented phase separation in the mixture from handling or accidental temperature fluctuation. A sample cell of 0.8 mm thick contained approximately 10 µl of the GGW mixture, and most of our studies were performed on samples of that thickness. It usually had an air bubble about 3 ~ 5 mm in diameter inside, which facilitated the mixing and homogenizing the

mixture once inside the cell if necessary. Due to the relatively small volume of the sample cells, the critical temperature T_{cl} of each sample cell was different even though GGW mixture was drawn from the same container, and the variation T_{cl} of could be as large as 0.5 °C. This was understandable as we knew that T_{cl} was very sensitive to the water content of the mixture (see § 4.1). There might be some change of water content during the transfer of the mixture from the container to the sample cell, when the mixture was exposed to the ambient environment for a however brief moment. After the sample cell was sealed and clamped, T_{cl} was still noticeably drifting downwards over time on the average of about 0.005 °C per week, presumably due to the absorption of moisture by glycerol in the mixture through the gasket. But overall, the Teflon gaskets gave a reasonably good seal.

4.4 Data Acquisition and Processing

Before every quench, the sample was first allowed to equilibrate at initial temperature T_i which was about 0.1 to 0.2 °C below the critical temperature T_c for at least two hours. Normally this time was between 6 to 12 hours if not more. Then it was quenched to a final temperature T_f inside the miscibility gap by 0.01 to 0.15 °C. The quench was effected by simultaneously turning a pair of 4-way valves, which resulted the higher temperature water being routed to the heat exchange chamber and the sample cell instead of the lower temperature water (see §3.2). Following the quench, we measured the scattered light intensity with the CCD camera, with equal interval of time between measurements for every sequence that consisted of 20 measurements, the interval subsequently increased exponentially for later

sequences as the phase separation proceeded, in deference to the power law behavior observed in the measurable quantities over time. The exact time of the interval depended also on the quench depth ΔT, which determines the dynamic time scale τ_0 through the relation

$$\tau_0 = \xi^2/D, \tag{4.2}$$

where ξ is the correlation length, which relates to ΔT as Eq. (1.1a) (see. § 1.1), and D is the interdiffusion constant.

The temperature of the sample was read with a Yellow Springs Instruments (YSI) thermistor with a nominal resistance of 30 kΩ at 25 °C. It was located inside the heat exchange chamber next to the sapphire window of the sample cell. The abruptness of the temperature quench and the temperature stability following the quench could be monitored in this way, and a typical temperature profile has been shown in Fig. 3.7.

The structure functions were calculated by averaging together 20 or 40 adjacent rows of pixels on the CCD image; the row corresponding to the scattering plane, and same number rows on each side of the plane. This averaging helped to reduce the laser speckle noise in the structure function profile, and increase the sensitivity to low light levels at large momentum transfer by improving the photon counting statistics. Before every quench, the background noise was measured, and later subtracted from all subsequent data set to eliminate the effects of scattering from imperfections on the glass surfaces, dust and dirt, and other static sources, such as the dark current from the CCD chip. Each measured structure function was also corrected for the fact that the scattered light from scattering volume had to go through two interfaces, the first between the liquid mixture to quartz glass and the second

between quartz glass and air, before exiting the sample cell; at each interface, the scattered light has certain probability of being reflected, and that probability increases with the scattering angle θ. Thus the scattered light intensity directly measured by the CCD camera was reduced, especially at larger angle θ, by as much as 14%. The correction could be simply calculated from the Fresnel formulas [See, *e.g.* Hecht, 1987], and thus we called the correction the Fresnel factor. In summary, the final structure factor $S(q)$ is calculated from measured light intensity I as

$$S(q) = \frac{I(q) - I_B(q)}{F(q)} \qquad (4.3)$$

where I_B is the background, and F is the Fresnel factor just mentioned.

4.5 Treatment of Glass Surface with Trichlorosilanes

With the observation of the fast mode in the GGW mixtures [Shi et al., 1993], it has been established that it is generic to a broad class of fluid mixtures, as now the same phenomena had been seen both in a polymer system and a simple low-molecular-weight binary fluids. Furthermore, we had evidence that this new mode of phase separation is mediated by solid substrate surface (container wall), *i.e.*, driven by the wetting dynamics of the three phases involved: two phase-separating liquid phases and the solid substrate phase. We will discuss our results and supporting evidence for this picture in detail in the next chapter, here I only want to briefly state our motive for chemically altering the surface properties of the substrate and the method that we used.

Based on our assumption that the fast mode is a surface-mediated phenomenon, we would expect the modifications the surface properties of the substrate will change the interactions among the three phases. It was well known that the glass surface chemically treated with a trichlorosilane compound became hydrophobic, and in phase separated binary fluids, it was experimentally observed that it effectively inverted the preferentially absorbed phase on the glass surface [Dixon et al., 1985], and in addition, the modification could result in shifting the wetting temperature T_w up to 10 °C [Abeysuriya et al., 1987; Durian and Franck, 1987]. The same phenomenon was seen in our phase separated GGW: when a glass surface was just cleaned with sulfuric acid, the glycerol-rich phase (or lower phase, because glycerol is denser than guaiacol) will preferentially wets the surface; after it was treated with phenethyltrichlorosilane (PET), the guaiacol-rich phase (upper phase) wets the glass surface. Using two types of capillary tubes, one was acid cleaned and the other treated with PET, situated across the phase separation meniscus, we experimentally demonstrated that the first case had capillary rise, while in the PET treated tubes had capillary sink, as shown schematically in Fig. 4.4. Therefore, the silane treatment of the glass surface effectively changed the surface tensions between the solid substrate and the two liquid phases. Based on our assumption that the fast mode is surface-mediated, we expected it should affect the dynamics of wetting and thus the fast mode.

We treated the window surfaces, both sapphire and quartz, with a self-assembled (SA) monolayer of silane compounds, and we chose the method mainly because of the simplicity of the procedure. The SA monolayer method was developed rapidly over the last ten years chiefly by chemists for
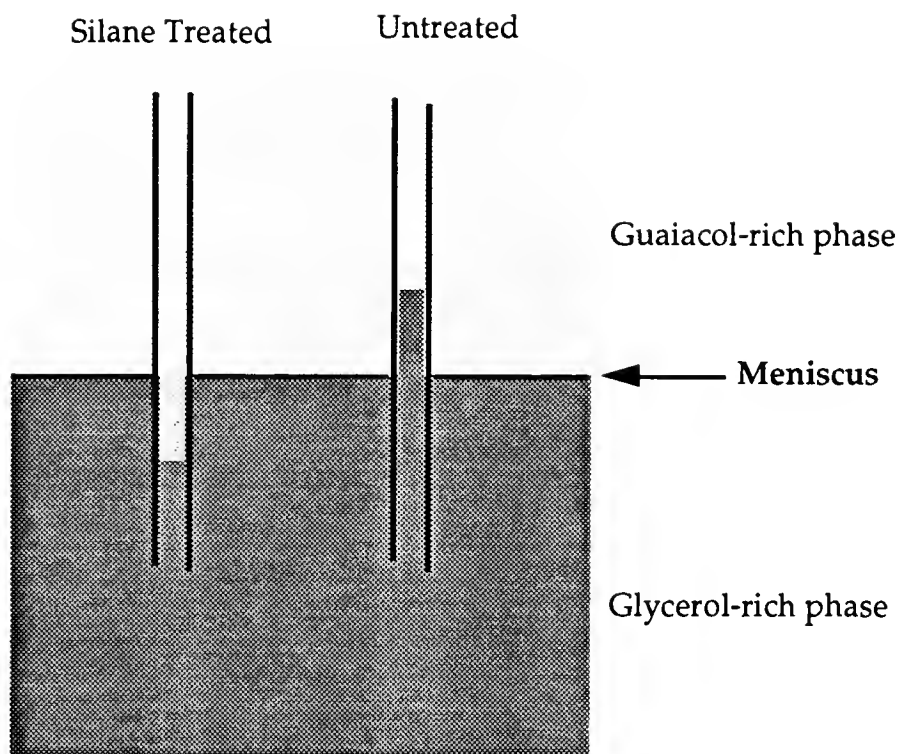
Fig. 4.4 Schematic representation of the capillary rise experiments. In fully phase-separated GGW mixture, glycerol-rich phase has a higher density, thus at the bottom while the guaiacol-rich phase at the top. In untreated capillary tube (on the right), glycerol-rich phase has a higher affinity to the tube wall, thus resulted in a rise. After the tube was treated with silane, the guaiacol-rich phase has a higher affinity instead, and that resulted in a capillary sink.

studying thin organic films [Ulman, 1991], which have the potential applications in a whole range of fields, like molecular electronics and nonlinear optics, etc.. The substrates used for the monolayer treatment had included metals, metal oxides, and most often glasses. The silane compounds were specially apt to form monolayers on the glass substrates, mainly because these silanes usually were surfactants like soaps, they had a polar head group centered on the silicon (see Fig. 4.5A), and a nonpolar alkyl (hydrocarbon) tail

of various length. They spontaneously assemble into monolayer films on an appropriate substrate immersed in the solution, with the head groups binding to the substrate and the alkyl tails stretching out. The substrate surface is usually polar. The polar head group is attracted to the substrate surface and then chemically binds to the surface where a molecular monolayer thus forms eventually, *e.g.*, for glass, a fully hydroxylated surface yields better monolayer film. A simplified scheme of the process is shown on Fig. 4.5. This monolayer effectively insulates the original substrate from anything that comes in contact, and thus drastically changed its surface properties.

The self assembled monolayer has a higher stability compared to the organic films deposited in other ways, e.g., Langmuir-Blodgett films, because the molecules are chemically bonded to the surface. For our experiments, it is important to have the film stable enough so it could withstand to the attack by the GGW mixture, at least for a period of several weeks.

We have used the four trichlorosilanes for the treatments of the glass windows: ethyltrichlorosilane (C_2H_5-$SiCl_3$)(ETS), decyltrichlorosilane ($C_{10}H_{21}$-$SiCl_3$)(DTS), octadecyltrichlorosilane ($C_{18}H_{37}$-$SiCl_3$)(OTS) and phenethyltrichlorosilane(C_6H_5-C_2H_4 $SiCl_3$)(PET), all these chemicals were purchased from Huls America Inc.. The first three compounds belong to the same homologous series and thus shared very similar molecular structures, and the only differences are in the lengths of the alkyl chains, which increase from 2 carbons in ETS to 18 carbons OTS. PET has a phenyl ring at the end of the tail, and therefore should have higher affinity for guaiacol molecule than glycerol. This had been confirmed in our capillary rise experiments.

The windows (both sapphire and quartz) were first cleaned in the so called "Piranha" solution made from sulfuric acid and hydrogen peroxide(30%) at 3:1 volume ratio. Caution must be taken in handling this

solution, as it reacts violently with any organic matter, which it literally "eats" away, and it should only be handled inside a fumehood. The windows were submerged in the "Piranha" solution for about an hour before being taken out. Afterwards they were rinsed thoroughly with deionized water, ethanol and acetone in sequence. Then they were dried in a nitrogen stream at room temperature. After the cleaning with the "Piranha" solution, the window becomes more hydrophilic compared to the original surface, as the glass surface is saturated with OH groups [Dixon et al., 1985], and hydroxylated. These windows could be used to make sample cells or further treated with the trichlorosilanes.

To treat the windows with the trichlorosilanes, we made a solution of each compound. As solvent we used 70% hexadecane with 30% chloroform by volume, and then we added 1% of trichlorosilane by volume to make the solution. Because all trichlorosilanes react with water to form polymers, all the processes involving them must be done inside a dry glove box. After windows had dried, they were submerged in the trichlorosilane solution for about 10 minutes before being taken out again. Then as an indication of a successful treatment, the windows should be dry and clean, and no droplets of solvent were left on the surface as they were withdrawn from the solution.

Thus the surface modification enabled us to change the surface tension between the fluid phases and the solid substrate, as established experimentally. The light scattering experiments were then carried out on these treated windows, the results of which will be discussed in the next chapter.
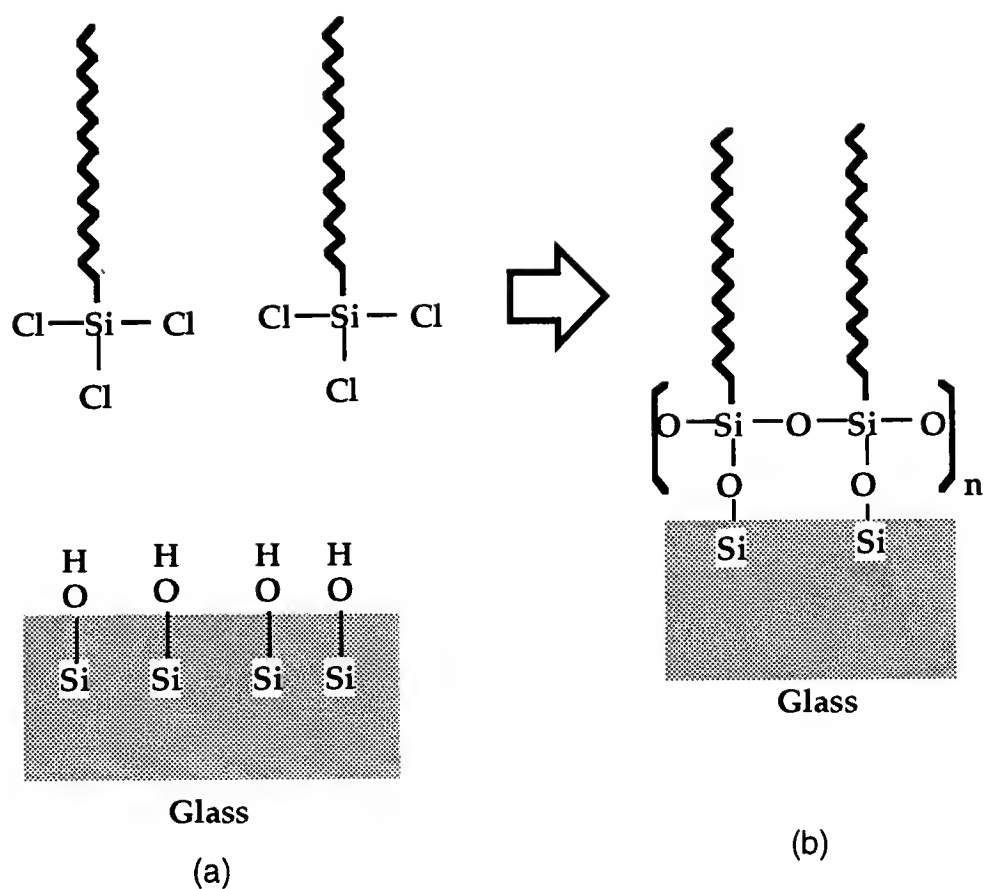
Fig. 4.5 Trichlorosilane monolayer formation on glass surface. Here we use OTS as an example, it has a 18 carbon tail and a strongly polar head centered at a silicon. (a) Before the treatment with silane, the glass surface is fully hydroxylated, i.e., saturated with - OH groups, which attracted the polar heads of the silane molecules. (b) After the treatment, a monolayer of OTS formed, each OTS molecule is chemically bonded to the glass surface in addition to the nearest neighbors.

CHAPTER 5

RESULTS AND DISCUSSIONS

This chapter is primarily concerned with the methods of data analysis and the results of our experiments. Our main efforts will be on the fast mode, whose properties I will try to outline. However, I find it necessary and useful to give an adequate description on the slow mode, and present the evidence of it being the phase separation mode in the bulk, which had been thoroughly investigated by the previous researchers in the field (see § 1.5). We will discuss the fast mode in full detail and its properties, including some results from the video microscopy studies. These fast mode results are compared with those from polymer mixture by Cumming and coworkers [Cumming et al., 1992]. Finally, we will discuss the surface treatments and their effects on the fast mode.

5.1 Data Analysis

So far we had limited our investigation to the spinodal decomposition process in a GGW mixture with critical concentration C_c, which is 47.9% of guaiacol by mass, 50.3% by volume. For critical quenches, we observed the well known spinodal rings associated with the bincontinuous interpenetrating network morphology seen in phase separation via spinodal decomposition. The
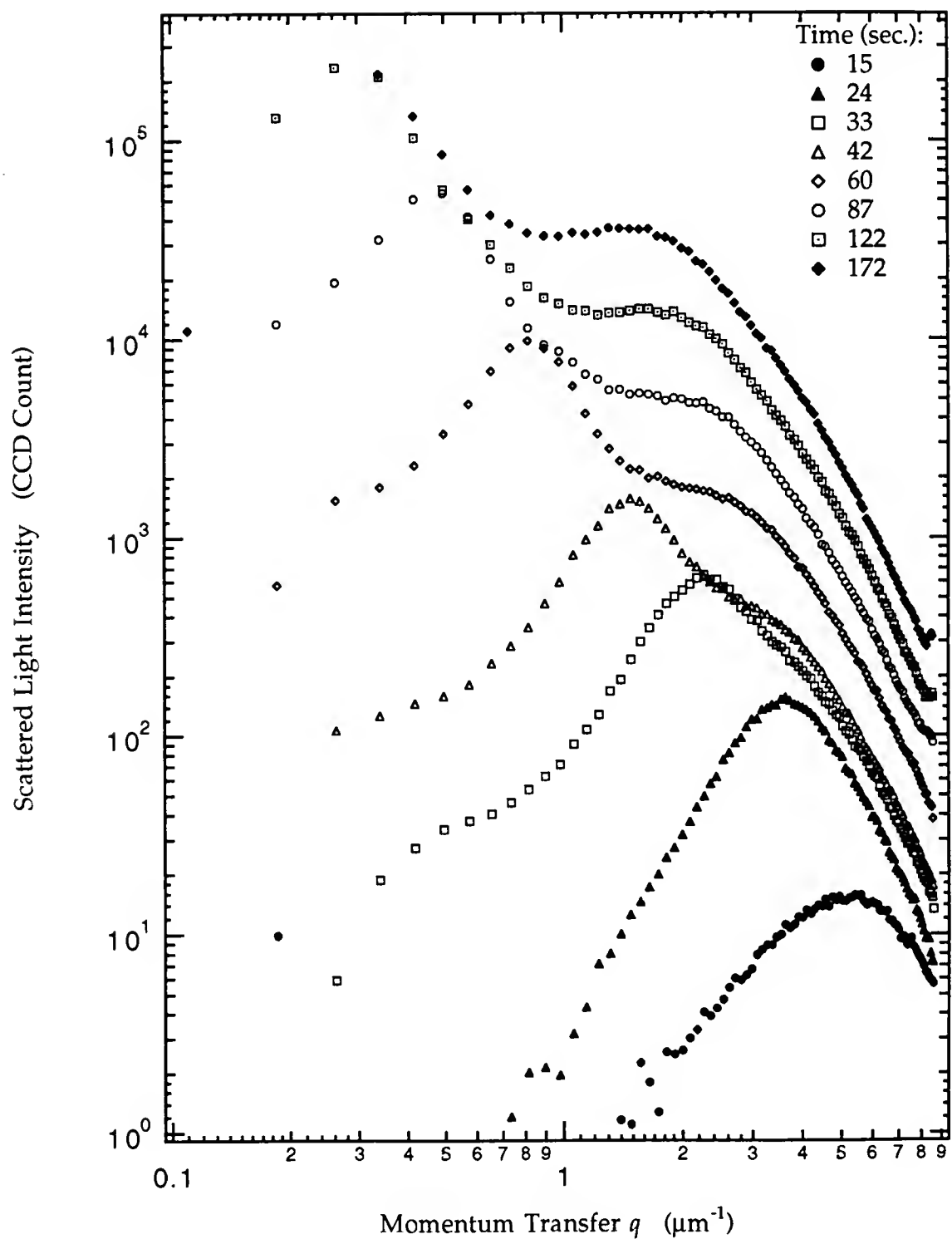
Fig. 5.1 Structure functions at various times after a quench of 0.111°C above T_c The 4 functions of later times have been scaled up by a factor of 2 consectively to avoid overlapping of the data.

(A)　　　　　　　　　　　　　　(B)

(C)　　　　　　　　　　　　　　(D)
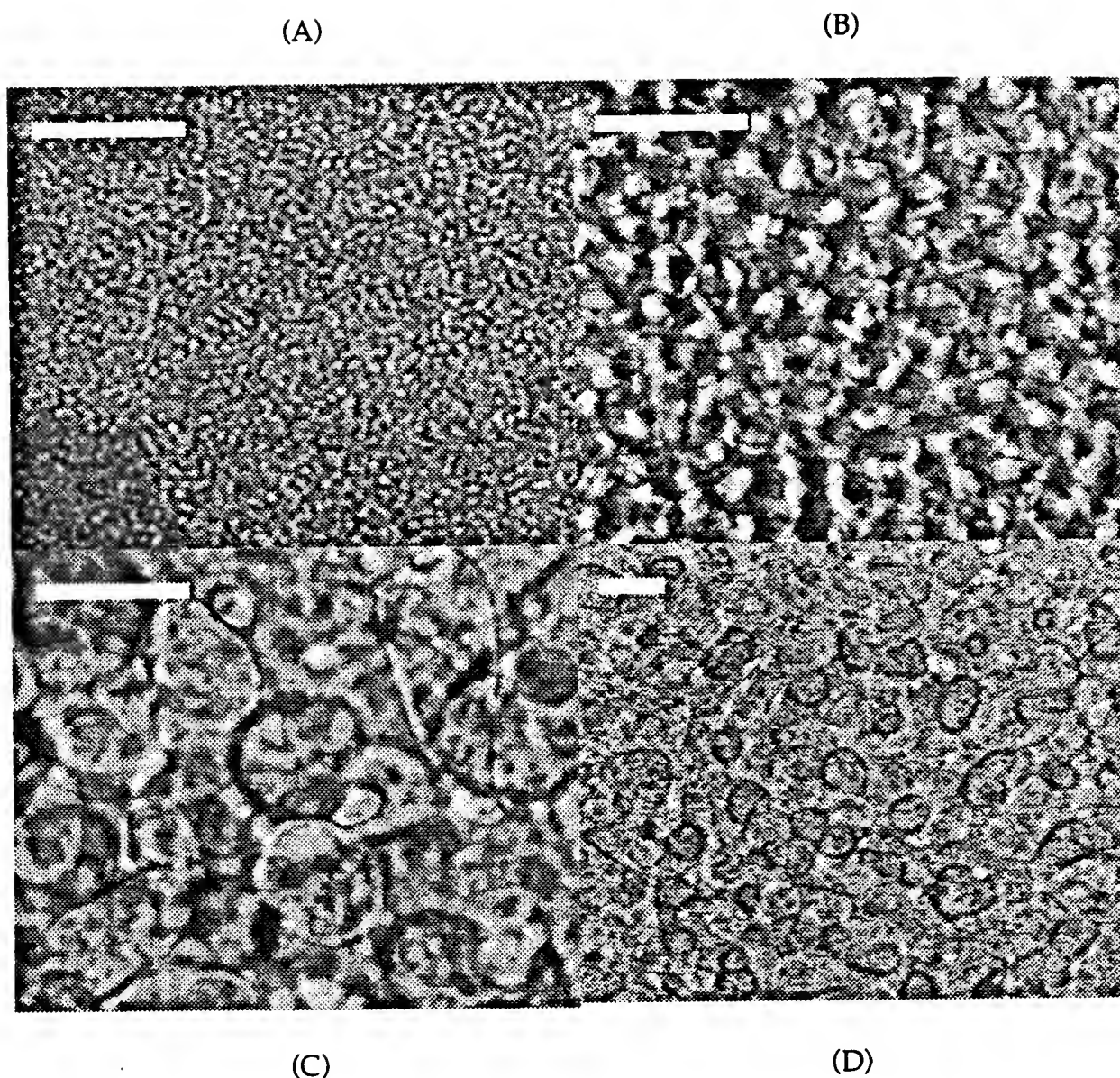
Fig. 5.2　A sequence of video micrographes of GGW mixture undergoing a phase separation. At time t =0, the mixture was quenched into the miscibility gap by a depth of 0.145 ^{o}C. Before the quench the mixture was homogeneous and structureless. Structures similar to those in spinodal decomposition gradually started to emerge after the quench . These eight micrographes were taken 25 , 60, 190, 210, 382, 415, 595, and 740 seconds in sequence, respectively, following the quench. The longer white bar shown on the upper lefter corner in A, B, C, and H is 60 μm in length, while the shorter bar in D, E, F, G is 50 μm in length. This difference of was simply due to the switching from a 32X to a 10X objective in microscope. Micrographes A to F show the growth of the fast mode, (Continued to the next)

(E) (F)

(G) (H)
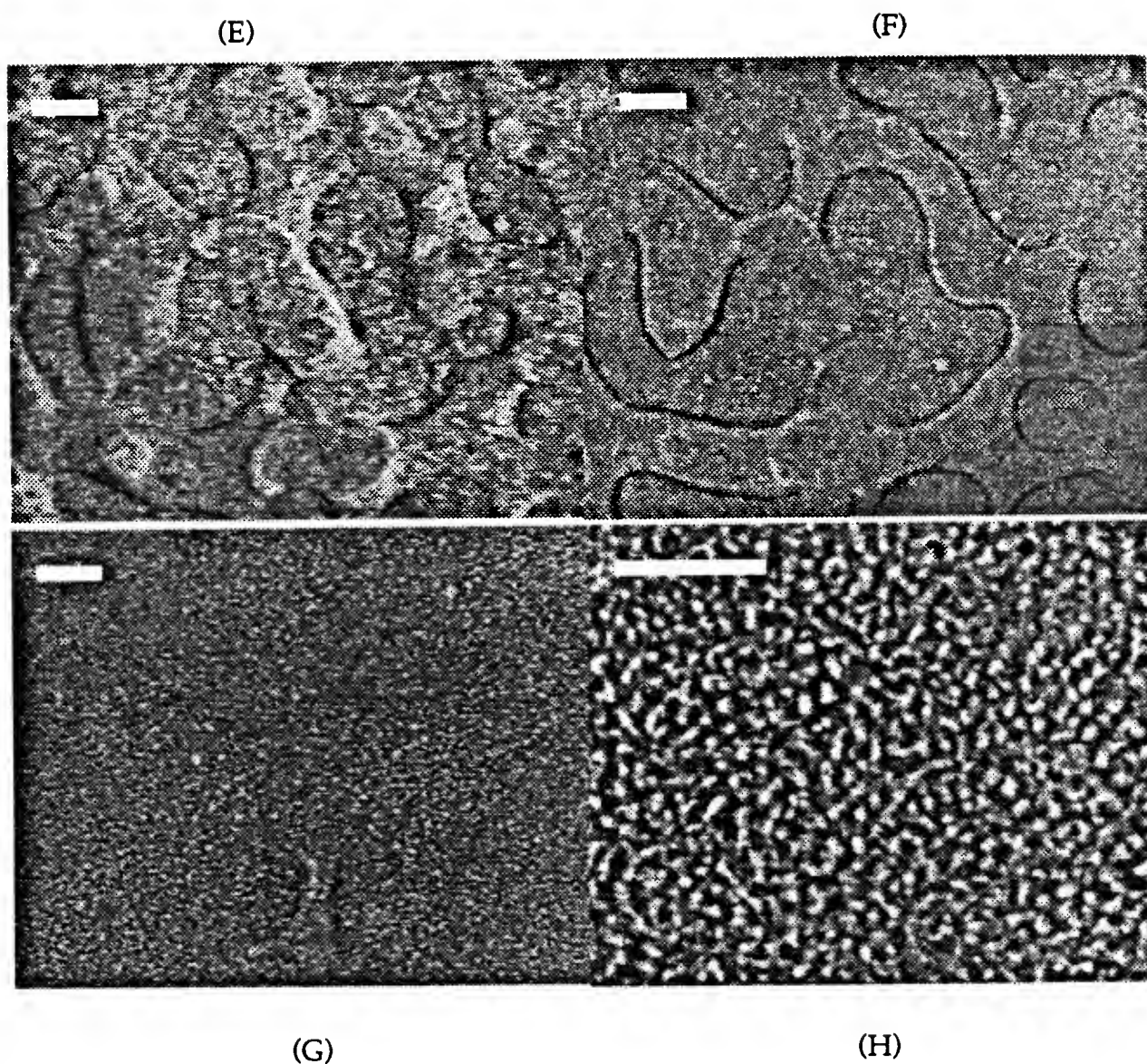
(Continued from the previous page), while the microscope was focused at about 20 μm above the surface of the quartz window. G and H show the slow mode growth, when the microcroscope was focused on a plane about 300 μm above the surface. At later stage, the fast mode morphology was quite anisotropic, as seen in E and F, it looks like one of the fluid was spreading across the plane while replacing the other fluid. E was taken using the schlieren technique, the fuzziness of the graph was partly due to the slow mode, which was outside the focal plane of the microscope. The fast mode was almost gone by the time of the graph G was taken, only a remnant of it could be seen in the center lower region of G.

major difference of our experiments are the observation of two spinodal rings, instead of one as in most of other experiments. Fig. 5.1 shows a time sequence of the scattered light profiles, or structure functions, it clearly shows the emergence and development of two peaks and their evolution. These data had been averaged over every 10 neighboring pixels, in order to reduce number of data points in each structure function to about 100, so that each data point could be clearly represented in the Figure. Also as a result of the averaging, the noise in the data had been reduced. The two peaks correspond to the two length scales presented in the system, as can be seen in Fig. 5.2, which is a time-series of video-micrographes of a sample phase separating. The first six micrographes show the morphology and its growth of the fast mode, and the microscope was focused on a plane about 20 μm above the inner quartz window surface, the last two show that of the slow mode after the fast mode had finished, at a location about the middle of the sample cell. These micrographes clearly show the two distinct length scales presented in the sample, although at different locations in the sample.

As we were most interested in finding the time evolution of the peaks in the present research, we only wanted to extract two quantities from each scattering profile $I(q)$ in a time sequence: the peak position and peak intensity. The peak position is directly related to the average domain size, and from its evolution we get the growth law. The peak intensity is a quantity crucial in testing the scaling hypothesis and other properties. So we chose two simple functions for the model line shape: for the fast mode, we used a gaussian, i. e.,

$$S(q) = I_f \, exp\left\{ -\frac{(q - q_f)^2}{2\sigma^2} \right\} + I_0, \quad (5.1)$$

where I_f, q_f, σ and I_0 are the fitting parameters, q_f, and σ are the peak position and peak width, respectively, and the sum of I_f, and I_0 is the peak intensity; for the slow mode, we chose one of the Furukawa functions (eq. (1.43)), and let $\gamma = 4$, then

$$S(q) = I_s \frac{3\left(\frac{q}{q_s}\right)^2}{\left(2 + \left(\frac{q}{q_s}\right)^6\right)},$$

(5.2)

where I_s and q_s are slow mode peak intensity and peak position, respectively. We chose the model function largely because at large $q \gg q_s$, $S(q) \sim q^{-4}$, which is known as the Porod law [Porod, 1951; Porod, 1982]. This characteristic tail is due to scattering from sharp interfaces in three dimensional systems. In our experiments, we would expect to see the q^{-4} tail at the late stage of phase separation, when the slow mode peak position q_s is fairly small, mainly due to the limited range of q window of our apparatus. At this stage, well defined interfaces should have developed and thinned. Fig. 5.3 illustrates such an asymptotic approach to the q^{-4} behavior, where the tails ($q \gg q_s$) of the structure functions become increasingly parallel to the q^{-4} line, which is a straight line on a log-log plot, at later stages of phase separation.

Our primary interest was in the peak positions as functions of time, $q_f(t)$ and $q_s(t)$, and the peak intensities as functions of time, $I_f(t)$ and $I_s(t)$. The model functions (eq. (5.1) and eq. (5.2)) served reasonably well individually as peak finders when fitted to the experimental data with a least square fitting routine. For the fast mode, we usually limited the fitting in range q-space to the interval between 1000 cm^{-1} and $q_f + \sigma$, which corresponds approximately

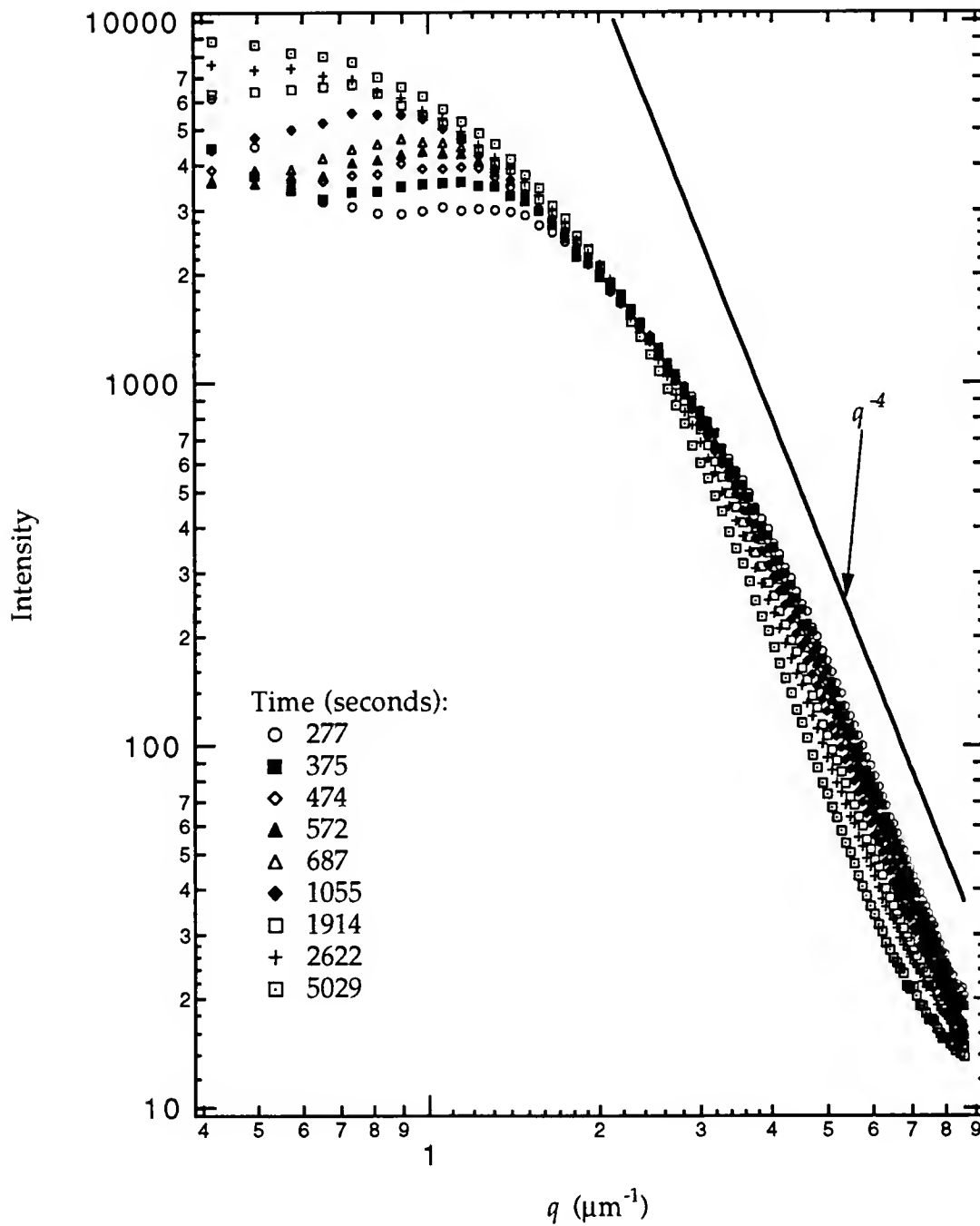Fig. 5.3 Late time structure functions of a quench of depth 0.09°C. As the phase separation proceeded, the tail of the structure function approached asymptotically q^{-4}, satisfying the Porod law. The peak in the structure function corresponds to the slow mode.

to the point where the structure function falls to half of its peak value. The lower limit of 1000 cm^{-1} was due the beam stopper (see Fig. 3.1), which served the purpose of reducing the transmitting beam intensity I_t by several order of magnitude before reaching the CCD camera, and it also blocked the scattered light within a small angle which corresponded to 1000 cm^{-1} in q. The slow mode peak was fitted with the Furukawa function eq. (5.2), usually within a range of in q-space where the corresponding intensities were above one half of peak value. Fig. 5.4 illustrates the fitting of both model functions to fast and slow mode, respectively, in the structure functions following a typical quench. Both fitting functions worked reasonably well, within their limited range of q-space, they adequately fitted the data, so that the fitting parameters q_f, q_s, I_f, and I_s could be determined as functions of time. Among the fitting parameters, the peak positions q_f and q_s were the most robust, especially q_f, simply due to the gaussian function.

A word of precaution is needed here. In our fitting scheme, the two peaks were fitted separately, although with two different model functions. That is, we fitted the same structure function twice, once for the fast mode peak, and the other for the slow mode. Each time we got the peak position and intensity as fitting parameters for one peak. Ideally, if we have one model function that could fit the structure function in the entire q-space, i.e., both of the peaks at once, we should have obtained the fitting parameters in a single fit. In comparison, our two-step fitting process would introduce certain errors in the resulting fitting parameters. For example, the peak position and peak intensity for the slow mode, q_s and I_s, could be strongly influenced by the tail of the fast mode peak, when the peaks were not well separated, as the fast mode intensity was usually far greater than that of the slow mode. Even
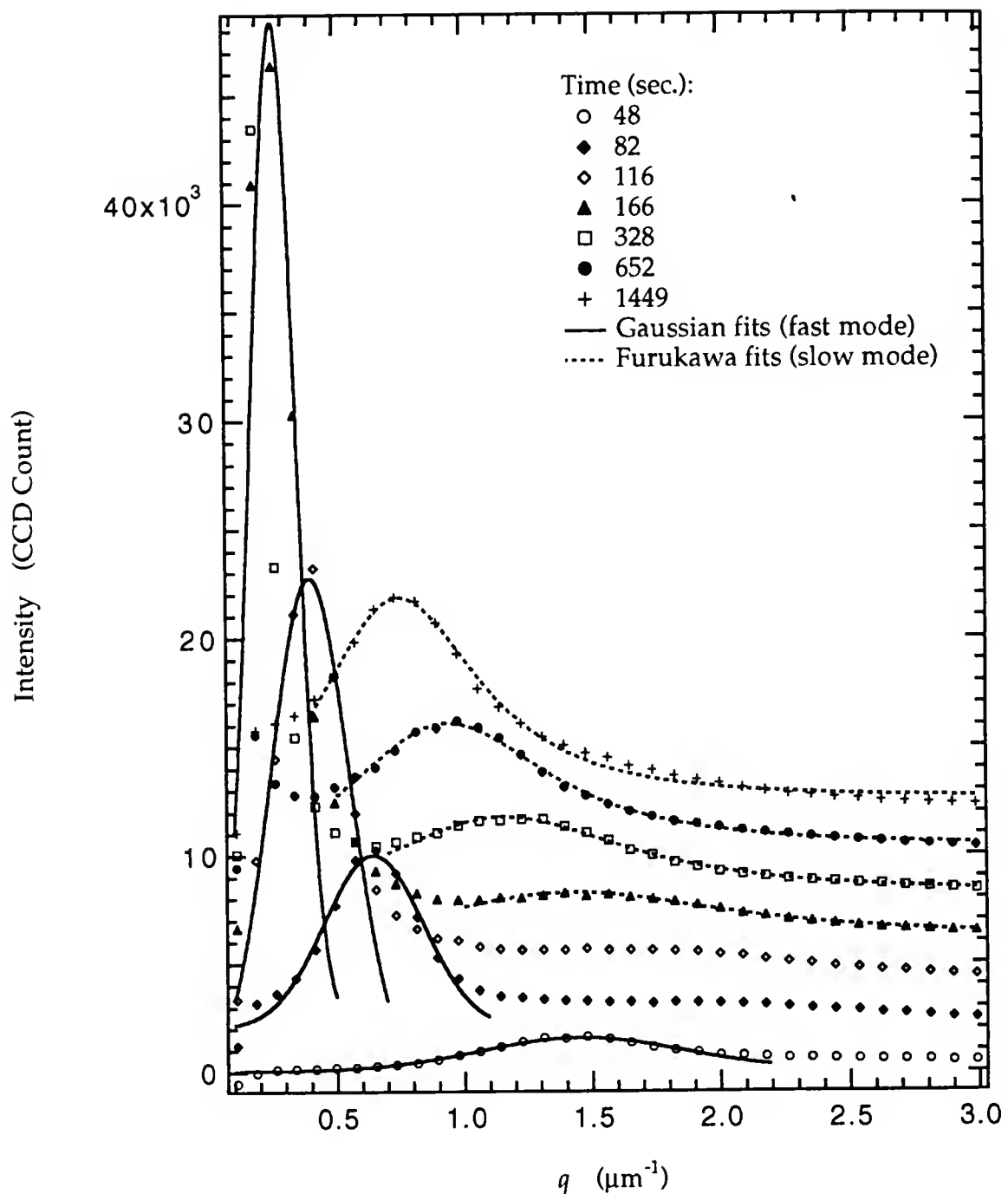
Fig. 5.4   The structure functions at various times as indicated after a quench of 0.082 °C. In the first three functions, at 48, 82, and 116 seconds, the slow mode peak hadn't fully developed.   At 328 seconds, the fast mode has gone forward into the beam stop.   The two types of fits, gaussian annd Furukawa functions, are illustrated for these data set.   Each successive structure function has had 2000 CCD count added to give the figure greater clarity.

when the fast mode peak had already gone into the beam stop, its tail at the location of the slow mode peak could still be substantial compared to the slow mode peak itself. Therefore, the fitting parameter q_s could be reduced and I_s increased artificially simply due to our two-step fitting process, especially when the two peaks were just emerging and thus not well separated. In that case, the error introduced could be too large to be ignored. Thus among the fitting parameters, the fast mode parameters q_f and I_f were more accurate than their counterparts of the slow mode, because in the same structure function, the fast mode intensity was usually far greater.

Sometimes the sum of the two model functions (eq. 5.1 and eq. 5.2) yielded good results in fitting the structure function in the entire q-space available in our experiment. One of the examples is shown in Fig. 5.5, the model function fitted the data very well, and the two peaks were fitted in a single step. To give greater clarity of the data and the fit function, we have added an off-set to the data, the earlier four structure functions have been off-set by 200 CCD count successively, and the four others at later times by 1000. At later times, the fit function showed progressively larger deviation from the data at the valley between the peaks and at the tail, part of it could be possibly attributed to the multiple scattering effect, as the quench depth was large enough, we would expect the contribution of the multiple scattering to be progressively larger as the phase separation proceeded. Also clearly seen in Fig. 5.5 is that the fast mode peak, which was fitted with a gaussian model function, evolved at a much faster rate toward $q = 0$ (beam stopper) than the slow mode, which was fitted with the Furukawa function (eq. (5.2)). Thus the former was conveniently named fast mode, while the later slow mode. We will give a detailed discussion on the kinetics of the two modes next.
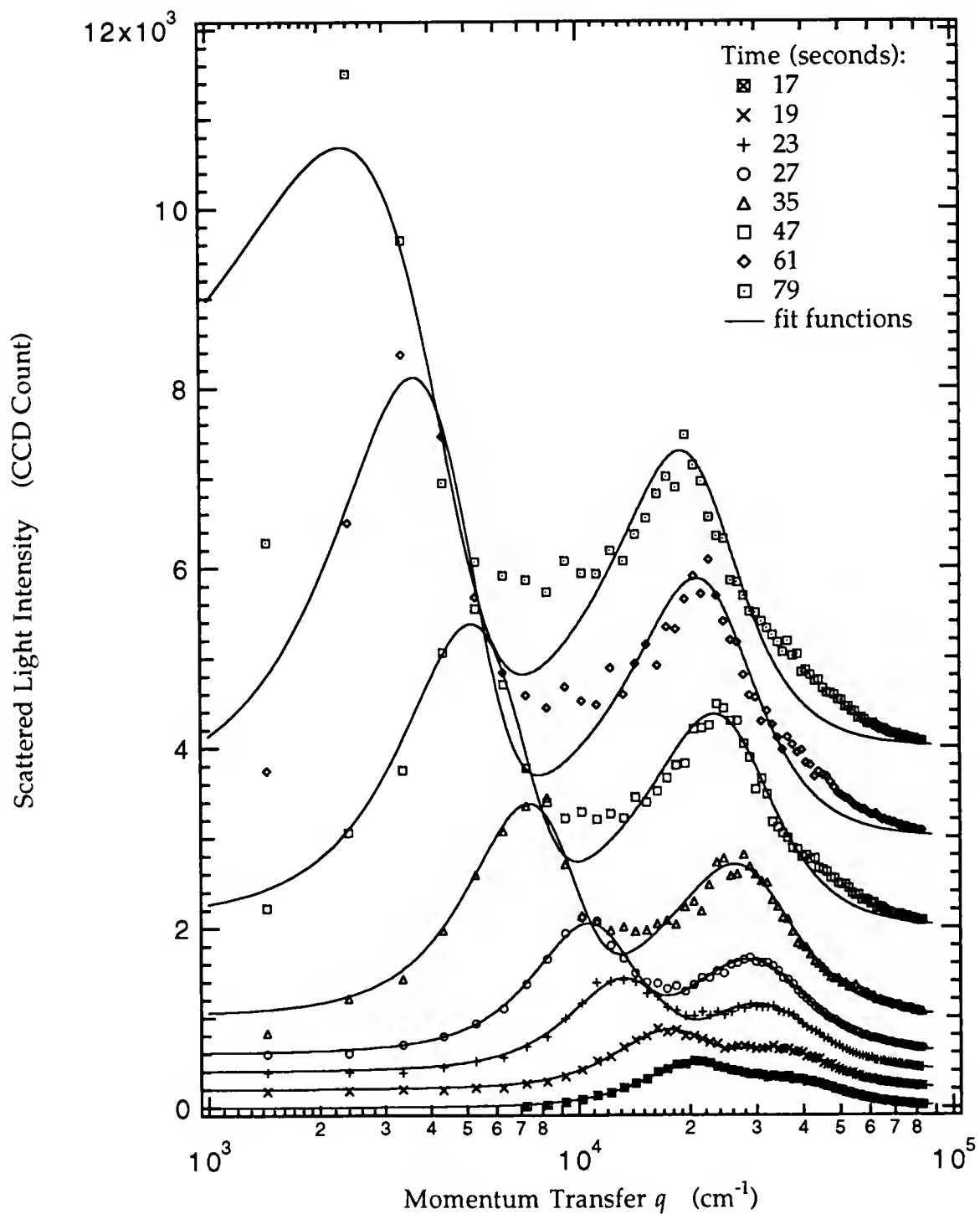
Fig. 5.5 Structure functions of after a quench of 0.126 °C into the miscibility gap and the fitting with the sum of gaussian and Furukawa function in the entire range of q-space available in our experiments.
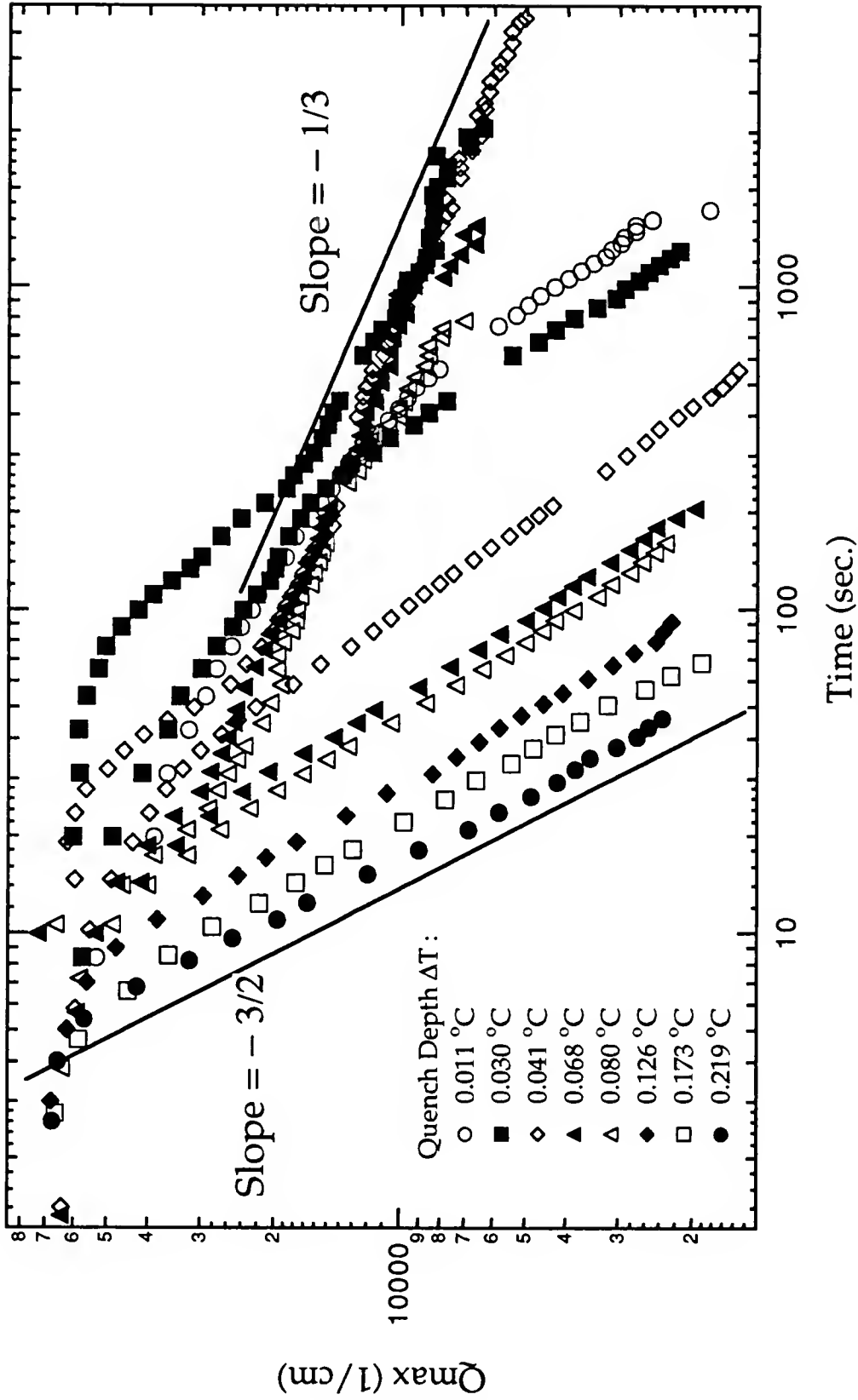
Fig. 5.6 Peak position in q-space vs. time for eight different quenches ranging in depth from 0.011 to 0.219 °C. Both fast and slow mode were observed in every quench, although not all the slow modes have been shown.
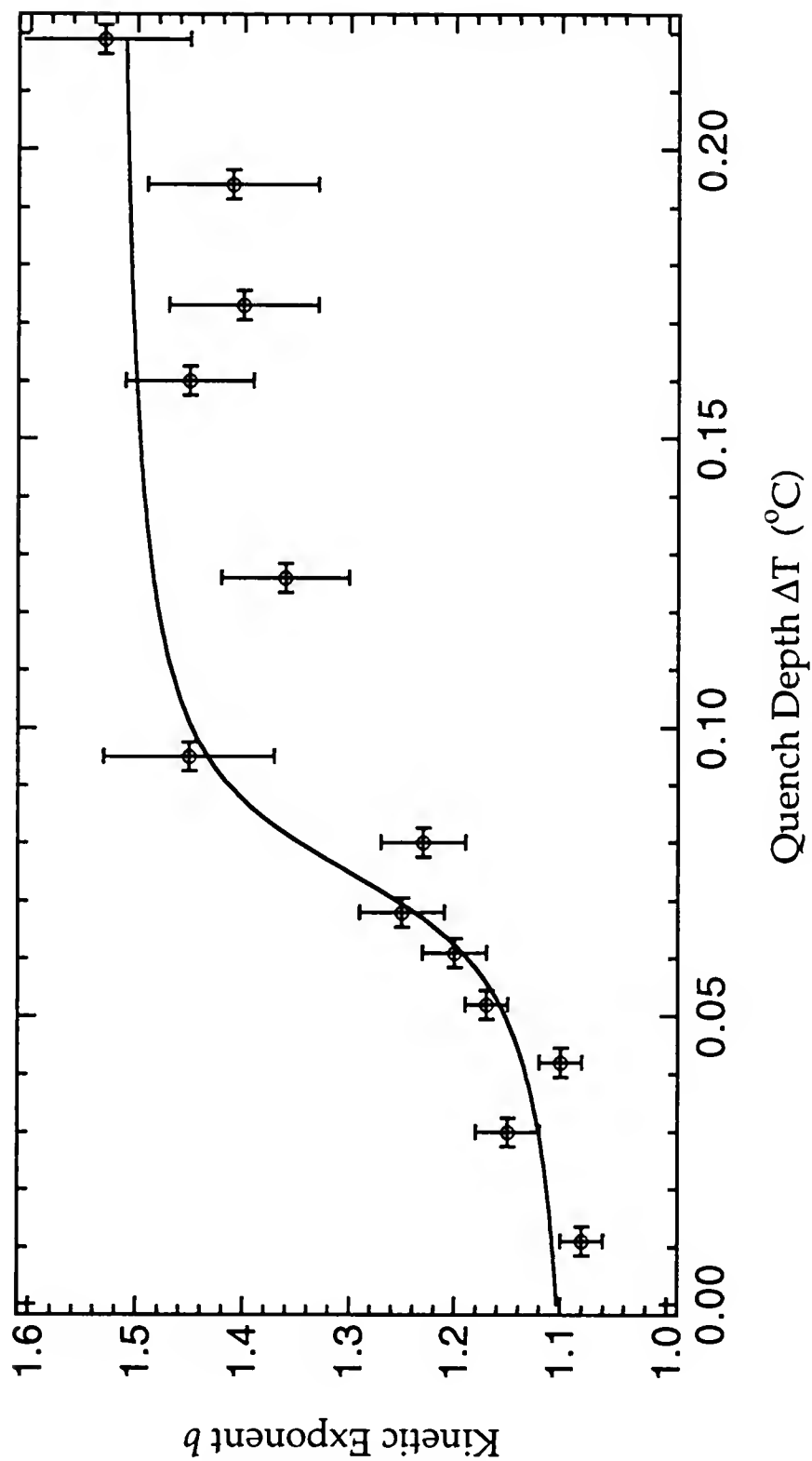
Fig. 5.7 The kinetic exponent of the fast mode vs the quench depth. For deeper quenches, the kinetics are fast and the couple of seconds uncertainty in the quench time translates into an uncertainty in slope on the logarithmic plot (as shown in Fig. 5.6) of nearly 0.1. The solid curve is a guide to a plausible trend in the data.

5.2 Phase Separation Kinetics

The evolution of the peak position Q_{max} as a function of time t is shown in Fig. 5.6, where both peak positions, which corresponded to fast and slow mode respectively, were plotted on logarithmic axes. The sample on which this set of data was taken was of 0.8 mm thick, and the GGW mixture was of critical concentration. As we know, a power law relation like $y = a x^b$ will be a straight line on a logarithmic plot of x and y, and the slope of the line equals the exponent b. From Fig. 5.6, we can see that after a certain amount of initial time following the quench, the evolution of the peak position approach a straight line in every quench depth, for both slow and fast mode. Therefore, the evolution of the peak position Q_{max} approximates a power law with time t at later stage, $Q_{max} \sim t^{-b}$, where b is called kinetic exponent and is usually chosen to be positive. Because the average domain size $L \sim 1/Q_{max}$, then the corresponding domain grows as $L \sim t^b$ at later stage.

On Fig. 5.6, we used the same symbol for the fast and slow mode data of the same quench. The slow mode data from different quenches approached the power law $Q_{max} \sim t^{-1/3}$ at later stage, and on the Fig.. I have drawn a line with slope - 1/3 next to the data for comparison. The slow mode data exhibited the power law with the kinetic exponent 1/3 over about two decades of time after an initial period following the quench. The kinetic exponent of 1/3 is exactly what had been theoretically predicted for systems where the growth and coarsening were diffusion driven (see §1.4), and this type of growth had been observed in binary mixtures of critical and off-critical concentrations undergoing phase separation (see §1.5 for details). The only noticeable difference between our slow mode data and those from other simple binary fluids [Chou and Goldburg, 1979; Wong and Knobler, 1978;

Goldburg, 1983] is the following of the diffusive growth over a prolonged period of time (about two decades) in our data, while in the earlier experiments, the diffusive growth mode with kinetic exponent of 1/3 was almost transitional in spinodal decomposition, and it was soon turned over to hydrodynamic growth mode with kinetic exponent of 1 as predicted by E. Siggia [Siggia, 1979]. This difference may be simply due to the high viscosity of the GGW mixture compared to the other binary mixtures previously studied. According to eq. (1.40), the growth due to hydrodynamic instability of tube-like structures is inversely proportional to the viscosity of the system. Therefore, the onset of this type of growth can be delayed in highly viscous fluids. In later experiments, we were able to follow the slow mode growth over even longer period of time, and there indeed we observed the crossover to the hydrodynamic growth. As a result, we identified the slow mode to be the normal mode of phase separation in bulk, as commonly observed in binary fluids.

In contrast, the fast mode data exhibited great difference from what had been observed previously. First of all, for all quenches, the peak position Q_{max} followed a power law t^{-b} after a transitional period of time, which is quench depth dependent, as shown in Fig. 5.6. However, the fast mode peak Q_{max} evolved much faster, and that is represented by a much larger kinetic exponent b than the slow mode, it increases from 1.1 at shallow quench to about 1.5 or 3/2 at the deepest quench allowable in our experiment with the quench depth, which we have shown in Fig. 5.6 by placing a line with slope -3/2 next to the fast mode data. The change of the kinetic exponent b with quench depth is shown in Fig. 5.7. Its trend of increase saturates at around 3/2 for quench depth beyond 0.10 °C. The fast mode is truly fast in terms of kinetic exponent, which has not been observed before, but also in the sense

that no theory so far has been able to predict or explain any kind of growth of faster than t^1, i. e., $b > 1$.

To compare our experimental results with those from other system, like that from polymer mixtures [Wiltzius and Cumming, 1991], we needed to express our data in appropriate dimensionless units. As we know, the correlation length ξ played a central role near the critical point T_c, and it is natural unit of length. Therefore we introduce a dimensionless variable K_{max}:

$$K_{max} = Q_{max} * \xi. \tag{5.3}$$

And the unit for time is t_0, which is the time need to diffuse across a correlation length ξ:

$$t_0 = \xi^2 / D, \tag{5.4}$$

where D is the interdiffusion constant, and is given by as

$$D = k_B T_c / 6\pi \eta \xi, \tag{5.5}$$

and η is the viscosity of the fluid. It vanishes at the critical point due to the divergence of the correlation length. We chose the dimensionless variable for time t is $\tau = t/t_0$.

Using an Ubbelohde viscometer and by the Stokes falling-ball method, we determined the viscosity of the GGW mixture to be 350 ± 20 cP at about 24 °C. And from the work of Johnston and coworkers [Johnston et al., 1985], in GGW mixture at the one-phase region, the correlation length

$$\xi^+ = \xi_0 \; ^+ \; | \; T/T_c \; - 1 \; |^{-\nu} \qquad\qquad (5.6)$$

where the $\xi_0 \; ^+$ is about 0.32 nm and the critical exponent $\nu = 0.63$. Inside the miscibility gap (two-phase region), the correlation length $\xi_0 \; ^- = \xi_0 \; ^+/2$, which is a universal ratio, therefore, $\xi_0 \; ^- = 0.16$ nm. We replotted the data in Fig. 5.6 in terms of dimensionless variable K_{max} and τ, and the results for the fast mode is shown in Fig. 5.8. Unlike the earlier studies on binary fluids, where the peak position vs. time data from different quench depths collapsed onto a single universal curve [Chou and Goldburg, 1979; Goldburg, 1983], the fast mode data still show a systematic deviation from a single curve for data from different quench depths. This deviation is expected from the original data in Fig. 5.6, where the slopes was quench depth dependent. It is also an indication something novel, different from the conventional phase separation process in bulk.

Lately Wiltzius and coworkers [Wiltzius et al., 1993] were able to show that the fast mode results from polymer mixture [Cumming et al., 1992] fell on top of those from GGW mixture on plots of K_{max} vs. τ, although the polymer data could not be resolved the quench depth dependence of the kinetic exponent b, presumably due to the larger noise present in the data set. Thus the fast mode phenomena in two fluid mixtures are quantitatively the same. This strongly supports the notion that the fast mode phenomenon is generic to all the fluid mixtures, as it has been seen in two very different binary mixtures.
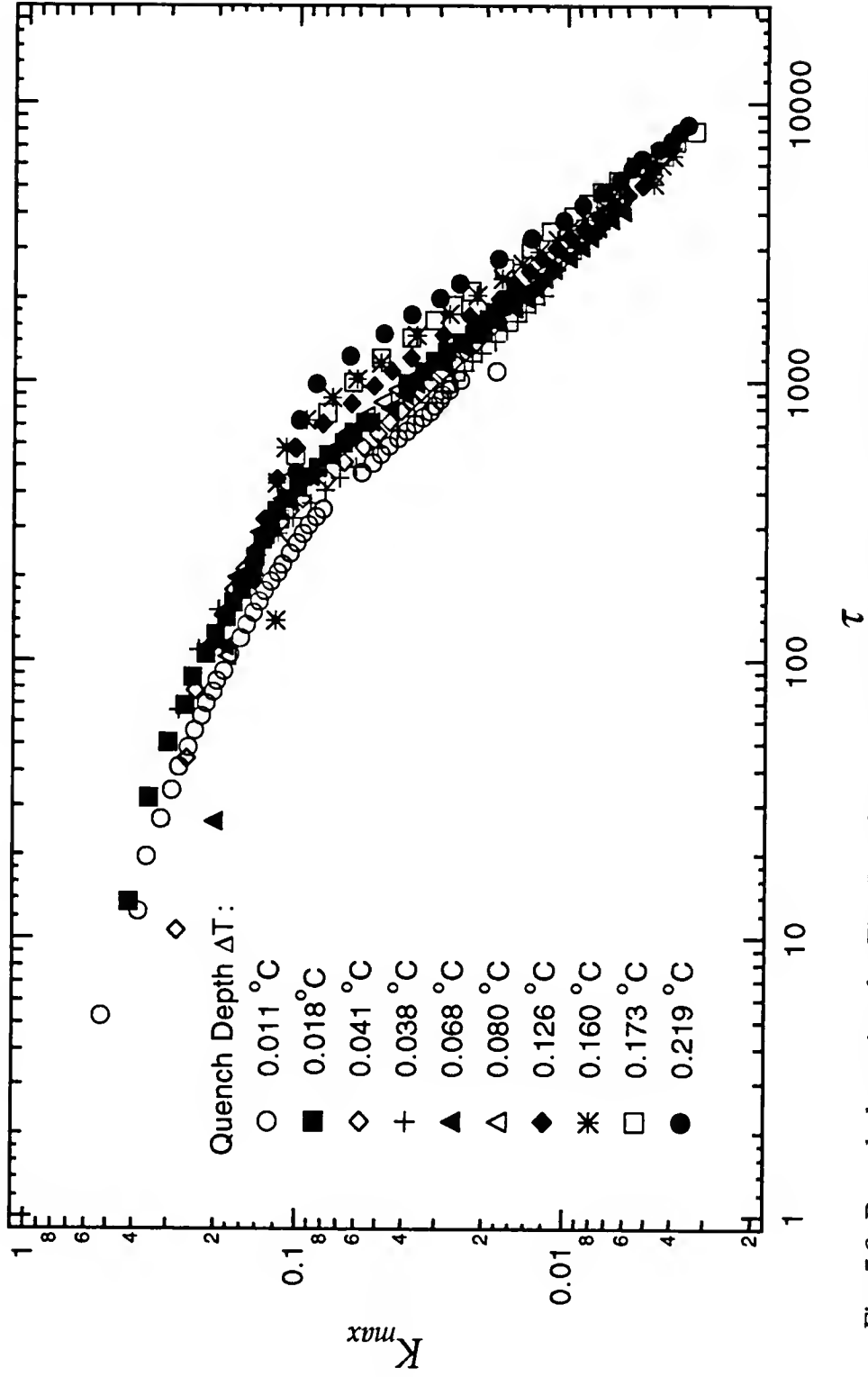
Fig. 5.8 Rescaled version for Fig. 5.6 of the fast modes. K_{max} is peak position Q_{max} multiplied by the correlation lenghth, and τ is time t rescale with the diffusion time t_0. There the dependence on the system parameters and quench depth were eliminated. But the data didn't quite collapse onto a single universal curve as expected from the bulk phase separation, a systematic deviation can be seen.
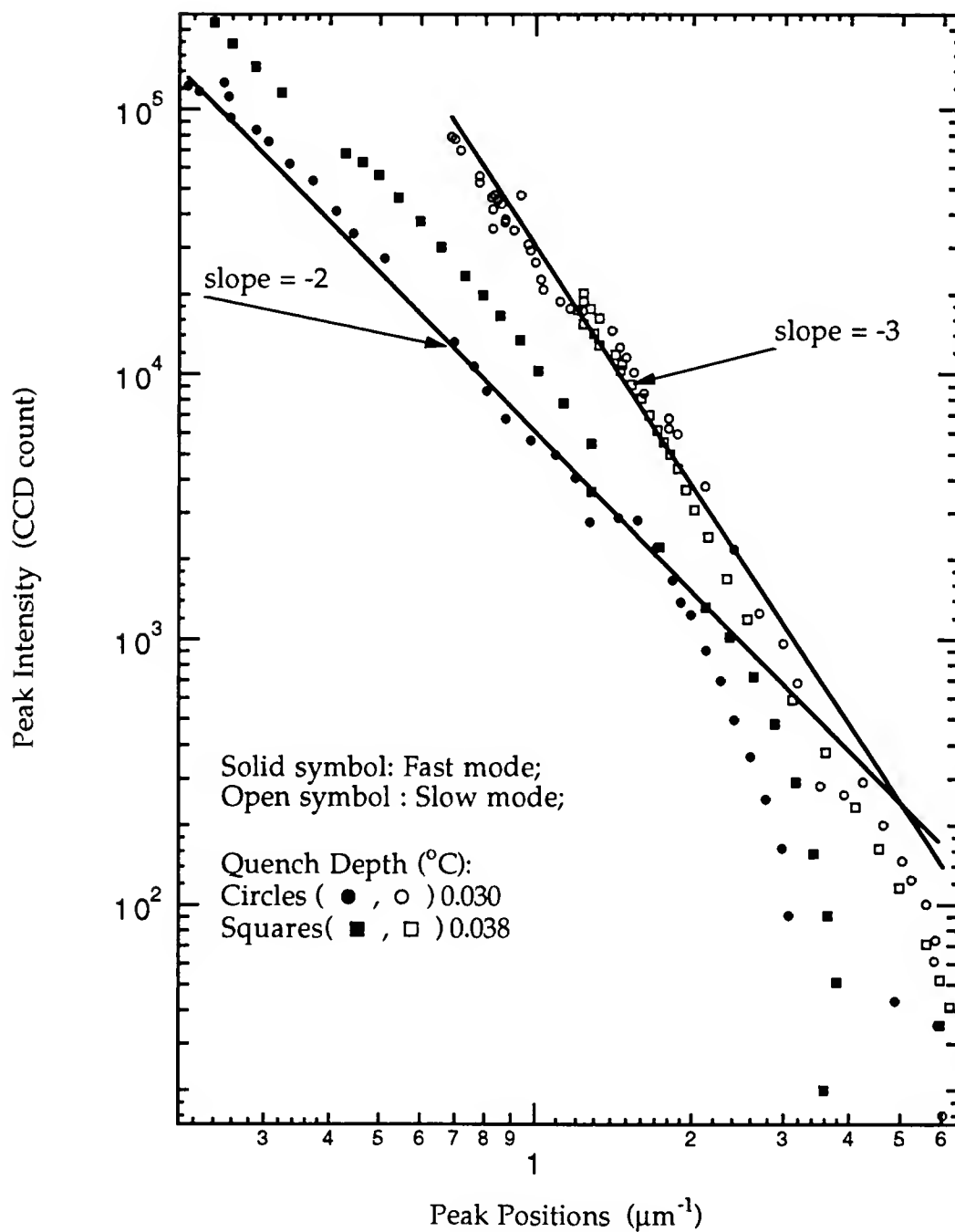
Fig. 5.9. Peak intensity vs. peak position in q-space for both fast and slow modes respectively on logarithmic axes. At late stage, the relation between the intensity and position follow a power law, satisfying the dynamical scaling hypothesis. The slope of the power law is -2 for the fast mode, and -3 for the slow mode, respectively.

There have been numerous experiments [e.g., Wong and Knobler, 1981; Chou and Goldburg, 1981; Gaulin et al., 1987; Izumitani et al., 1990] which confirmed the hypothesis of dynamic scaling (eq. (1.42), see §1.4D) in phase-separating fluids. At later stage, the morphology of the domains are approximately self-similar in time, and there is only one dominant length scale $q_m(t)$ in the system. If the hypothesis is right, then the peak intensity should follow a power-law with the peak position $q_m(t)$ according to eq. (1.43), with the power equal to - d, where d is the dimensionality of the underlying structure that is responsible for the scattering, and in the common phase separation process in bulk, d = 3. We sought to confirm the slow mode was associated with the coarsening of a three dimensional structure by plotting I_s vs. q_s on logarithmic axes, as shown in Fig. 5.9, and found that data indeed fell on a straight line with slope -3 at late stage, correspondingly d=3. We made the similar plots for the fast mode data and found they fell again on a straight line, but with slope -2 approximately, suggesting the underlying structure is two dimensional. Fig. 5.9 showed data sets from two relatively shallow quenches, for the peak intensities could be very sensitive to the multi-scattering and we wanted to limit its effect as much as possible, we drew two lines of slope -2 and -3 respectively across the fast mode and the slow mode data for comparison. At late stage of phase separation, the data follow the trend of their respective lines. The results from polymer mixture also showed the same behavior [Wiltzius and Cumming, 1991].

5.3 Gravitation Effects

Gravity plays an important part in binary fluids if the two components are not density matched, especially near the critical point T_c, at which it will

lead to the formation of a concentration gradient [Fannin and Knobler, 1974; Greer et al., 1975; Kwon et al., 1977], and the gradient takes excessively long time to diffuse away due to vanishing interdiffusion constant (eq. (5.5)). In probing the critical behavior, the gravity imposed increasing important problems that limited the accuracy of experiments [for a review, see Hohenberg and Barmatz, 1972; Moldover et al., 1979].

The densities of glycerol and guaiacol are 1.261 g/cm^3 and 1.129 respectively, in pure form as purchased, the GGW mixture thus has about 10% density mismatch between the pure phases glycerol-water and guaiacol, which is relatively large compared to those binary fluids used in the previous studies. In our experiments, we found the gravity had a particular strong effect on the fast mode, and this is what we will focus on in the following discussion.

In our original design of the elastic light scattering, (see Fig.3.1), our disk-shaped sample cell was oriented such that the disk plane was vertical. When the sample cell was in such an orientation, we observed that the fast mode would gradually diminish and eventually disappear within about 8 hours. This was the reason for the elusiveness of the fast mode in our initial experiments, that it simply disappeared after one or two quenches. After several months of bewilderment, we found that the fast mode could be restored consistently by taking the sample cell down from the anchoring posts and letting it lie flat (in horizontal plane) on the optical table while annealing after every quench. Fig. 5.10 shows the results of several quenches made after the fast mode had disappeared. Clearly the peak position followed the kinetics of the slow mode, and the structure functions following the quenches
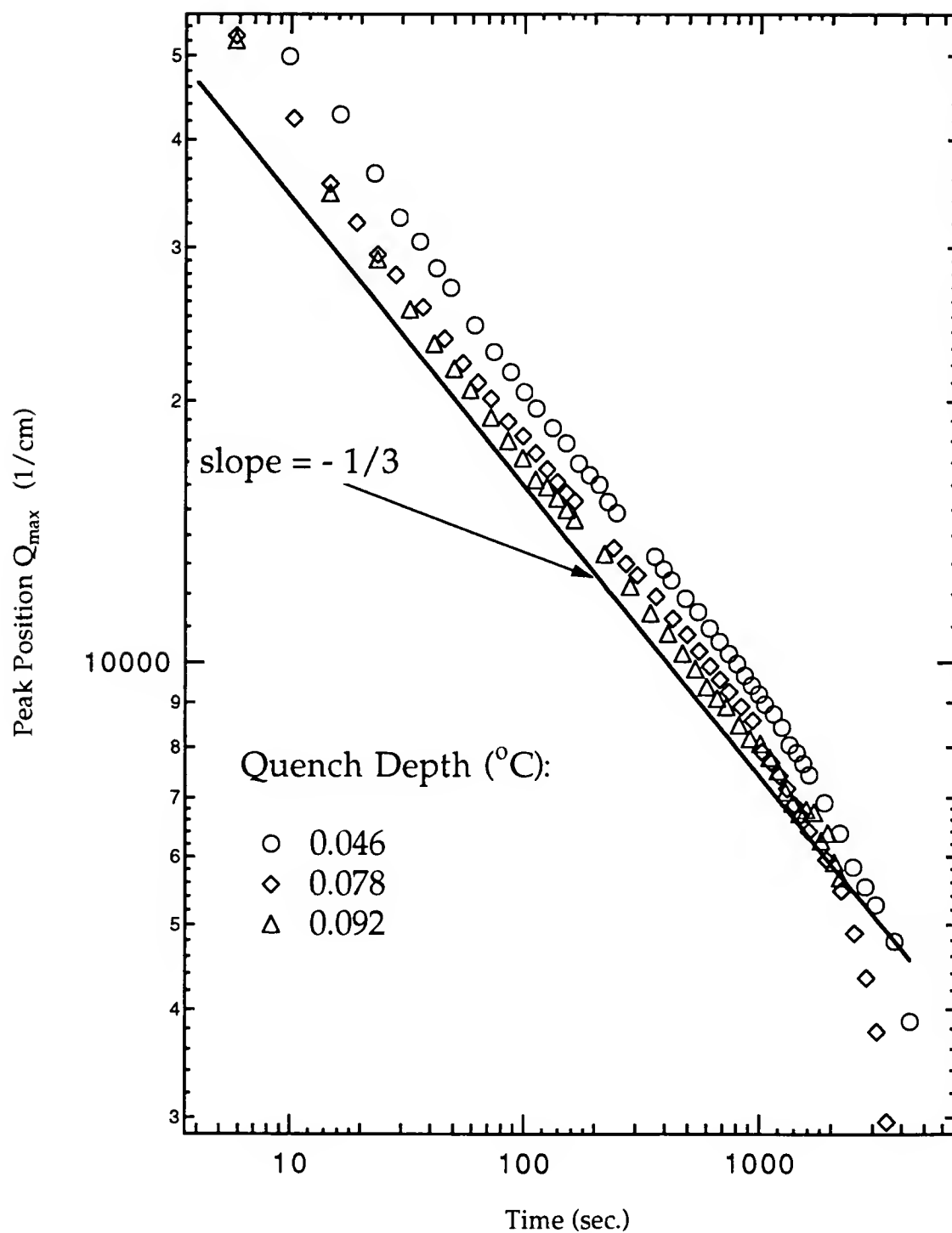
Fig. 5.10 Peak position in q-space vs. time when that only one peak appeared in the structure function following a quench. The sample was in vertical position for over 6 hours before the quenches were made.

could be well fitted with a Furukawa function of eq. (5.2). For this reason, we changed the configuration of our light scattering apparatus from its original design (Fig. 3.1) to the final design shown in Fig. 3.3, where the sample cell rested in horizontal rather than the vertical plane as in Fig. 3.1. As our sample cells were of less than 1 mm thick, the gravity effects were significantly reduced as a result of the reorientation of the sample cell. From then on, we were able to observe the fast mode in every quench.

The two polymer components used in the experiments of Cumming and coworkers [Cumming et al., 1992] were specially density matched (density mismatch < 0.1%), therefore the gravity effect discussed above was not observed. But the gravity is unlikely to play any other significant roles of the fast-mode phenomenon, as it was observed in the two systems with a rather larger difference (a factor of 100) in their degrees of density mismatch.

5.4 Surface Treatment and Its Effects

We gave a full description on our method of treating the glass and sapphire windows with trichlorosilanes. Essentially it was a two-step process: first the windows were cleaned with a strong acid ("pirahna" solution, see §4.5), and then treated with the silane solution to form an SA monolayer on the surfaces of the windows.

We have used four trichlorosilane compounds in the window treatment: PET, ETS, DTS, OTS. The last three belong to a homologous series, with different lengths in the tail part, from 2 carbon chain in ETS to a 18-carbon chain in OTS. As we knew, after the step of acid cleaning, the window surface had a higher affinity to the glycerol-rich phase over the guaiacol-rich

phase. However, after the SA monolayer treatment with the silanes, the affinity was reversed, as we have demonstrated with capillary rise experiments. The effect of the acid cleaning and silane treatment to the window surface was evident: After the step of acid cleaning, the surface became much more hydrophilic compared to that before the cleaning; and the silane treatment turned the surface hydrophobic.

We performed a series of quench experiments on sample cells with these windows that have been treated. The thickness of the sample cells were 0.8 mm. Fig. 5.11 showed the peak position vs. time plot of the fast mode on a sample with windows treated with OTS, where we also showed the power-law fit function for each quench. It clearly showed the increase of the slope with the quench depth. We have replotted the fast-mode data in terms of the dimensionless variables K_{max} and τ defined in eq.(5.3) and (5.4), and the result is shown in Fig. 5.12. Four sets of data are included, each from a sample cell with windows treated differently. Each set of data overlapped almost on top of one another, and within the uncertainty of the data, we could not detect any systematic difference. Fig. 5.12 showed the same features as the earlier Fig. 5.8.

The only subtle difference among the data could be seen in Fig. 5.13, where we plotted the kinetic exponent b vs. the quench depth. Despite the larger error bars of the data, we can observe consistently the higher exponent at the same quench depth in these samples that have been acid cleaned than those that didn't undergo this step, but within the uncertainty, the data didn't show any systematic difference among those with windows treated differently, either with different silanes or simply acid cleaned. These data indicate the difference is due to the acid cleaning, not to the silane monolayer.

It was well known the sulfuric acid solution we had used in cleaning windows was very reactive, it "eats" away all the organic matter left on the window surface (see §4.5). This cleaning step left the surface free of dirt, oil and other organic compounds, *i.e.*, a clean surface. It is possible that the acid did more than cleaning and fully hydroxylating the window surface, maybe a little etching, but this effect should be small. But it is understandable that effect of the acid cleaning is quite different from the treatment with silanes, which resulted in a monolayer on the surface. On the other hand, those windows that didn't undergo this step could still have certain dirt, oil or other contaminants left on the surface, even after our conventional cleaning process. Therefore, we can regard those data from the acid-cleaned cells are in a clean limit, while those not cleaned with acid are in a dirty limit. And the difference in the data in Fig. 5.13 is a result of the two limits.

The silane treatment effectively reversed the role of the two phases (glycerol-rich and guaiacol-rich) with respect to the surface of the windows. But the dynamics that underlies the fast mode is probably symmetric with respect to the two phases, just like the critical properties associated with the critical point. If this is what happened, we should not see any difference in our data from silane treatment.

In summary, within our experimental uncertainty, we couldn't see any consistent and repeatable difference in the data from samples whose windowswere treated with different silanes. The only change observed was due to the acid cleaning, which resulted an increase in the kinetic exponent, especially at quench depth larger than 0.05 °C.
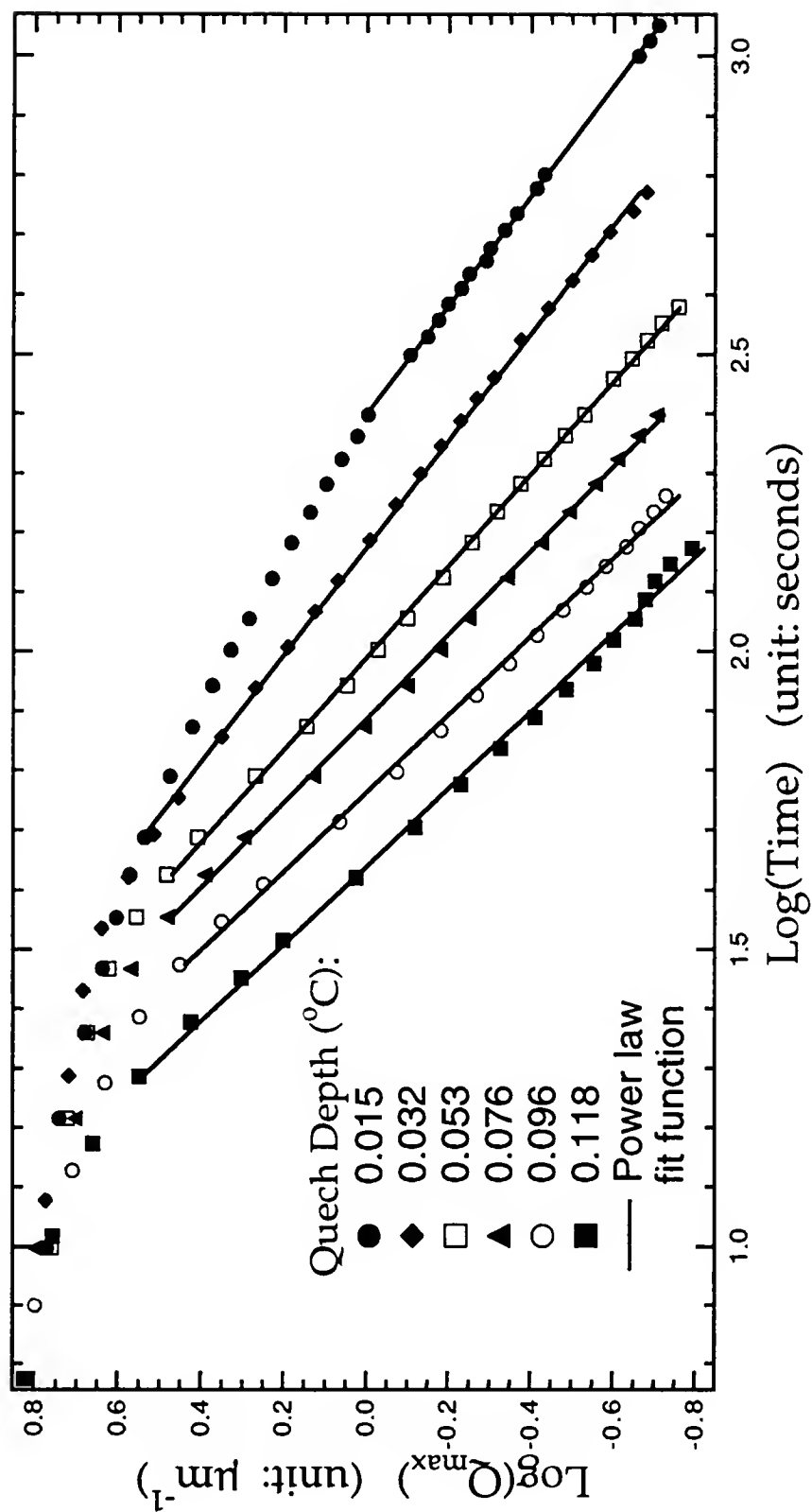
.

Fig. 5.11 A plot of log(peak position) vs. log(time) for a sample whose windows were treated with Octadecyltrichlorosilane (OTS). A power law was fitted to the data of each quench, as shown by the solid lines.
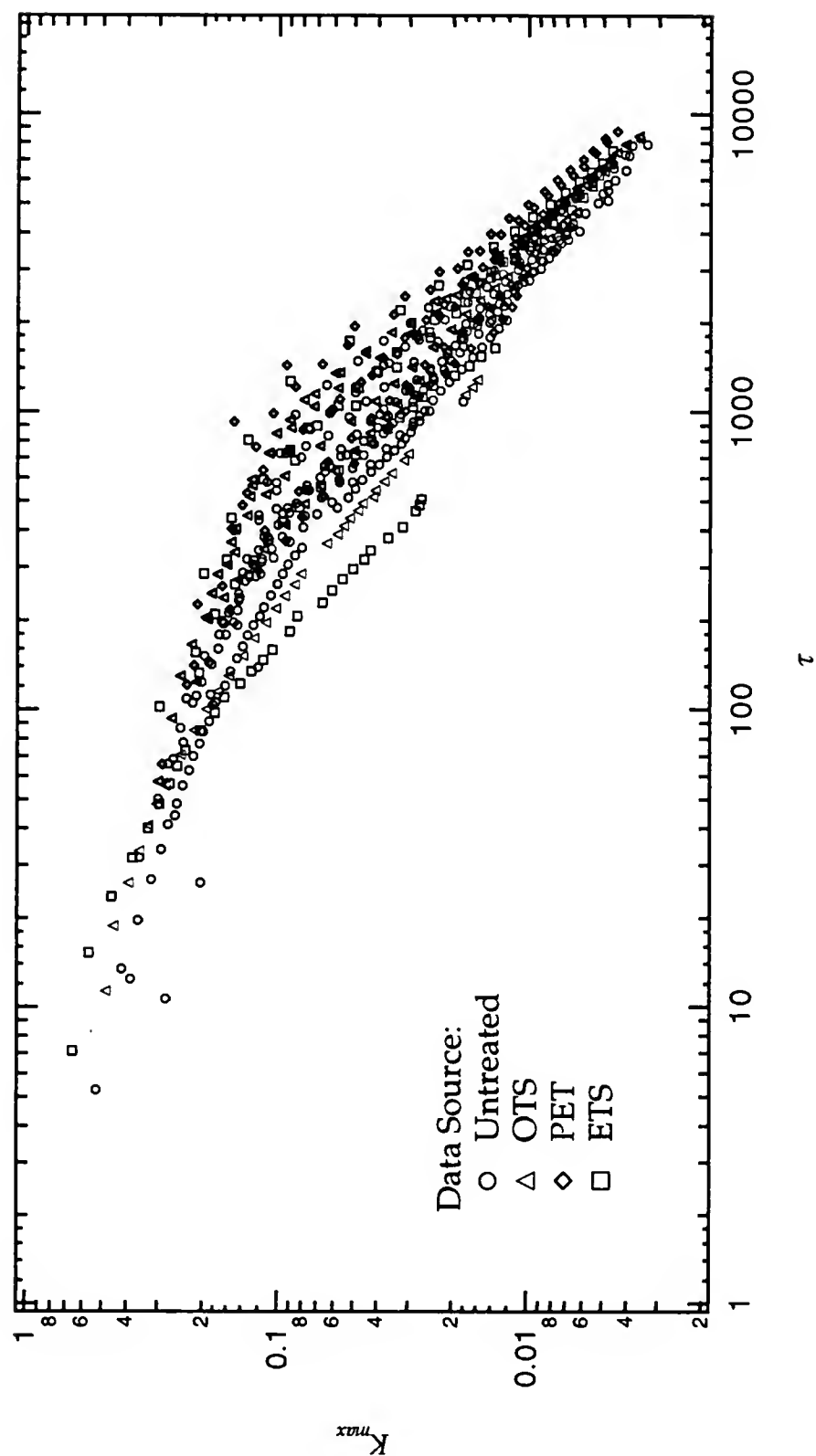
Fig. 5.12 The peak positions vs. time in dimensionless variables K_{max} and τ. The data from one sample are plotted with the same symbol. The untreated data is that same as those shown in Fig. 5.8. The OTS data is from Fig. 5.11, converted into dimensionless variable.
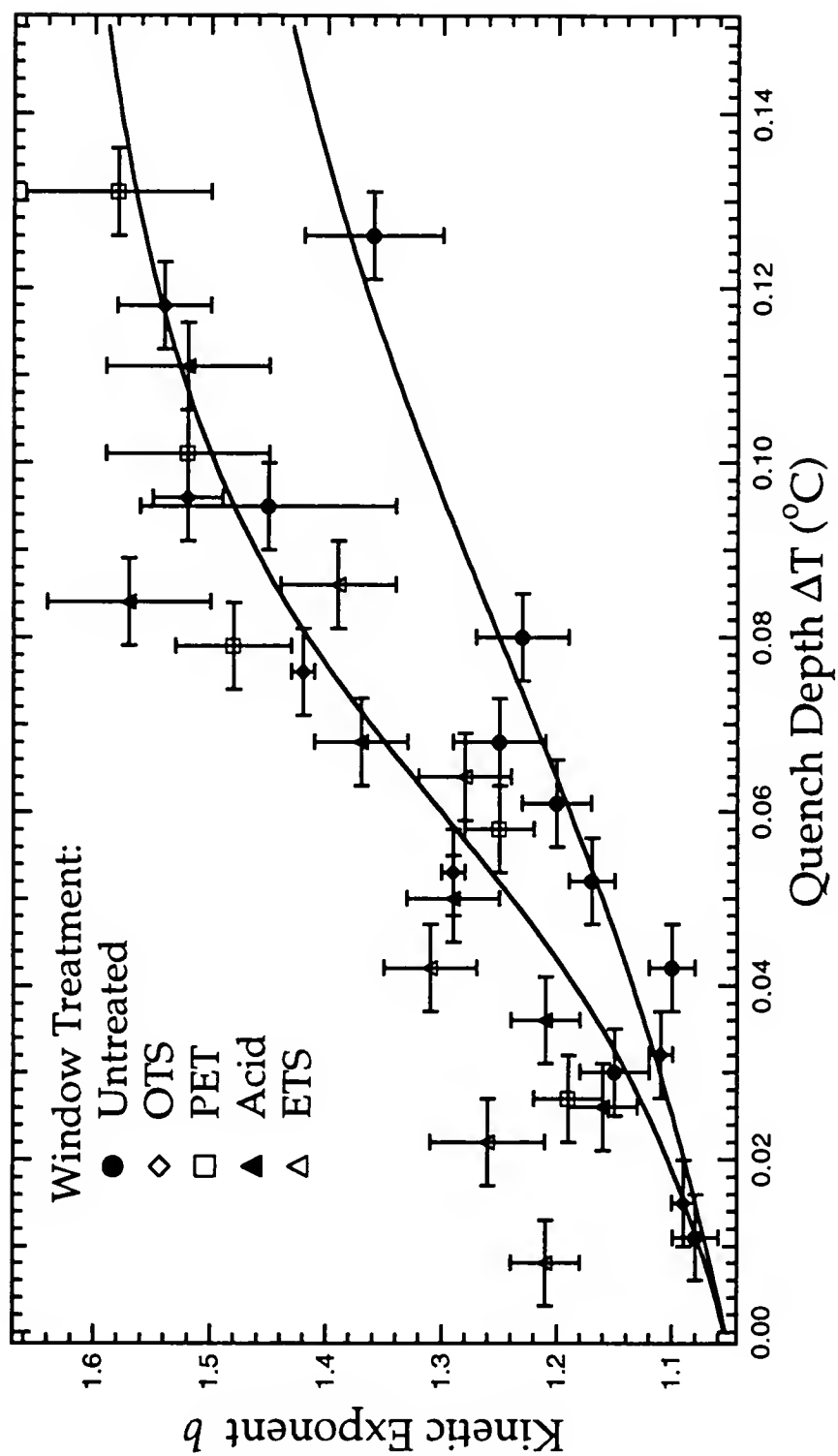
Fig. 5.13 Fast-modekinetic exponent vs. quench depth for sample cells whose windows were treated differently. The data in Fig. 5.7 are shown as the solid circles (untreated). The two solid lines are a guide to the eye across the data set.

5.5 Discussion

We do not have a theoretical description that would possibly account for the fast kinetics of the fast mode. By making the dynamical scaling hypothesis, we have observed the fast mode data are consistent with a 2-dimensional structure and a 3-dimensional structure for the slow mode. From the growth law of $L \sim t^{1/3}$, we were able to identify the slow mode as the conventional diffusion limited growth for coasening in the bulk, which is consistent with the 3-dimensional structure implied from the dynamical scaling. From the videomicroscopy studies [Harrison et al.,1993] of the domain morphology at late stages (after the spinodal rings have collapsed into the beam stop of the light scattering apparatus) in the same GGW mixture indicated that the fast mode was associated with the surfaces of our sample cell (windows). At this stage, when the length scales of the domain structures was much larger than what could be measured with light scattering, the domains corresponding to the fast mode appeard to be spreading or shrinking in the planar direction in a layer next to the surfaces of the windows. In the video microscopic study, we were unable to tell if a domain was of glycerol-rich or guaiacol-rich. But the motions of the domains appeared to resemble the spreading certain domains on a planar surface and squeezing the others aside. The video microscopic observation appeared to be consistent with the 2-dimensional structure from the dynamical scaling.

All these indicate that the fast mode is related to the surfaces. In addition, the change in the kinetic exponent further supported this point of view, that the fast mode is surface-mediated.

Within the range of quench depth of our experiments, we would expect the final state of the mixture to be well within the complete wetting region. Therefore the phase separation will result in a complete wetting layer of the preferred phase next to the container wall in equilibrium. The optical microscopic observations [Guenoun et al., 1990; Tanaka, 1993a; 1993b] on the subject of wetting layer indicated that the layer formed relative quickly, well in advance of the completion of the full phase-separation in bulk, one of the authors [Tanaka, 1993a] suggested that the fast mode was associated the formation of the wetting layer, and the fast growth was due to the interplay of the hydrodynamic flow similar to the Siggia mechanism (see §1.4C) and the wetting effect. This is certainly an appealing proposal. In our video microscopic studies, due to the cell setup, we were not able to observe the wetting layer directly, and the layer where the fast mode was observed could well over 10 μm in thickness, which makes it unlikely to be the wetting layer itself. But the layer itself could well be associated with the wetting layer formation. The association of the fast mode with the wetting layer could also provide a possible explanation of the effect of gravity on the fast mode. Due to the presence of the large density mismatch in GGW mixture, the concentration gradient can develop along the vertical direction. If the cell was oriented vertically, just as in our initial experiments, the concentration gradient was along the surface of the windows. This concentration gradient could prohibit the formation of a wetting layer due to the Marangoni effect [see, *e.g.*, Adamson, 1990]. However, when the cell lies horizontally, there is no gradient across the surfaces of the windows.

However, the gravity is not responsible for the occurrence of the fast mode. In the work of Cumming and coworkers [Cumming et al., 1992] on the polymer mixtures, they were able to eliminate the gravity as a potential cause

of the fast mode, and two polymers involved in the studies were specially density-matched. The gravity effect on the fast mode observed in GGW mixture was a peculiar effect of the system.

.

CHAPTER 6

CONCLUSIONS

With the observation of the fast mode both in a simple low-molecular-weight mixture like GGW and a polymer mixture, it establishes that the fast-mode phenomenon as generic to a broad category of fluid mixtures. The fast mode followed the kinetics of a power law, where the average domain size L grows at t^b (t is the time), and the kinetic exponent b ranges from 1.1 for a quench of depth 0.01 °C to about 1.5 for depth above 0.08 °C. The mode of growth is probably associated with the formation of a wetting layer next to the container wall.

To further understand the fast-mode phenomenon we will need a theoretical description. The results of our experiments indicate it is possibly a dynamic wetting phenomenon, which at this stage, we are just beginning to grasp certain aspects of it.

Our experiments on the fast mode were slightly limited in scope. We have restricted our experiments only on the mixtures with critical concentration, where the mixture phase separates via spinodal decomposition. It will be quite interesting to study the phenomena in the off-critical mixtures, where there is the asymmetry of a major phase and a minor phase, especially in the light of the recent theoretical work [Troian, 1993]. However, there are obvious limitations on the information one can obtain with the light scattering methods, and it will be helpful to observe the fast mode using the

112

other methods, like ellipsometry, which can directly yield information on the growth of the wetting layer and thus establish the possible link between the fast mode and the formation of the layer. Each method of observation can yield only a limited aspect of an unknown phenomenon. Thus it is essential to use several complementary techniques in order to gain a full understanding of the phenomenon.

APPENDIX
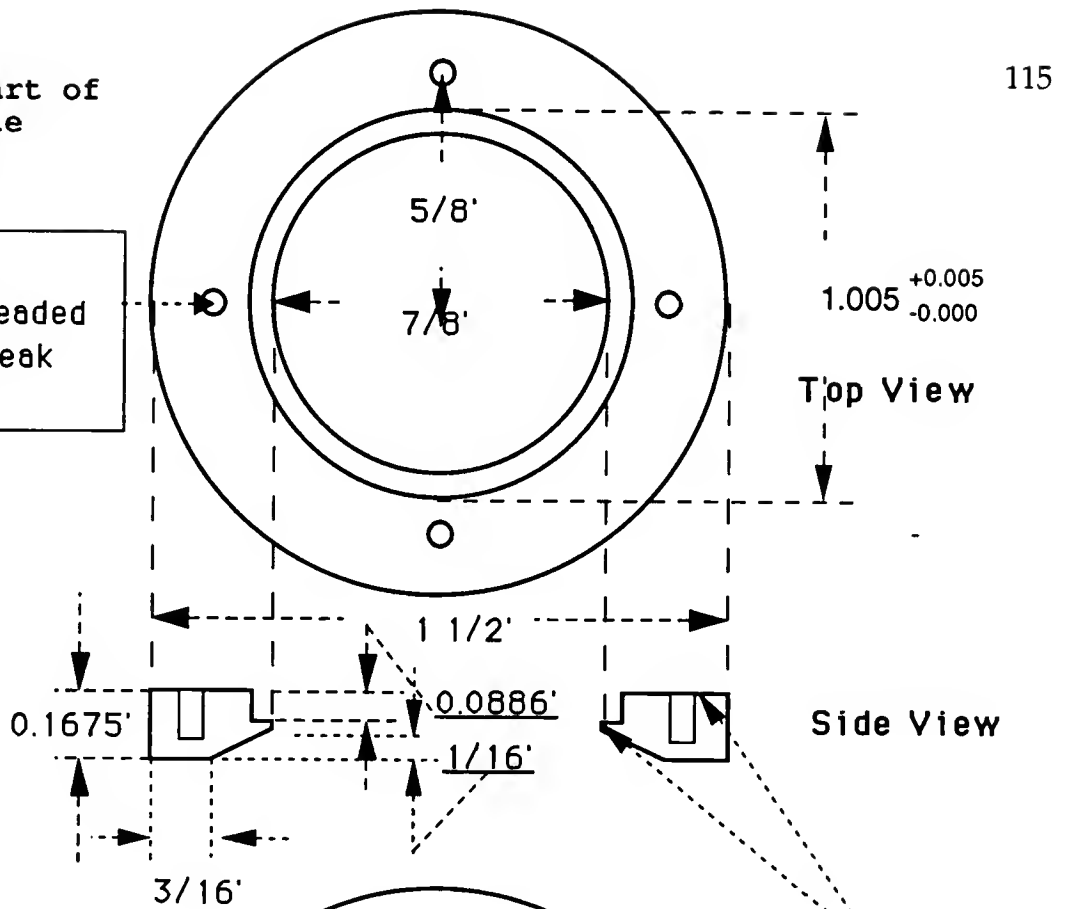
SAMPLE CELL CARRIER DESIGN
(Mechanical Drawing)

Note:

The sample cell carrier consists of two parts that clamped together with 4 screws (3-48 size). It clamped together the two optical windows with a Teflon gasket in between (see Fig. 4.3). It was made of stainless steel. The unit in the drawing is inch.
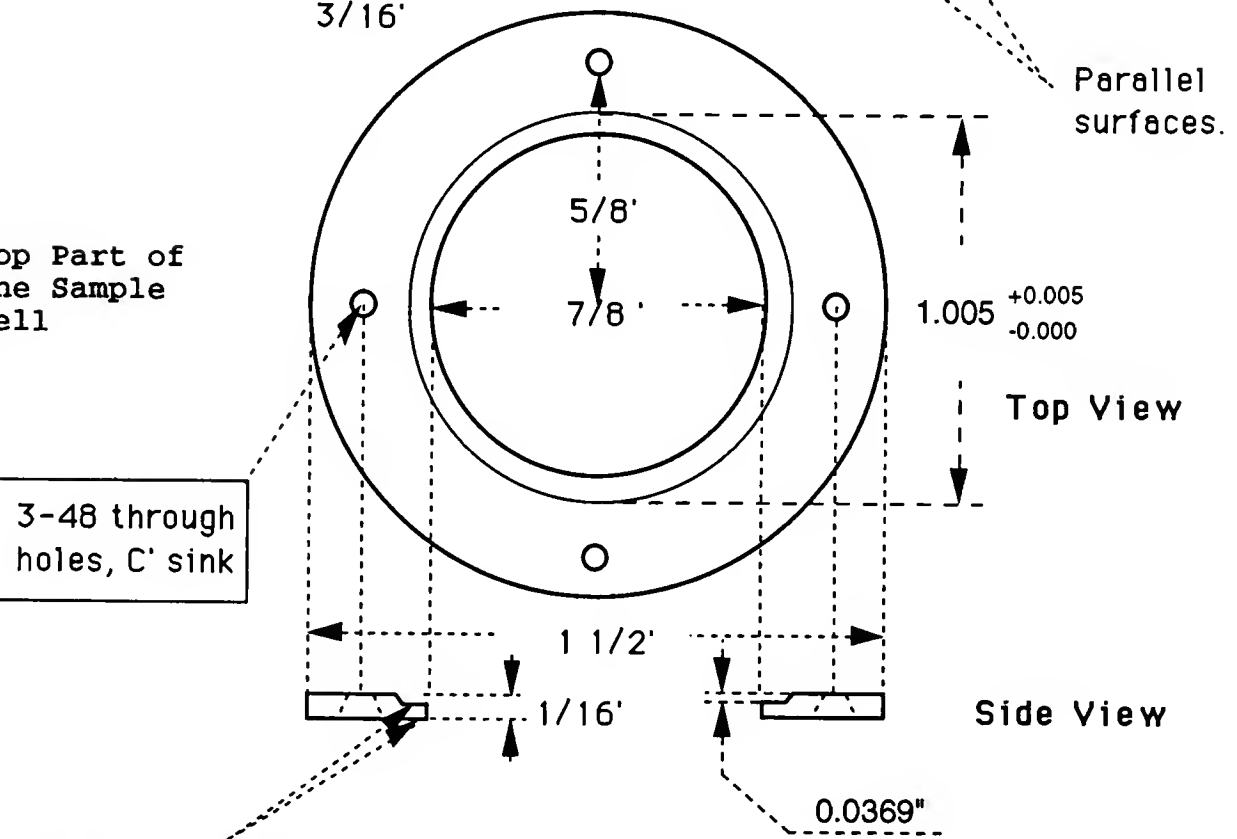
**Bottom Part of
the Sample
Cell**

4 holes:
3-48 threaded
Do not break
through.

5/8'

7/8'

1.005 $^{+0.005}_{-0.000}$

Top View

1 1/2'

0.1675'

0.0886'

1/16'

3/16'

Side View

Parallel
surfaces.

**Top Part of
the Sample
Cell**

5/8'

7/8 '

1.005 $^{+0.005}_{-0.000}$

Top View

3-48 through
holes, C' sink

1 1/2'

1/16'

0.0369"

Side View

Parallel surfaces.

Unit: Inch.

Material: Stainless

REFERENCES

Abeysuriya, K., Wu, X.-l., and Franck, C. (1987). *Phys. Rev.* B, 35, 6771.

Adamson, A. W., (1990). *Physical Chemistry of Surfaces*, 5th edition, (John Wiley and Sons, New York).

Bates, F. and Wiltzius, P. (1989). *J. Chem. Phys.* 91, 3258.

Berne, B. J. and Pecora, R. (1976). *Dynamic Light Scattering*, (Wiley-Interscience, New York)

Beysens, D., Guenoun, P. and Perrot, F. (1988). *Phys. Rev. A* 38, 4173.

Binder, K., Billotet, C. and Mirold, P. (1978). *Z. Phys. B* 30, 183.

Binder, K. and Stauffer, D. (1974). *Phys. Rev. Lett.* 33, 1006.

Binder, K. and Stauffer, D. (1976). *Adv. Phys.* 25, 343.

Brochard-Wyart, F. and Daillant, J. (1990) *Can. J. Phys.* 68, 1084.

Cahn, J. W. (1961). *Acta Metall.* 9, 795.

Cahn, J. W. (1962). *Acta Metall.* 10, 179.

Cahn, J. W. (1966). *Acta Metall.* 14, 1685.

Cahn, J. W. (1968). *Trans. Metall. Soc. AIME* 242, 166.

Cahn, J. W. (1977). *J. Chem. Phys.* 66, 3667.

Cahn, J. W. and Hilliard, J. E. (1958). *J. Chem. Phys.* 28, 258.

Cahn, J. W. and Hilliard, J. E. (1959). *J. Chem. Phys.* 31, 688.

Chen, J.-D. and Wada, N. (19890. *Phys. Rev. Lett.*, 62, 3050.

Chou, Y. C. and Goldburg, W. I. (1979) *Phys.Rev. A* 20, 2105.

Chou, Y. C. and Goldburg, W. I. (1981) *Phys.Rev. A* 23, 858.

Chu, B. (1974). *Laser Light Scattering*, (Academic Press, New York).

Chu, B. (1991). *Laser Light Scattering*, 2nd edition, (Academic Press, New York).

Cook, H. E. (1970). *Acta Metall.* 18, 297.

Cumming, A., Wiltzius, P., Bates, F. and Rosedale, J. (1992) *Phys. Rev A* 45, 885.

de Gennes, P. G. (1985) *Rev. Mod. Phys.* 57, 827.

Dixon, J. A., Schlossman, M., Wu, X.-l. and Franck, C. (1985). *Phys. Rev. B,* 31, 1509.

Durian, D. J. and Franck, C. (1987). *Phys. Rev. Lett.* 59, 555.

Fannin, A. A. and Knobler, C. M. (1974). *Chem. Phys. Lett.* 25, 92.

Furukawa, H. (1977). *Phys. Lett.* 62A, 377.

Furukawa, H. (1978). *Prog. Theoret. Phys.* 59, 1072.

Furukawa, H. (1979). *Phys. Rev. Lett.* 43, 136.

Furukawa, H. (1981). *Phys. Rev. A* 23, 1535.

Furukawa, H. (1985). *Adv. Phys.* 34, 703.

Gaulin, B. D., Spooner, S., and Morii, Y. (1987). *Phys. Rev. Lett.* 59, 668.

Goldburg, W. I. (1983). in *Light Scattering Near the Phase Transition,* edited by H.Z. Cummins and A. P. Levanyuk (North Holland, Amsterdam).

Greer, S. C., Block, T. E. and Knobler, C. M. (1975). *Phys. Rev. Lett.,* 34, 250.

Guenoun, P., Beysens, D. and Robert, M. (1990). *Phys. Rev. Lett.* 65, 2406.

Guenoun, P., Gastaud, R., Perrot, F. and Beysens, D. (1987). *Phys. Rev A* 36, 4876.

Gunton, J. D., San Miguel, M. and Sahni, P.S. (1983). in *Phase Transition and Critical Phenomena,* vol. 8, edited by C. Domb, and J. L. Lebowitz (Academic Press, New York).

Harrison, C., Rippard, W., and Cumming, A. (1993) to be published.

Hashimoto, T. (1988). *Phase Transitions,* 12, 47.

Hashimoto, T., Itakura, M. and Hasegawa, H. (1986). *J. Chem. Phys.* 85, 6118.

Hashimoto, T., Itakura, M. and Shimidzu, N. (1986). *J. Chem. Phys.* 85, 6773.

Hecht, E. (1987). *Optics,* 2nd edition, (Addison-Wesley, Menlo Park, CA).

Heslot, F., Cazabat, A. M. and Levinson, P. (1989) *Phys. Rev. Lett.,* 62, 1286.

Hohenberg, P. C. and Barmatz, M. (1972) *Phys. Rev. A,* 6, 289.

Hohenberg, P. C. and Halperin, B. I. (1977) *Rev. Mod. Phys.* 49, 435.

Hono, K. and Hirano, K. I. (1987) *Phase Transitions,* 10, 223.

Huse, D. A. (1986). *Phys. Rev. B* 34, 7845.

Izumitani, T., Takenaka, M. and Hashimoto, T. (1990). *J. Chem. Phys.* 92, 3213.

Johnston, R. G. (1983). Ph. D. Dissertation, Univ. of Colorado. (UMI Dissertation Services, Ann Arbor, Michigan)

Johnston, R. G., Clark, N. A., Wiltzius, P. and Cannell, D. S. (1985) *Phys. Rev. Lett.* 54, 49.

Kaski, K., Binder, K. and Gunton, J. D. (1983) *J. Phys.* A16, L623.

Kawasaki, K. and Ohta, T. (1978). *Prog. Theor. Phys.* 59, 362.

Kerker, M. (1969). *The Scattering of Light and Other Electromagnetic Radiation,* (Academic Press, New York).

Knobler, C. M. and Wong, N. C. (1981). *J. Phys. Chem.* 85, 1972.

Kwon, O., Kim, D. M. and Kobayashi, R. (1977). *J. Chem. Phys.,* 66, 4925.

Langer, J. S. (1974). *Physica* 73, 61.

Langer, J. S., Bar-on, M. and Miller, H. D. (1975). *Phys. Rev. A* 11, 1417.

Lebowitz, J. L., Marro, J. and Kalos, M. H. (1982). *Acta Metall.* 30, 297.

Levich, V. G. (1962), *Physiochemical Hydrodynamics,* (Prentice-Hall, Englewood Cliffs, N.J.)

Lifshitz, E. M. and Pitaevskii, L. P. (1981). *Physical Kinetics, Course on Theoretical Physics,* vol. 10, (Pergamon Press, Oxford).

Lifshitz, I. M. and Slyozov, V. V. (1961). *J. Phys. Chem. Solids* 19, 35.

Lipowsky, R. and Huse, D. A. (1986). *Phys. Rev. Lett.* 57, 353.

Moldover, M. R., Sengers, J. V., Gammon, R. W. and Hocken, R. J. (1979) *Rev. Mod. Phys.* 51, 79.

Porod, G. (1951). *Kolloid-Z.* 124, 83.

Porod, G. (1982). in *Small-Angle X-Ray Scattering,* edited by O. Glatter and O. Kratsky, (Academic, New York).

Redon, C., Brochard-Wyart, F. and Rondelez, F. (1991). *Phys. Rev. Lett.*, 66, 715.

Sasaki, K. and Hashimoto, T. (1984) *Macromolecules*, 17, 2818.

Shi, B. Q., Harrison, C. and Cumming. A. (1993). *Phys. Rev. Lett.* 70, 206.

Siggia, E. D. (1979). *Phys. Rev. A* 20, 595.

Stanley, H. E. (1971). *Introduction to Phase Transitions and Critical Phenomena*, (Oxford University Press, Oxford).

Takenaka, M., Izumitani, T. and Hashimoto, T. (1990). *J. Chem. Phys.* 92, 4566.

Tanaka, H. (1993a). *Phys. Rev. Lett.*, 70, 53.

Tanaka, H. (1993b). *Phys. Rev. Lett.*, 70, 2770.

Tomozawa, M., MacCrone, R. K., and Herman, H. (1970) *Phys. Chem. Glasses*, 11, 136.

Troian, S. M. (1993). *Phys. Rev. Lett.*, 71, 1399.

Ulman, A. (1991). *An Introduction to Ultrathin Organic Films: From Langmuir-Blodgett to Self Assembly*, (Academic, San Diego).

van de Hulst, H. C. (1957). *Light Scattering by Small Particles*, (John Wiley & Sons, New York)

Voorhees, P. W. and Glicksman, M. E. (1984). *Metall. Trans.* 15A, 1081.

Walker, J. S. and Vause, C. A. (1980). *Phys. Lett.* 79A, 421.

Walker, J. S. and Vause, C. A. (1983). *J. Chem. Phys.* 79, 2660.

Wiltzius, P. and Cumming, A. (1991). *Phys. Rev. Lett.* 66, 3000.

Wiltzius, P., Cumming, A., and Shi, B. Q. (1993). to be published.

Wong, N. C. and Knobler, C. M. (1978). *J. Chem. Phys.* 69, 725.

Wong, N. C. and Knobler, C. M. (1979). *Phys. Rev. Lett.* 43, 1733; 45, 498.

Wong, N. C. and Knobler, C. M. (1981). *Phys. Rev. A* 24, 3205.

BIOGRAPHICAL SKETCH

Qingbiao Shi, commonly known as Bill Q. Shi, was born on April, 28, 1963 in Hangzhou, China. He attended Fudan University in Shanghai, China, and received his B. S. degree in physics in July, 1984. He came to the University of Florida in August, 1986 for graduate study in physics.

In his spare time, he enjoys traveling, hiking and biking, especially into the wilderness. He dreams one day he will be a mountain climber, and go back to native country, China, which enjoys some of the highest mountain ranges in the world, to explore some of these regions.
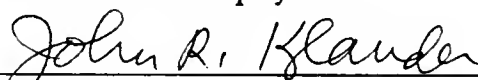
I certify that I have read this study and that in my opinion it conforms to acceptable standards of scholarly presentation and is fully adequate, in scope and quality, as a dissertation for the degree of Doctor of Philosophy.

Andrew W. Cumming, Chairman
Assistant Professor of Physics

I certify that I have read this study and that in my opinion it conforms to acceptable standards of scholarly presentation and is fully adequate, in scope and quality, as a dissertation for the degree of Doctor of Philosophy.
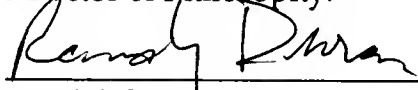
Neil S. Sullivan
Professor of Physics

I certify that I have read this study and that in my opinion it conforms to acceptable standards of scholarly presentation and is fully adequate, in scope and quality, as a dissertation for the degree of Doctor of Philosophy.

John R. Klauder
Professor of Physics

I certify that I have read this study and that in my opinion it conforms to acceptable standards of scholarly presentation and is fully adequate, in scope and quality, as a dissertation for the degree of Doctor of Philosophy.

James W. Dufty
Professor of Physics

I certify that I have read this study and that in my opinion it conforms to acceptable standards of scholarly presentation and is fully adequate, in scope and quality, as a dissertation for the degree of Doctor of Philosophy.

Randolph S. Duran
Assistant Professor of Chemistry

This dissertation was submitted to the Graduate Faculty of the Department of Physics in the College of Liberal Arts and Sciences and to the Graduate School and was accepted as partial fulfillment of the requirements for the degree of Doctor of Philosophy.

April, 1994

_____

Dean, Graduate School